

# **Investigation of Seepage near the Interface between an Embankment Dam and Concrete Structure: Monitoring and Modelling of Seasonal Temperature Trends**

by

**Tana Yun**

BSc Earth Sciences, University of Waterloo, Canada, 2015

A Thesis Submitted in Partial Fulfillment of  
the Requirements for the Degree of

**Master of Science in Earth Sciences**

in the Graduate Academic Unit of Earth Sciences

Supervisors: Karl E. Butler, Ph.D., Dept. of Earth Sciences  
Kerry T.B. MacQuarrie, Ph.D., Dept. of Civil Engineering and  
Canadian Rivers Institute

Examining Board: Jennifer J. Day, Ph.D., Dept. of Earth Sciences  
Won Taek Oh, Ph.D., Dept. of Civil Engineering

This thesis is accepted by the Dean of Graduate Studies

THE UNIVERSITY OF NEW BRUNSWICK

August, 2018

©Tana Yun, 2018

## **ABSTRACT**

The temperature monitoring method, which makes use of the fact that increased seepage flow may locally alter the natural temperature distributions within embankment dams and their foundations, is regarded as a useful approach for seepage monitoring and evaluation. In this study, spatial and temporal variations of temperature have been monitored and modelled at the interface between the compacted clay till core of an embankment dam and an adjoining concrete diversion sluiceway structure at the Mactaquac Generating Station, located on the Saint John River near Fredericton, NB. The measurements were acquired using a fibre optic distributed temperature sensing (DTS) system installed in a 50 m long borehole drilled into the concrete structure within 0.5 m of the interface. Two significant temperature anomalies were observed.

A three-dimensional finite element model was developed to simulate the temperature distributions within the dam resulting from the seasonal variations of air and headpond water temperatures. Anomalous seepage zones near the interface were simulated in the concrete and along the dam/concrete interface (in the embankment) independently, and in both locations simultaneously. The results demonstrate that passive DTS monitoring is a feasible approach to identify potential seepage zones near an embankment dam/concrete structure interface. Anomalous temperature zones, and associated gradients, can be clearly identified and numerical modelling can indicate, in some cases, whether such anomalies are related to seepage in the concrete or in the embankment; however, other details such as the water flow path geometries and seepage rates are not as well constrained.

## ACKNOWLEDGEMENTS

This thesis project could not have been accomplished without the help and care I received from many people.

First, I would like to express my sincere gratitude to my supervisors Dr. Karl Butler and Dr. Kerry MacQuarrie for their patience, enthusiasm and immense knowledge. Their excellent guidance and continuous support helped me a lot through my research and writing of this thesis.

Besides my advisors, I would like to thank the rest of my thesis committee: Dr. Jennifer Day and Dr. Won Taek Oh for their insightful comments and valuable advice. Special thanks to my colleagues Andrew Ringeri and Keenan Lamb from the Department of Earth Sciences and the Department of Civil Engineering, respectively, for their helpful guidance and support on database generation and numerical modelling.

I am grateful to Bruce Mclean, John Fletcher and Ian Campbell from NB Power for their generous support during the field activities and good suggestions on my research and to all of those who provided me with all kinds of support during my research.

I also acknowledge financial support received through an NSERC Collaborative Research and Development Grant with NB Power and a STEM scholarship received from the New Brunswick Innovation Fund, along with in-kind support from NB Power and DHI/FEFLOW.

Last but not the least, I would like to thank my parents and all my close friends for their love and inspiration.

## TABLE OF CONTENTS

<b>ABSTRACT</b> .....	ii
<b>ACKNOWLEDGEMENTS</b> .....	iii
<b>TABLE OF CONTENTS</b> .....	iv
<b>LIST OF TABLES</b> .....	vii
<b>LIST OF FIGURES</b> .....	viii
<b>LIST OF SYMBOLS AND ABBREVIATIONS</b> .....	xiv
<b>Chapter 1 : Introduction</b> .....	1
<b>1.1 Background</b> .....	1
<b>1.2 Dams and internal erosion processes</b> .....	2
<b>1.3 Temperature monitoring for seepage detection</b> .....	6
<b>1.4 Distributed Temperature Sensing (DTS) technology</b> .....	9
<i>1.4.1 Temperature data collection by DTS systems</i> .....	10
<i>1.4.2 Methods used to analyze DTS temperature data</i> .....	12
<b>1.5 Research objectives and significances</b> .....	14
<b>1.6 Thesis structure</b> .....	15
<b>Chapter 2 : Field data collection, processing and analysis</b> .....	16
<b>2.1 Instrumentation and data acquisition</b> .....	16
<b>2.2 DTS data plots and conceptual model</b> .....	22
<i>2.2.1 Observed temperature anomalies</i> .....	22
<i>2.2.2 Visual evidence of possible seepage</i> .....	27
<i>2.2.3 A conceptual model for possible seepage</i> .....	29
<i>2.2.4 A conjecture about the origin of seepage</i> .....	30
<b>2.3 DTS data processing and calibration</b> .....	33
<i>2.3.1 Adjustment of DTS calibration parameters</i> .....	37
<b>Chapter 3 : Theoretical background</b> .....	42
<b>3.1 Seepage and temperature fields in embankment dams</b> .....	42
<b>3.2 Hydro-thermal coupling</b> .....	43
<b>3.3 Numerical model selection</b> .....	49
<b>Chapter 4 : Numerical simulations of seasonal temperature variations for the case of bulk seepage only</b> .....	53
<b>4.1 Introduction</b> .....	53

<b>4.2 Simulation of heat transport near the dam/concrete interface – bulk seepage only</b> .....	54
4.2.1 <i>Finite element grid</i> .....	54
4.2.2 <i>Initial and boundary conditions</i> .....	59
4.2.3 <i>Material properties</i> .....	64
4.2.4 <i>Numerical settings for the simulation of bulk seepage</i> .....	69
<b>4.3 Parameter sensitivity analysis</b> .....	69
<b>4.4 Results and discussion</b> .....	72
<b>Chapter 5 : Numerical simulations for anomalous seepage analysis</b> .....	83
<b>5.1 Introduction</b> .....	83
<b>5.2 Simplified model for temperature gradients investigation</b> .....	84
5.2.1 <i>Simulation descriptions</i> .....	85
5.2.2 <i>Results and discussions</i> .....	86
<b>5.3 Simulation of the shallow temperature anomaly</b> .....	89
5.3.1 <i>Case 1: Anomalous seepage zone in the concrete only</i> .....	91
5.3.2 <i>Case 2: Anomalous seepage zone along the dam/concrete interface</i> .....	98
5.3.3 <i>Case 3: Anomalous seepage zone in concrete and along interface</i> .....	104
<b>5.4 Simulation of the temperature anomaly at elevation 95'</b> .....	106
<b>5.5 Discussion</b> .....	114
5.5.1 <i>Influence of grouting on seepage</i> .....	114
5.5.2 <i>Influence of freeze and thaw cycle</i> .....	116
5.5.3 <i>Recommendations for improvement of anomalous seepage simulations</i> .....	117
<b>Chapter 6 : Conclusions</b> .....	123
<b>REFERENCES</b> .....	128
<b>Appendix A. Instrumentation specification sheets</b> .....	140
<b>Appendix B. Headpond temperature vs. depth profile from Mactaquac Aquatic Ecosystem (MAES) project</b> .....	146
<b>Appendix C. Jib boom temperature data</b> .....	148
<b>Appendix D. Frost depth estimation at the Mactaquac dam</b> .....	150
<b>Appendix E. Construction of the Mactaquac embankment dam</b> .....	152
<b>Appendix F. Simulated temperatures within the dam/concrete structure</b> .....	154
<b>Appendix G. Interpreted position of the clay till core-concrete interface through a borehole seismic reflection survey</b> .....	158

**Appendix H. An example of simulated temperature profile with seepage simulated for an entire year .....159**

**Appendix I. Simulated temperature variations versus time for scenarios A2 to A5..... 160**

**Appendix J. Weekly average temperature profiles for scenarios B11 and B12..... 161**

**Appendix K. Photographs of concrete drill core from boreholes SEPI-1, 2 and 3..... 163**

**CURRICULUM VITAE**

## LIST OF TABLES

Table 4-1: Thermal-hydraulic property values for FEFLOW simulations. ....	48
Table 4-2: Parameter analysis: variations of hydraulic conductivity, anisotropy ratio and thermal conductivity for scenarios B1 to B9.....	71
Table 4-3: Bulk seepage simulations: annual average seepage rate for scenarios B1 to B9. ....	75
Table 5-1 Thermal-hydraulic parameters for anomalous seepage zone (Shija and MacQuarrie, 2015). ....	90
Table 5-2: Key parameter values for the concrete anomalous seepage simulations (A1 to A5) for the shallow temperature anomaly.....	92
Table 5-3: Annual average seepage rate, the increased seepage rate, and the annual and spatial average RMS deviations for scenarios A1 to A5.....	97
Table 5-4: Key parameter values for the interface anomalous seepage simulations (A6 to A9) for the shallow temperature anomaly.....	99
Table 5-5: Annual average seepage rate, the increased seepage rate, and the annual and spatial average RMS deviations for scenarios A6 to A9.....	103
Table 5-6: Annual average seepage rate, the increased seepage rate, and the annual and spatial average RMS deviations for scenarios A2, A6 and A10. ....	104
Table 5-7: Key parameter values for the anomalous seepage simulations (A11 to A14) for the deep temperature anomaly.....	107
Table 5-8: Annual average seepage rate, the increased seepage rate, and the annual and spatial average RMS deviations for scenarios A11 to A14.....	114
Table C.1: Headpond water temperature data measured by TLC meter on the SEP concrete structure.....	150

## LIST OF FIGURES

Figure 1-1: General types of rock-fill embankment dams: (a) central core; (b) inclined core; and (c) upstream facing (Narita, 2000). .....	3
Figure 1-2: Model for the development of failure by internal erosion in an embankment dam initiated by a) backward erosion and b) concentrated leak (Fell and Fry, 2007). .....	5
Figure 2-1: a) Location map and b) photo of the Mactaquac Generating Station. From Mactaquac Aquatic Ecosystem Study (MAES), <a href="http://canadianriversinstitute.com/research/mactaquac-aquatic-ecosystem-study">http://canadianriversinstitute.com/research/mactaquac-aquatic-ecosystem-study</a> . Copyright by Canadian Rivers Institute. ....	17
Figure 2-2: Photo of concrete diversion sluiceway and embankment dam along with a 3D model showing the locations of monitoring instrumentation. SEP: South End Pier, UWW: Upstream Wing Wall, DWW: Downstream Wing Wall (Butler, 2013). .....	18
Figure 2-3: BRUSens FO cable with jacket removed, blue and yellow jacketed optical fibres (one down-going and the other up-going) wrapped around central strength member at a ratio of 11.8 m of fibre for every meter of cable. ....	20
Figure 2-4: A screen capture of the Halo DTS system software showing an example of how temperature varied with distance along the optical fibre on Sep. 25, 2015. The up-going optic fibre cable broke in April, 2015. ....	20
Figure 2-5: Plots of seasonal variations in weekly average temperature versus depth in borehole SEPI-3 for years 2014 to 2017. The red lines in the 2014 and 2015 plots indicate the duration of the heating experiments during those two years. The red arrows and purple dashed rectangles indicate the location of anomalous temperature zones. ....	25
Figure 2-6: Plots of seasonal variations in daily average temperature versus depth in borehole SEPI-3 for years 2014 to 2017. The red arrow in the 2015 plot indicates the abrupt temperature shift observed on July 15, 2015. ....	26
Figure 2-7: Air, headpond and potential shallow seepage zone temperature time series from Jan. 2014 to Sep. 2017 (weekly average). Temperature anomalies are indicated by red arrows. ....	27
Figure 2-8: Weekly average headpond water level and elevations of the upper and lower boundaries of the shallow temperature anomaly from January, 2014 to July, 2017. ....	27
Figure 2-9: Photo taken in November, 2014 showing the vegetation (indicated by red circle in the photo) observed near the dam-concrete interface on the downstream slope of the embankment. The regularly-spaced beige objects on the downstream slope of the embankment are tarpaulins covering the electrodes used for Self-Potential measurements (Ringeri & Butler, 2016). ..	28
Figure 2-10: Photo taken in April 2017, showing the residual ice observed emanating from a concrete crack on the back of the SEP concrete wall at elevation about 95'. .....	29

Figure 2-11: Left: Conceptual model illustrating the locations of potential increased seepage on a longitudinal section through the clay till core/concrete interface. Right: Weekly average temperature-depth profiles for October, 2015 to May, 2016. ....30

Figure 2-12: Measurements from the inverted pendulum at Mactaquac SEP located near upstream face showing the seasonal thermal displacement of the SEP concrete in the longitudinal direction during 2004 (Sooch, 2016). ....31

Figure 2-13: Exaggerated deformed shapes of the longitudinal section of the SEP concrete, illustrating how AAR induced concrete expansion may cause a potential seepage zone at the clay till core/concrete interface. ....32

Figure 2-14: Comparisons of DTS measured temperature with thermistor and RTD temperature at different depths: a) Comparison of daily average DTS temperature and SEPI-3 thermistor temperature at depth about 33.4 m; b) Comparison of daily average DTS temperature and SEPI-2 thermistor temperature at depth about 21.3 m; c) Comparison of daily and hourly average DTS temperature and SEPI-2 RTD temperature at depth about 7.6 m. ....36

Figure 2-15: Description and verification of the calibration method applied on the instrument-calibrated data to remove the additional differential attenuation in the Stokes and anti-Stokes back scatter. a) Diagrams show the method of determining new offset and slope calibrated values. The instrument-calibrated temperature data is a sample data set measured at midnight on August 1, 2015. b) Differences between user-calibrated and instrument-calibrated temperature at depth about 33.4 m from June 2016 to June 2017 for the purpose of verifying the feasibility of the calibration method. ....40

Figure 2-16: User-calibrated plot of temperature versus depth from June 2016 to June 2017 (weekly average). ....41

Figure 4-1: 3D geometry of the dam-concrete structure generated in FEFLOW along with a longitudinal section through the clay till core/concrete interface. ....54

Figure 4-2: 2D supermesh and 3D meshed model domain for the dam/concrete structure. ....55

Figure 4-3: A longitudinal section through the clay till core/concrete interface showing details of the layer discretization within the 3D dam-concrete model domain. The circled numbers indicate the slice numbers, and the green dots represent observation points where simulated temperatures were extracted for comparison to the borehole DTS data. ....57

Figure 4-4: View of slice 8 showing the location of observation points (green dots) where temperatures were simulated for comparison to those measured along the DTS cable in borehole SEPI-3. ....58

Figure 4-5: Elements deactivated (in red) for layers of the zoned rock-fill dam segment (slice 1 to 5) to achieve different geometry from the concrete segment in one model domain. ....58

Figure 4-6: Hydraulic boundary conditions for the embankment and concrete segments of the model domain along with daily average time-varying headpond water elevations for June 1, 2016 – May 30, 2017. ....	60
Figure 4-7: Thermal boundary conditions for the embankment and concrete segments along with the slices specified as the SEP concrete wall and the dam/concrete interface. The multiple colored line segments shown in the headpond correspond to temperatures at various depths as shown in Figure 4-8 a). ....	61
Figure 4-8: Temperature time series applied for thermal boundary conditions: a) daily average headpond temperatures, averaged over 5 m intervals from the bottom of the model domain; b) daily average air temperature and concrete surface temperature; c) daily average foundation temperature.....	62
Figure 4-9: Distributions of different materials in the zoned rock-fill embankment dam. The yellow dashed line indicates the projection of SEPI-3 borehole into the embankment dam. ....	66
Figure 4-10: Simulated temperature variations versus time for scenarios B1 to B4. Several of the temperature contour lines have been highlighted in scenarios B1, B3 and B4 for easier visual comparison.....	73
Figure 4-11: Simulated temperature variations versus time for scenarios B5 to B8. The 8.5 °C temperature contour line has been highlighted in scenario B7 for easier visual comparison. ....	74
Figure 4-12: Bulk seepage simulations: comparison of seepage rate versus time for scenarios B1 to B4. ....	75
Figure 4-13: Bulk seepage simulations: comparison of seepage rate versus time for scenarios B1, B3 and B5 to B8. ....	75
Figure 4-14: Temperature variations versus time plots for a) DTS data and b) scenario B9, as well as c) seepage rate versus time for scenario B9.....	81
Figure 4-15: Comparisons of weekly average DTS temperature profiles (in blue) to the simulated bulk seepage temperature profile (in red) for scenario B9 at intervals of 35 days along with annual average RMS deviation as a function of depth. These temperature profiles were determined at borehole SEPI-3 (Figure 2-2). ....	82
Figure 5-1: Weekly average temperature versus depth (a) and temperature gradient versus depth (b) profiles for November 2016 to March 2017.....	84
Figure 5-2: 3D geometry and meshing of the simplified cubic model. The z direction is magnified five times for easier viewing of the layers. ....	86
Figure 5-3: Simulated temperature versus depth and temperature gradient versus depth profiles for Case 1 (a, b) and Case 2 (c, d) with borehole-interface separations varying from 0.1 m to 0.6 m. ....	88
Figure 5-4: Longitudinal section of the dam/concrete structure through the clay till core-concrete interface and the SEPI-3 borehole (a) along with the slice views of the 3D model illustrating the location and geometry of the simulated seepage zone in the concrete (b) and embankment (c). ....	91

Figure 5-5: Seepage rate (daily average) versus time for scenarios A1 to A5 and B9 (bulk seepage). .....93

Figure 5-6: Simulated temperature variations versus time for scenario A1.....93

Figure 5-7: Comparisons of weekly average DTS temperature profiles (in blue) to the simulated anomalous temperature profile (in red) and bulk seepage profile (in dashed green) for January, February and March in 2017, along with annual average RMS deviation as a function of depth for scenarios a) A1, b) A2, and c) A3.....95

Figure 5-8: Comparisons of weekly average DTS temperature profiles (in blue) to the simulated anomalous temperature profile (in red) and bulk seepage profile (in dashed green) for January, February and March in 2017, along with annual average RMS deviation as a function of depth for scenarios a) A4 and b) A5. ....96

Figure 5-9: Simulated temperature variations versus time for scenarios A6 to A9. .... 100

Figure 5-10: Seepage rate (daily average) versus time for scenarios A6 to A9 and B9 (bulk seepage). ..... 101

Figure 5-11: Comparisons of weekly average DTS temperature profiles (in blue) to the simulated anomalous temperature profile (in red) and bulk seepage profile (in dashed green) for January, February and March in 2017, along with annual average RMS deviation as a function of depth for scenarios a) A6 and b) A7. .... 101

Figure 5-12: Comparisons of weekly average DTS temperature profiles (in blue) to the simulated anomalous temperature profile (in red) and bulk seepage profile (in dashed green) for January, February and March in 2017, along with annual average RMS deviation as a function of depth for scenarios a) A8 and b) A9. .... 102

Figure 5-13: Seepage rate versus time for scenarios A2, A6 and A10 and B9 (bulk seepage)..... 105

Figure 5-14: Comparisons of weekly average DTS temperature profiles (in blue) to the simulated anomalous temperature profile (in red) and bulk seepage profile (in dashed green) for January, February and March in 2017, along with annual average RMS deviation as a function of depth for scenario A10. .... 105

Figure 5-15: Simulated temperature variations versus time for scenario A10. .... 106

Figure 5-16: Temperature distribution within the concrete, 0.5 m from its interface with the embankment, for scenario A11 on January 1, 2017..... 108

Figure 5-17: Simulated temperature variations versus time for scenarios A11 to A14. 110

Figure 5-18: Comparisons of weekly average DTS temperature profiles (in blue) to the simulated anomalous temperature profile (in red) and bulk seepage profile (in dashed green) for August, September and October in 2017, along with annual average RMS deviation as a function of depth for scenarios a) A11 and b) A12..... 111

Figure 5-19: Comparisons of weekly average DTS temperature profiles (in blue) to the simulated anomalous temperature profile (in red) and bulk seepage profile (in

dashed green) for August, September and October in 2017, along with annual average RMS deviation as a function of depth for scenarios a) A13 and b) A14.....	112
Figure 5-20: Seepage rate (daily average) versus time for scenarios A11 to A14 and A3 as well as bulk seepage scenarios B9 and B10. ....	113
Figure 5-21: Comparisons of daily average DTS temperature profiles on a) December 19, 2016/2017, and b) on February 16, 2017/2018. ....	115
Figure 5-22: Photos of the back of the SEP concrete wall showing that an icefall emanating from a crack in the concrete at elevation 95' in April 2017 had disappeared in April 2018. ....	116
Figure 5-23: Temperature distribution within the embankment along the interface on September 1, indicating that the headpond water temperature is higher than the temperature at the clay till core at elevation 95' in September. ....	120
Figure 5-24: Schematic horizontal slice through the dam-concrete structure at elevation 95' illustrating how the water flow into a fracture zone in the concrete from the embankment and headpond would influence the borehole temperature in September depending on the horizontal extent of the fracture: a) extent from the interface to the outer concrete wall; b) reduced extent, not reaching the interface. ....	121
Figure 5-25: Comparisons of weekly average DTS temperature profiles (in blue) to the simulated anomalous temperature profile (in red) and bulk seepage profile (in dashed green) for scenarios A11 and A15 in September and October in 2017. Note that the simulated profiles in red match the observed profiles in blue much more closely for scenario A15, in which the deep concrete seepage zone is effectively disconnected from the embankment. ....	122
Figure B.1: Headpond temperature versus depth time series.....	146
Figure B.2: MAES project map showing the location of thermograph strings in the headpond. The site 24 is indicated by red arrow.....	147
Figure C.1: Jib boom structure installed on the SEP concrete structure to facilitate measurements of water temperature versus depth.....	148
Figure E.1: Design drawing for a cross section through the middle of the Mactaquac embankment dam, approximately 300 m away from the dam/concrete interface, showing zonation of the construction materials, and upstream inclination of the core.....	152
Figure E.2: Photo of the clay till core materials distribution looking from the SEP to the south at the time of dam construction in 1967 indicating that the core was made wider at its southern abutment (NB Power).....	153
Figure F.1: Simulated temperature distribution along the dam/concrete interface (slice 6 in Figure 4-3) for bulk seepage scenario B9 from June 1, 2016 to Nov. 1, 2016.....	154
Figure F.2: Simulated temperature distribution along the dam/concrete interface (slice 6 in Figure 4-3) for bulk seepage scenario B9 from Dec. 1, 2016 to May 1, 2017.....	155

Figure F.3: Simulated temperatures on slice 1 within the embankment, 30.6 m from top of the SEP interface, for bulk seepage scenario B9; June 1, 2016 to Nov. 1, 2016.....	156
Figure F.4: Simulated temperatures on slice 1 within the embankment, 30.6 m from top of the SEP interface, for bulk seepage scenario B9; Dec 1, 2016 to May 1, 2017.....	157
Figure G.1: Interpreted clay till core-concrete interface. Preferred interpretation shown in black. Red line shows recommended trajectory for seepage monitoring boreholes.....	158
Figure H.1: An example of the simulated temperature versus depth plot from June 1, 2016 to June 1, 2017 for the case of a seepage zone simulated in the concrete and along the interface for an entire year.....	159
Figure I.1: Simulated temperature variations versus time for scenarios S2 to S5.....	160
Figure J.1: Comparisons of weekly average DTS temperature profiles (in dashed green) to the simulated bulk seepage temperature profiles for scenarios 9 (in blue) and 11 (in red) at intervals of 35 days, along with annual average RMS deviation as a function of depth for scenario 11.....	161
Figure J.2: Comparisons of weekly average DTS temperature profiles (in dashed green) to the simulated bulk seepage temperature profiles for scenarios 9 (in blue) and 12 (in red) at intervals of 35 days, along with annual average RMS deviation as a function of depth for scenario 12.....	162
Figure K.1: Plan view of the top of the SEP showing locations of the collars of boreholes SEPI 1, 2 and 3 below the road. (Drawing by A. Ringeri).....	163
Figure K.2: Photo of the concrete core drilled from borehole SEPI 1 between slant depth 0' to 27' (slant depth 0 to 8.2 m).....	164
Figure K.3: Photo of the concrete core drilled from borehole SEPI 2 between slant depth 0' to 30' (slant depth 0 to 9.1 m).....	164
Figure K.4: Photo of the concrete core drilled from borehole SEPI 3 between slant depth 0' to 35' (slant depth 0 to 10.7 m).....	165
Figure K.5: Photo of the concrete core drilled from borehole SEPI 2 showing the steeply (red arrow) and gently (blue arrows) dipping fractures at a slant depth of approximately 50' (15.24 m). The dashed yellow lines are approximately parallel to the core axis.....	165
Figure K.6: Photo of the concrete core drilled from borehole SEPI 3 showing the steeply dipping fracture at slant depth a) 27' (8.2 m); b) 29' (8.8 m); and c) 67' (20.4 m). The shallow angles of the steeply dipping fractures relative to the core axis and the observed water staining are indicated by red and green arrows, respectively. The dashed yellow lines are approximately parallel to the core axis. ....	166

## LIST OF SYMBOLS AND ABBREVIATIONS

### Symbols

$A$	-	calibration parameter for optical fibre
$a_0$ to $a_6$	$ML^{-3}$	coefficients for water (density)
$C_e$	$ML^{-1}K^{-1}T^{-2}$	effective volumetric heat capacity
$C_p$	$L^2K^{-1}T^{-2}$	specific heat
$C_s$	$ML^{-1}K^{-1}T^{-2}$	volumetric heat capacity of solids
$C_w$	$ML^{-1}K^{-1}T^{-2}$	volumetric heat capacity of water
$c$	-	cloud coefficient
$\mathbf{D}$	$L^2T^{-1}$	tensor of mechanical dispersion
$\mathbf{e}$	1	gravitational unit vector
$F$	K	freezing index
$f$	-	coefficient for frost depth calculation
$g$	$LT^{-2}$	gravitational acceleration
$h$	L	hydraulic head
$\mathbf{I}$	1	unit tensor
$K$	$LT^{-1}$	saturated hydraulic conductivity
$K_r$	-	relative (unsaturated) hydraulic conductivity
$k$	-	topography coefficient
$k_1$	-	latitude coefficient
$L$	L	distance along the direction of flow
$l$	-	pore-connectivity parameter

$\Delta l$	L	maximum length of the finite element
$m$	-	van-Genuchten curve fitting parameter
$n$	-	van-Genuchten curve fitting parameter
P	$ML^{-1}T^{-2}$	fluid pressure
$P_e$	-	Péclet number
$P_{as}$	$L^2MT^{-3}$	power of anti-Stokes
$P_s$	$L^2MT^{-3}$	power of Stokes
q	$LT^{-1}$	specific discharge or Darcy velocity or Darcy flux
<b>q</b>	$LT^{-1}$	Darcy flux vector
S	$MT^{-3}$	total solar radiation
s	-	saturation
$s_e$	-	effective saturation
$s_r$	-	residual saturation
$s_s$	-	maximum saturation
T	K	temperature
$T_c$	°C	temperature in degrees Celsius
$\Delta T$	K	temperature increment
t	T	time
u	$LT^{-1}$	average linear velocity
y	L	distance along the DTS cable
Z	L	frost depth
z	L	elevation head
$\alpha$	$L^{-1}$	van-Genuchten curve fitting parameter

$\alpha_L$	L	longitudinal dispersivity
$\alpha_T$	L	transverse dispersivity
$\alpha_s$	-	concrete absorption coefficient
$\Delta\alpha$	$L^{-1}$	differential attenuation
$\beta$	-	offset calibrated value
$\gamma$	K	shift in energy between a photon at the wavelength of the incident laser and the scattered Raman photon
$\delta$	-	van-Genuchten curve fitting parameter
$\varepsilon$	-	porosity
$\kappa$	$L^2$	intrinsic permeability
$\lambda_e$	$MLK^{-1}T^{-3}$	effective thermal conductivity
$\lambda_s$	$MLK^{-1}T^{-3}$	thermal conductivity of solids
$\lambda_w$	$MLK^{-1}T^{-3}$	thermal conductivity of water
$\mu$	$ML^{-1}T^{-1}$	dynamic viscosity
$\mu_0$	$ML^{-1}T^{-1}$	reference dynamic viscosity
$\rho$	$ML^{-3}$	fluid density
$\rho_0$	$ML^{-3}$	reference fluid density
$\sigma$	$MK^{-1}T^{-3}$	surface conductance
$\psi$	L	pressure head
$\omega$	-	slope calibrated value
$\nabla$	-	Gradient operator

## **Abbreviations**

<b>AAR</b>	<b>Alkali-Aggregate Reaction</b>
<b>ASR</b>	<b>Alkali-Silica Reaction</b>
<b>DWW</b>	<b>Downstream Wing Wall</b>
<b>DTS</b>	<b>Distributed Temperature Sensing</b>
<b>FEFLOW</b>	<b>Finite Element Subsurface Flow System</b>
<b>FO</b>	<b>Fibre Optic</b>
<b>IRFTA</b>	<b>Impulse Response Function Thermic Analysis</b>
<b>MAES</b>	<b>Mactaquac Aquatic Ecosystem Study</b>
<b>NASA</b>	<b>National Aeronautics and Space Administration</b>
<b>RTD</b>	<b>Resistance Temperature Detector</b>
<b>RMS</b>	<b>Root Mean Square</b>
<b>SEP</b>	<b>South End Pier</b>
<b>SP method</b>	<b>Self-potential method</b>
<b>TLC meter</b>	<b>water Temperature, Level and Conductivity meter</b>
<b>UPS</b>	<b>Uninterruptible Power Supply</b>
<b>UWW</b>	<b>Upstream Wing Wall</b>
<b>2D</b>	<b>Two-dimensional</b>
<b>3D</b>	<b>Three-dimensional</b>

# **Chapter 1 : Introduction**

## **1.1 Background**

Earthen embankment dams, which are constructed of earth and rock materials, are widely used to contain water supply and hydroelectric reservoirs, as well as wastes such as those produced by mining operations. Earthen dams must be designed and maintained to safely control seepage. One of the major reasons for embankment dam failure is internal erosion and piping, caused by the loss of fine-grained materials due to localized seepage flow (Fell et al., 1992). It is therefore important to ensure that any anomalous seepage giving rise to internal erosion be identified and remediated at an early stage.

Temperature monitoring, which can give real time information on seepage conditions, has been employed to investigate dam seepage for many years (Cuong et al., 2017a). The introduction of Distributed Temperature Sensing (DTS) technology, which allows for continuous temperature measurements along a cable to give high information density, makes temperature monitoring more effective when compared to conventional point measurements (Aufleger et al., 2007).

In this study, spatial and temporal variations of temperature have been monitored by a DTS system installed near the interface between the compacted till core of an embankment dam and an adjoining concrete diversion sluiceway structure at the Mactaquac Generating Station, located on the Saint John River approximately 20 km upstream of Fredericton, NB. Numerical simulations have been applied to find possible

explanations for the temperature anomalies observed from the passive temperature monitoring.

## **1.2 Dams and internal erosion processes**

Depending on the predominant construction material used, embankment dams can be classified into two types: earth-fill dams and rock-fill dams. Rock-fill dams can be further subdivided into three groups based on the location of the low permeability zone as follows: 1) central core, 2) inclined core and 3) upstream facing (U.S. Army Corps of Engineers, 2004; Narita, 2000). Generalized cross sections of these different types of rock-fill dams are shown in Figure 1-1. The main body of a rock-fill dam is typically composed of largely fragmented rocks forming zones or shells, along with a core that is constructed from low permeability earth-fill materials for the purpose of minimizing seepage. The core is separated from the rock shells by a filter zone that has a low porosity to prevent the erosion of the core materials, but a high permeability relative to the core to allow seepage drainage (Fell et al., 1992). The selection of embankment dam type for a specific location is affected by various factors including topography, environment, available construction materials, foundation conditions and more (Narita, 2000; Fell et al., 1992).

All dams are designed and constructed to allow some seepage from the headpond (i.e. reservoir) to the downstream toe or face of the structure. Seepage only becomes a concern when it leads to internal erosion. Statistical analyses by Foster et al. (2000b) indicate that about 50% of embankment dam failures in the world before year 1999 were

due to internal erosion. The location of the internal erosion may occur within the embankment, in the foundation, or from the embankment into the foundation (Fell et al., 1992). The well-known failure of the Teton Dam in Idaho, United States reported by Seed and Duncan (1981), and the failure of the nearby Fontenelle Dam reported by Baker (2011) were both due to internal erosion of the embankment through the foundation. The Baldwin Hills Dam failure, caused by internal erosion of the embankment dam body, is discussed by Sharma and Kumar (2013). Additional case histories of embankment dam failures caused by internal erosion, along with potential factors that contribute to dam failures associated with internal erosion, are presented by Miedema (2004).

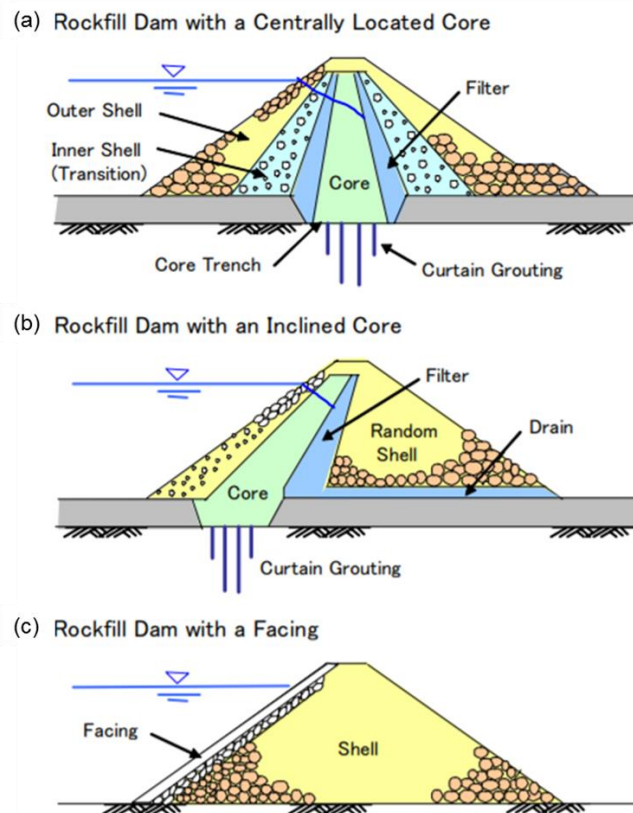


Figure 1-1: General types of rock-fill embankment dams: (a) central core; (b) inclined core; and (c) upstream facing (Narita, 2000).

The process of internal erosion and piping can be divided into four phases: initiation, continuation, progression, and breach (Fell & Fry, 2007). There are three ways for initiation of internal erosion in a rock-fill dam with an earth core: backward erosion, concentrated leak, and suffusion (Fell et al., 1992). Figure 1-2 depicts internal erosion in the embankment initiated by backward erosion and a concentrated leak. Backward erosion starts at an interface between materials having a large difference in grain size, such as core and filter, fine and coarse filter, or filter and rock-fill zone. The erosion then gradually progresses backward to the upstream side of the embankment. A concentrated leak may occur in a crack or a soft zone emanating from the source of water to an exit point (Mattsson et al., 2008). Cracks can form due to differential settlements, desiccation, freezing and thawing, and hydraulic fracture (Fell & Fry, 2007). The concentration of flow causes erosion along the walls of cracks, which can further intensify a concentrated leak. Suffusion is the process where the fine particles of the soils are eroded from the matrix of coarser particles by seepage flow thus making the soils internally unstable (Fell & Fry, 2007). The continuation of internal erosion depends highly on the grading of the filter; if the filter cannot stop the concentrated leak, erosion will continue (Lagerlund, 2009). The progression stage of internal erosion and piping is affected by several issues including the hydraulic gradient, the ability of soils to support a roof of the pipe, the geometry of the eroding hole, and flow limitations (Fell et al., 2003; Fell & Wan, 2005). Breach is the final phase of internal erosion; it may occur due to piping or instability of the downstream slope. More details about internal erosion mechanisms can be found in Fell and Fry (2007) and a discussion of the time required for development of internal erosion and piping can be found in Fell et al. (2003).

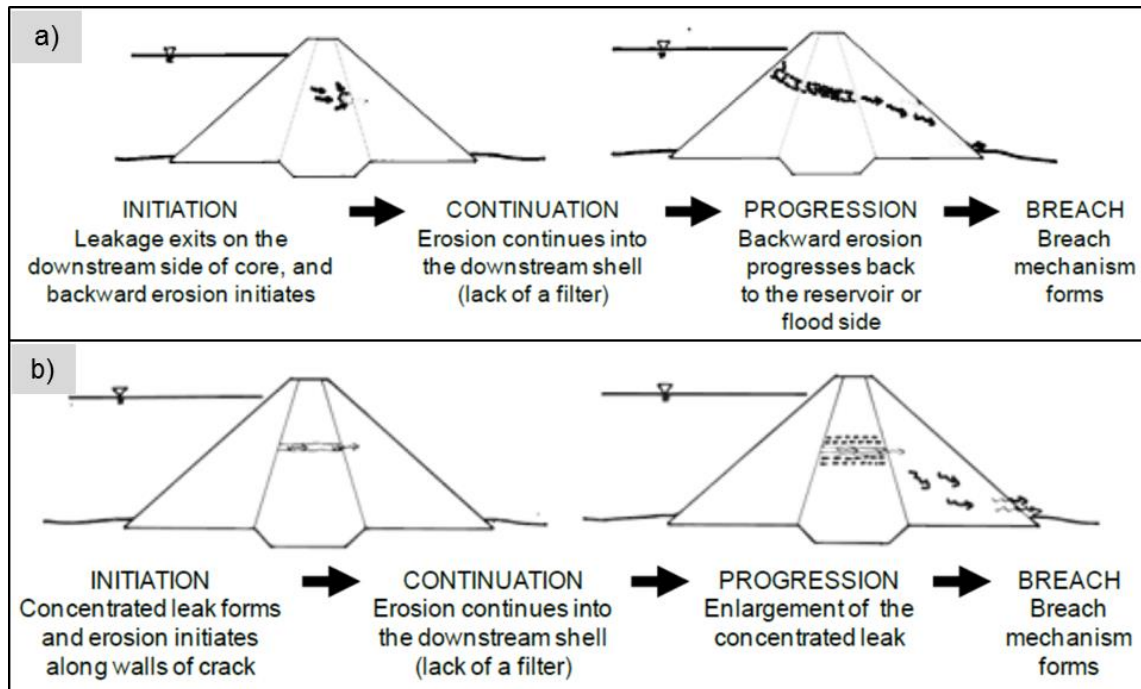


Figure 1-2: Model for the development of failure by internal erosion in an embankment dam initiated by a) backward erosion and b) concentrated leak (Fell and Fry, 2007).

The interface between an earth-fill embankment and a concrete structure, such as a spillway or sluiceway structure, is another common region for cracking and internal erosion. This is mainly due to difficulties in compaction of soils at the earth-concrete interface during construction, which in turn contributes to a low quality and more permeable interface (Lagerlund, 2009). Cracks induced by differential settlement can expand and develop further by hydraulic fracturing if the reservoir water pressure exceeds the total normal stress on the earth-concrete interface fracture plane (Mattson et al., 2008; Mesri & Ali, 1988). As the concrete acts as a relatively impervious structure, and the permeability of the core is low, seepage water may enter and flow along cracks more rapidly than it can flow through the pores of the dam core. Several cases of dam breach caused by internal erosion of the earth materials along the contact between an embankment and concrete spillway were documented by Foster et al. (2000a) and Kolala

et al. (2015). Most of these failures occurred on the first filling of a reservoir and within the first 5 years of operation as indicated by Foster et al. (2000a).

### **1.3 Temperature monitoring for seepage detection**

Seepage monitoring is an indispensable component of embankment dam safety. Besides the common visual inspection for dam surveillance, different monitoring methods have been developed to detect potential leakage within an embankment dam and its foundation. Piezometers can be installed in boreholes to measure pore water pressure, which is sensitive to increased permeability of the soil (Ridley et al., 2003). Temperature monitoring can detect anomalous temperature variations triggered by increased seepage flow (Aufleger et al., 2007). Several geophysical techniques can be applied to detect anomalous seepage: the electrical resistivity method and ground penetrating radar are sensitive to changes of the electrical resistivity and permittivity, respectively, which are in turn both related to changes of porosity, saturation and clay content (Johansson, 1997); seismic measurements can indicate anomalous seepage by identifying areas with seismic waves travelling at lower velocity (Hickey et al., 2009); the self-potential method responds to the electrical currents generated by the flow of water through electrokinetic coupling (Ringeri & Butler, 2016).

Among these various methods, temperature monitoring, which can provide real-time information on seepage conditions (Yousefi et al., 2013), is now regarded as a powerful tool for seepage monitoring and evaluation. Johansson (2009) thoroughly discussed the application of temperature measurements to seepage monitoring of

embankment dams including its fundamentals, different measurement methods and evaluation methods, along with its application at Swedish dams. There are two basic types of temperature monitoring: the passive method (gradient method) and the active heating method (i.e. heat injection with subsequent temperature monitoring).

Passive monitoring relies on the natural seasonal temperature variations within the dam body, which are mainly affected by air temperature, reservoir water temperature, and foundation temperature. In general, seasonal reservoir water temperature oscillations do not propagate deep into the dam, and the temperature fluctuations within the dam should be relatively stable especially at distances far from the reservoir (Velásquez, 2007). However, when anomalous seepage occurs, temperature anomalies will be transported into the dam structure by means of convection and the normal temperature field will be distorted (Aufleger et al., 2008). The magnitude and velocity of seepage flow may be estimated by means of the time lag and intensity of the temperature anomaly (Aufleger et al., 2007; Sjö Dahl and Johansson, 2012). Moreover, long term monitoring is required to observe seasonal temperature variations.

An example of successful application of passive monitoring for anomalous seepage detection was documented by Smith and Konrad (2008). They used seasonal variations in reservoir temperature measured by point sensors along the submerged upstream face of a dam, and within the embankment dam itself, to identify a seepage zone within the compacted till core. The temperature data were analyzed using a simplified 2D finite element model with coupling between heat transport and water flow to assess the hydraulic conductivity contrast within the core; the simulated temperature profiles provided a reasonable fit to the observed temperature patterns. The results

showed that the hydraulic conductivity within the enhanced seepage zone was approximately 20 times larger than in the surrounding core.

In contrast, the active method combines heating together with temperature measurements. Temperature data are collected before and during the heating process. Leakage zones can then be detected by comparing the temperature measurements before heating and at the peak of heating because zones with higher seepage usually have higher heat loss leading to a lower peak temperature (Dornstädter, 2013).

Cuong et al. (2017b) assessed the capability of the active method for seepage evaluation through numerical simulations of an actual dam. A 15 m homogeneous dam segment containing a horizontal permeable layer measuring 1 m x 3 m (height x width) in the vertical section was simulated. The hydraulic conductivity of the horizontal layer ( $3.0 \times 10^{-5}$  m/s) was  $10^3$  times larger than that of the dam ( $3.0 \times 10^{-8}$  m/s). A vertical line heat source in a standpipe was simulated at the centre of the horizontal layer, and 1, 2 and 3 m away from the edge of the horizontal layer. The results showed that the application of high-power line heat sources and temperature measurements in standpipes were able to detect anomalous seepage within 6 m.

Both active and passive monitoring methods have their own advantages and disadvantages. Originally the active method was developed for applications where the gradient method was not applicable, which is the case if there is neither sufficient temperature gradients between the reservoir water and the location(s) of temperature measurement, nor adequate seasonal temperature variations in the reservoir water (Aufleger et al., 2007). In terms of data collection, the active method only requires a

short time, even a few days, while the passive method requires several months or years to adequately capture the seasonal temperature variations. However, the temperature data collected using the passive method can be more useful for seepage rate analysis because the seasonal temperature variations within the dam are directly proportional to seepage velocity at high seepage rates (Yousefi, 2013; Cuong et al., 2017a).

Temperature data within an embankment dam can be collected at a single point, multiple points, or in lines (Johansson, 2009). Conventional temperature sensors including thermocouples, junction temperature sensors, resistance temperature detectors (RTDs) and thermistors are limited in their sensitivity and spatial resolution to detect small and local seepage characteristics (Hoffmann et al., 2007). Recent experience has shown that Distributed Temperature Sensing (DTS) technology based on optical fibre sensors is an effective and economical solution to temperature monitoring in embankment dams.

#### **1.4 Distributed Temperature Sensing (DTS) technology**

DTS technology is based on the temperature sensitive properties of optical fibre (Aufleger et al., 2007). The measuring instrument uses a laser source to emit a high intensity light signal into the optical fibre. The backscattered light is then detected in the DTS control unit and analyzed with Raman spectroscopy, providing Stokes and anti-Stokes intensities as a function of distance along the optical fibre (Dornstädter, 2013). The intensity ratio of Stokes to anti-Stokes contains the temperature information at the scattering point. The key feature is that the optical fibre is the sensor itself, and it can be

used to measure the real-time temperature fluctuation along its entire length (Johansson, 2009).

The advantages of the fibre optic cable when compared to conventional temperature measurements are summarised as follows (Aufleger et al., 2007; Velásquez, 2007; Khan et al., 2010b):

- Long-range measurements: up to 30 km in length.
- High information density: high spatial and temperature resolutions (as precise as 1 m and 0.01 °C, respectively).
- Commercial viability: low cost by using fibre optic cable.
- Suitable for harsh environments: protection of the cable and external protection may be employed.
- Simple and flexible installation of the cables: sensors are installed permanently.

#### *1.4.1 Temperature data collection by DTS systems*

Installation of fibre optic cable at a strategic location near or within a dam is important for successful seepage detection. Most DTS systems have been installed in existing dams where the fibre optic cable may be deployed in existing standpipes or buried along the downstream dam toe (Johansson, 2009). An experiment performed at Hylte Dam demonstrated that a fibre optic cable installed below the groundwater table in the downstream toe of the dam can detect small seepage changes (Johansson, 2009). Artières et al. (2010) also showed that a fibre optic cable can detect seepage successfully when placed in an unsaturated zone, such as the dry dike of the Oraison canal. In the

latter study, locations of all artificial seepage paths were detected by analysing the DTS data using the Impulse Response Function Thermic Analysis (IRFTA) model.

In the case of new embankment dams, fibre optic cables can be installed behind waterproof upstream facings or behind a central impervious core during construction (Tanchev, 2014). At these two locations, cables are exposed to tensile forces and lateral pressure due to the deformations and the stresses within the dam (Aufleger et al., 2011). Thus, the protection of cables and laboratory tests to evaluate the influence of deformations and stresses on the cables and temperature measurements are indispensable. Successful seepage monitoring performed at the Knezovo Dam in Macedonia proved the applicability of a DTS monitoring system in the central part of an embankment dam (Aufleger et al., 2011). The DTS cable was installed longitudinally in the transition zone behind the asphalt core. Significant seepage flow was detected using the active heating method. More case studies that have used distributed optical fibres for seepage studies are presented in Artières et al. (2007), Johansson (2009), Inaudi et al. (2013) and Zhu et al. (2008). Radzicki (2014) also presented recommendations on optimal locations for fibre optic cables in dams considering their size, type, construction, foundation conditions and monitoring purposes.

There are also other locations that may be useful for fibre optic cable installation, for example, near the interface between earth materials and adjoining concrete structures. Shija and MacQuarrie (2015) used numerical simulations to investigate the feasibility of using active heat injection methods to identify anomalous seepage at the interface between an earth embankment dam and adjoining concrete structure. The thermal responses relative to the distance between the heat injection location and

temperature monitoring borehole, the temperature sensitivity to borehole-interface separation distances, and to seepage rates within the anomalous seepage zone were evaluated. The results showed that the preferred location for temperature monitoring is within the concrete structure and as close to the earth-concrete interface as feasible.

#### *1.4.2 Methods used to analyze DTS temperature data*

Usually, the data collected by the DTS/passive method in dykes or at the dam toe cannot be used directly for leakage detection. Many other environmental factors may influence the acquired temperature data, such as drainage pipes, ground heterogeneities, precipitation, and the temperature difference between seepage water and the ground in which the fibre cable is buried (Khan, 2010a). In this case, methods for advanced temperature analysis are necessary and useful. Various models have been developed for analysis of temperature data acquired by DTS sensors. Khan et al. (2010a) introduced a source separation method to separate different thermal contributions (sources) from the raw temperature data. Decomposition of the raw temperature data can be performed using singular value decomposition (SVD) and independent component analysis (ICA) based on the assumption that the sources are mutually independent. Khan et al. (2010b) developed another method that can be used for real-time early warning based on the assumption that anomalies such as leakages show daily temperature variations that are different from the non-anomalous zones. Both of these methods were validated on two different sites equipped with fibre optic temperature sensors along a dike, whereby anomalously increased seepage was detected.

Another approach to temperature analysis is based on the estimation of physical parameters associated with seepage. The Impulse Response Function Thermic Analysis (IRFTA) model, which was proposed by Radzicki and Bonelli (2011), allows for seepage identification and its intensity estimation. The measured temperature is regarded as a superposition of the responses related to the reservoir water and the air temperatures, while other thermal contributions like geothermal and freezing processes, radiation and wind influence are neglected. That is to say, only the heat transport mechanisms of conduction and convection are analyzed. Beck et al. (2010) further validated the efficiency of the source separation model and IRFTA model for seepage monitoring through several tests at controlled and industrial sites with the application of fibre optic sensors. Descriptions of other models developed in the past decade for analysis of passive temperature measurements in earthen hydraulic structures can be found in Radzicki (2014).

Besides the temperature data analysis models discussed above, seepage and temperature variations within the dam body can also be simulated using numerical methods. Song and Yosef (2017) used a finite difference method to simulate a two-dimensional dam region with a 0.02 m thick crack in the clay till core. The simulation results showed that the location of the crack could be clearly identified in the temperature profiles. Moreover, the study also showed the possibility that temperature data might serve as a tool to diagnose prior seepage conditions within a dam before temperature monitoring based on the fact that there is a time lag between the seepage time and heat transfer. Opaliński et al. (2016) applied a two dimensional, thermal-hydraulic finite element model to verify the hypothesis of potentially intensified seepage

processes in the foundation of Kozłowa Góra Dam in Poland. The simulation results were compared to measured temperature data, and elevated levels of seepage were confirmed between sheet piles and the impermeable foundation layer, although not enough to result in significant internal erosion processes in the foundations. This study also demonstrated the high sensitivity of the thermal methods to seepage rate changes. More discussions about the numerical modelling method for seepage investigation are presented in Chapter 3.

### **1.5 Research objectives and significances**

The main purpose of this research is to investigate, using numerical simulations, the passive temperature data collected by a DTS system installed at the northern end of the embankment dam at the Mactaquac Generating Station, and to provide possible explanations for the observed temperature anomalies. The focus of the seepage investigations is at the interface between the compacted clay till core of the embankment dam and the adjoining concrete diversion sluiceway structure. The specific objectives of this research are to: 1) collect and process the field temperature data monitored by the DTS system; 2) develop a three-dimensional finite element model to simulate coupled heat transport and water seepage within the dam-concrete structure and investigate the sensitivity of temperature within the dam to various thermal-hydraulic parameters; 3) simulate the observed seasonal temperature variations along the dam-concrete interface, using multiple seepage scenarios to provide possible interpretations for the observed temperature anomalies.

Although temperature monitoring and heat transport modelling have been widely applied within the interior of embankment dams, this application at Mactaquac appears to be the first to specifically investigate seepage at the interface between an earth embankment and a concrete structure using thermometry. This research is expected to provide a reliable scientific basis for using passive thermal monitoring measurements and numerical modelling to detect seepage. In that sense, the investigations of temperature sensitivity to seepage conditions, and the development of recommendations for effective passive DTS monitoring at interfaces will also be important outcomes of this research.

## **1.6 Thesis structure**

The body of this thesis is organized into five chapters (Chapter 2-6). The next chapter (Chapter 2) introduces the study site and data acquisition as well as the processing of field temperature data obtained from the DTS system. Chapter 3 provides theoretical principles related to the coupling between seepage and heat transport in dams. Chapter 4 presents the numerical model for the dam-concrete structure and parametric studies for bulk seepage simulations. Chapter 5 presents numerical modelling for anomalous seepage analysis. Quantitative analysis of the differences between the simulated results and the measured DTS data is also performed. Finally, Chapter 6 presents the conclusions of this study.

## **Chapter 2 : Field data collection, processing and analysis**

### **2.1 Instrumentation and data acquisition**

The study site is at NB Power's Mactaquac Generating Station, located on the Saint John River, 20 km upstream from Fredericton, New Brunswick, Canada (Figure 2-1). The station was constructed in stages from 1964 to 1980 and is the largest hydroelectric generating facility in the Maritime Provinces with a maximum generating capacity of 670 MW (Gilks et al., 2001). The main dam structure is a zoned rock-fill embankment dam with a central inclined clay till core (more details are presented in Section 4.2.3). The maximum height of the dam above the foundation is about 58 m and the crest length is about 500 m (Conlon & Ganong, 1966). The adjacent concrete structures, containing gates and power generating infrastructure, have been experiencing expansion and degradation problems as a result of alkali-aggregate reaction (AAR), in the specific form of alkali-silica reaction (ASR), and various innovative remedial measures have been undertaken since 1985 to extend the life of the structure (Gilks et al., 2001). In this study, seepage investigations were performed at the interface between the compacted clay till core of the embankment dam and the adjoining concrete diversion sluiceway structure (Figure 2-2). This area has also been investigated by Ringeri et al. (2016), using self-potential (SP) monitoring; their study results suggested the presence of foundation seepage, but the investigation did not include data collection and 3D modelling that was specifically intended to detect seepage along the embankment/concrete interface.



Figure 2-1: a) Location map and b) photo of the Mactaquac Generating Station. From Mactaquac Aquatic Ecosystem Study (MAES), <http://canadianriversinstitute.com/research/mactaquac-aquatic-ecosystem-study>. Copyright by Canadian Rivers Institute.

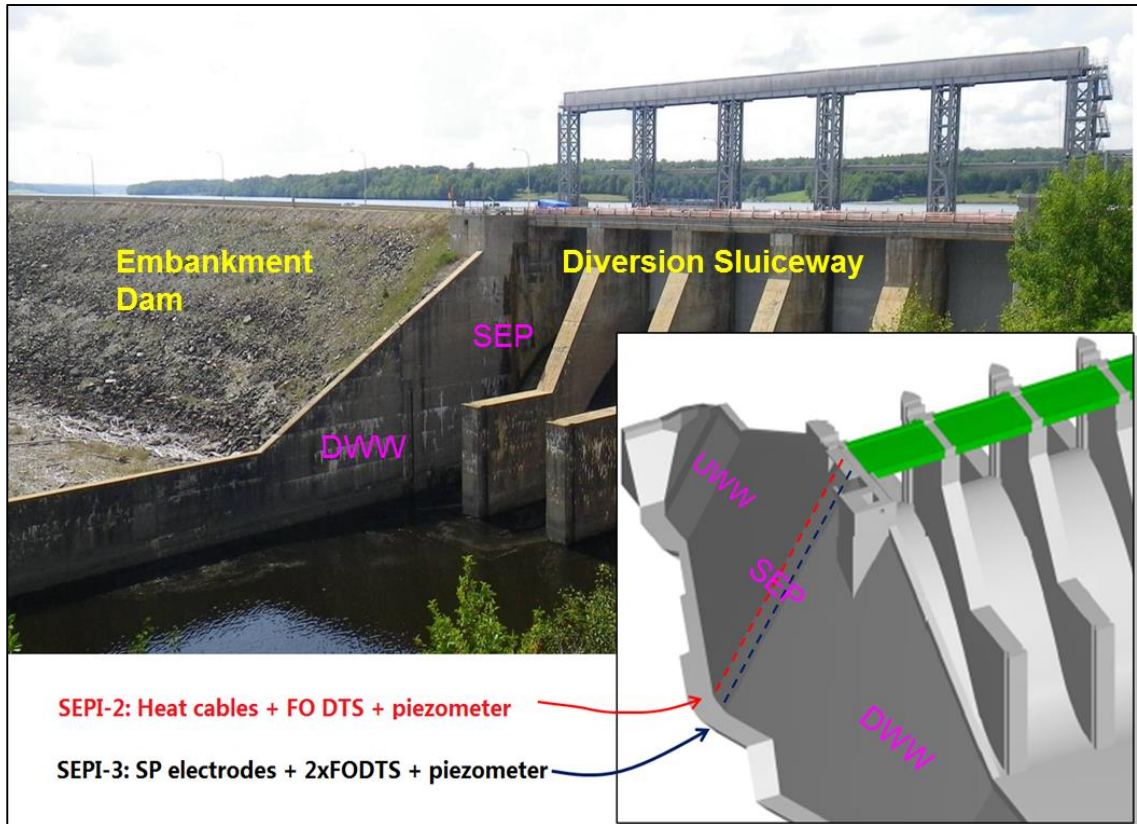


Figure 2-2: Photo of concrete diversion sluiceway and embankment dam along with a 3D model showing the locations of monitoring instrumentation. SEP: South End Pier, UWW: Upstream Wing Wall, DWW: Downstream Wing Wall (Butler, 2013).

During the summer and fall of 2013, two 50 m boreholes were drilled sub-vertically into the south end pier (SEP) of the concrete diversion sluiceway to allow installation of seepage monitoring sensors including DTS cables and SP electrodes. As shown in Figure 2-2, the boreholes were drilled nearly parallel to the steeply inclined face of the SEP that abuts the clay till core of the embankment dam. The two holes were drilled approximately 3 m apart under the asphalt of the roadway crossing the diversion sluiceway, and each is estimated to lie within 0.5 m of the interface along its entire length (Butler, 2013). The downstream hole, SEPI-3, was equipped with SP electrodes and one BRUSens multi-mode fibre optic (FO) DTS cable. The upstream hole, SEPI-2,

was equipped with one heating cable. Each borehole was additionally equipped with one vibrating wire piezometer with integrated thermistor and one single-mode FO cable that was connected to prototype DTS instrumentation installed and operated by Dr. Bruce Colpitts and his students from UNB during two active heating experiments. Specifications for the BRUSens DTS cable, piezometers and thermistor are presented in Appendix A.

The temperature data used for this study were acquired using the BRUSens multimode fibre optic DTS cable installed in borehole SEPI-3. Figure 2-3 shows the DTS cable with jacket removed. The blue and yellow-jacketed optical fibres (one down-going and the other up-going) were wrapped around a central strength member at a ratio of 11.8 m of fibre for every metre of cable, delivering temperature profiles with high spatial (17 cm) resolution. Temperature profiles, averaged for 10 min, were recorded every 30 minutes, by a Sensornet Halo DTS instrument (Appendix A). Further averaging of the 48 measurements recorded each day yielded temperature profiles with noise levels on the order of 0.05 - 0.1 °C, as defined by scattering of the daily mean. An example of a temperature versus depth profile displayed on the screen of the Halo DTS system is shown in Figure 2-4. It was expected that any zones of elevated seepage would be revealed by more extreme fluctuations in temperature over the course of a year as a consequence of greater heat exchange between the interior of the dam and water originating from the Mactaquac headpond.

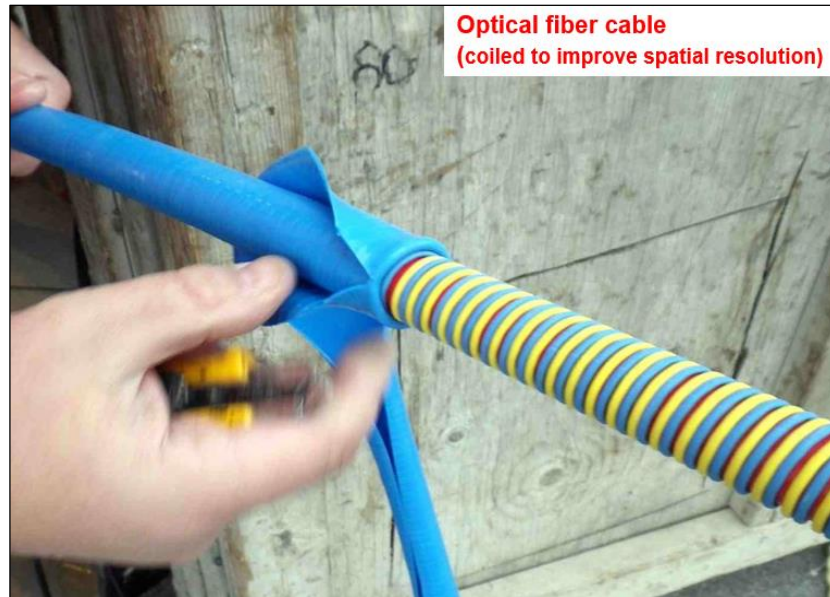


Figure 2-3: BRUSens FO cable with jacket removed, blue and yellow jacketed optical fibres (one down-going and the other up-going) wrapped around central strength member at a ratio of 11.8 m of fibre for every meter of cable.

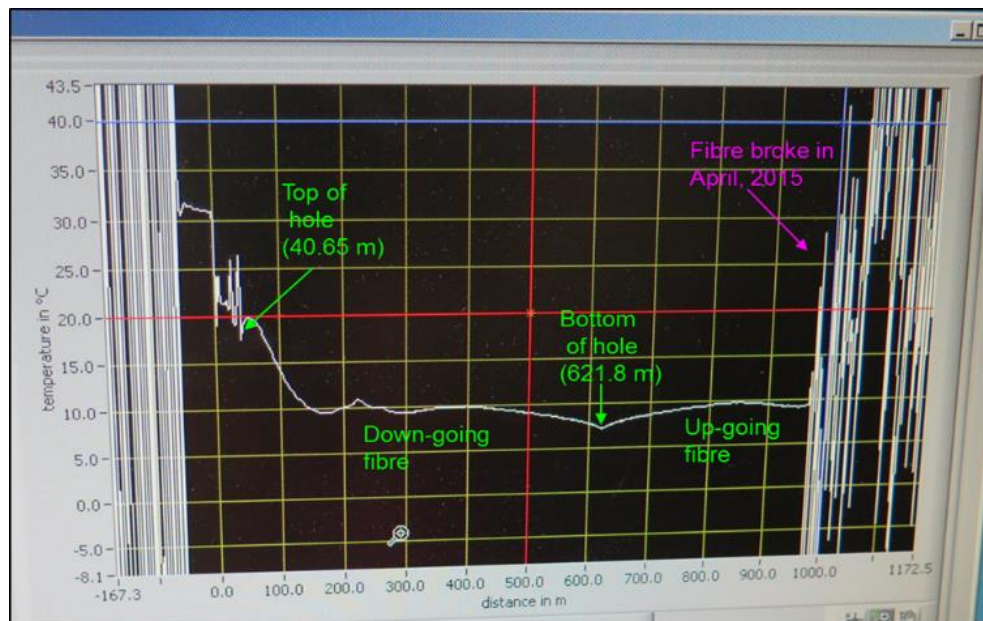


Figure 2-4: A screen capture of the Halo DTS system software showing an example of how temperature varied with distance along the optical fibre on Sep. 25, 2015. The up-going optic fibre cable broke in April, 2015.

The DTS monitoring system was connected over a wireless network to a server located in the AAR project offices at the Mactaquac Generating Station. This allowed DTS data files to be transferred to the server and then in turn be backed up to computers at UNB. The DTS system has been functioning since late December 2013. Following two active heating experiments during the summers of 2014 and 2015, the system was devoted to passive temperature monitoring. There were three significant interruptions in data acquisition during 2014 and 2015 due to power outages (eventually resolved by installation of a high capacity battery-powered uninterruptible power supply (UPS)), and other issues. On September 26, 2017, the Halo DTS was temporarily removed and sent back to the manufacturer for software and hardware upgrades. The system was reinstalled on December 19, 2017, but suffered from hardware (computer) problems such that it operated only sporadically during the winter of 2017-2018 and had to be sent back to the manufacturer again for repair in the spring of 2018.

Environmental data, including time series of air temperature and headpond level were routinely collected by NB Power. Daily average solar radiation data for the Mactaquac site were obtained from the NASA Prediction of Worldwide Energy Resource (POWER) website. The headpond water temperature was only recorded at one point located about 3 m below the surface, right at the face of the SEP concrete, using one temperature sensor in a galvanized steel pipe bolted to the concrete. Headpond water temperatures as a function of depth were acquired approximately 1 km upstream of the dam from July to November, 2014, as part of the ongoing Mactaquac Aquatic Ecosystem (MAES) project (Appendix B). Another three independent headpond temperature versus depth measurements were acquired on December 5, 2016, June 1,

2017 and August 30, 2017 by deploying a Solinst Model 107 TLC (temperature-level-conductivity) meter from a jib boom on the SEP concrete structure (Appendix C). These data were used to extend the summer/fall data from the MAES project to provide a representative annual temperature versus depth time series for the headpond (described further in Section 4.2.2).

## **2.2 DTS data plots and conceptual model**

### *2.2.1 Observed temperature anomalies*

Over approximately four years of monitoring, DTS profiles have been compiled to compare the evolution of average weekly and daily temperature. The weekly average DTS temperature profiles (Figure 2-5) show large swings in temperature near the surface, with the amplitude of annual temperature variations gradually decreasing with depth. Comparisons of weekly average temperature profiles show seasonal variations decreasing from more than 35 °C at the surface to less than 1 °C near the dam foundation. The daily average DTS temperature profiles (Figure 2-6) show more details in daily temperature oscillations. The abrupt temperature shifts on July 15, 2015 are due to calibration of the Halo DTS system, with the slope calibration value decreasing from 1.295 to about 1.255 to correct for differential attenuation relating to the signal loss in Stokes and anti-Stokes wave propagation.

Two anomalous temperature patterns are indicated in Figure 2-5. The most obvious one is at elevation 113' to 120-129' (slant depth 8.9 m to 6.3-3.1 m) between November and May of each year. This anomalous zone is bounded on the top and

bottom by narrow intervals of very high temperature gradients and the anomalous zone is cooler than would be expected based on the trends evident below it. Over time, the top of the anomalous zone shifted upwards from 120' in 2014, to 125' in 2016, and to 129' in 2017. Another minor temperature anomaly was observed at elevation 95'. The temperature at this depth was anomalously warm or cold between August and April. Unlike the shallower one, the temperature anomaly at elevation 95' appears during both summer and winter.

Additional plots were generated to specifically investigate the shallow temperature anomaly. According to Johansson (1997), larger seasonal temperature variations within the dam and shorter time lags between their appearance in the headpond and the dam indicate higher seepage. The relative amplitude and time lag of seasonal temperature variations at different depths within the dam may also contain information about the anomalous seepage. Thus, weekly average temperature time series for the air, headpond, and six different depths within the monitoring borehole were plotted (Figure 2-7). The shallowest temperature time series at elevation 134' follows the air temperature closely. The three temperature time series at the depths within the shallow anomalous zone clearly lag temperature variations in the headpond. However, the three anomalous zone temperature time series converge during fall/winter 2015/2016 and 2016/2017 and do not exhibit time lag with increasing depth. This anomalous temperature pattern indicates that, besides the process of heat conduction, heat transfer through convection may also be occurring in this zone.

Figure 2-8 shows how the headpond water level and the upper and lower boundaries of the shallow temperature anomaly changed over time between 2014 and

2017. The base of the anomalous zone remained nearly constant at an elevation of 113' from winter 2014 to winter 2017, but its height increased incrementally from one year to the next. The headpond level remained at approximately 132' during the same time period, with only minor and relatively short period fluctuations, thereby illustrating that the height of the anomalous zone had no obvious correlation with headpond level.

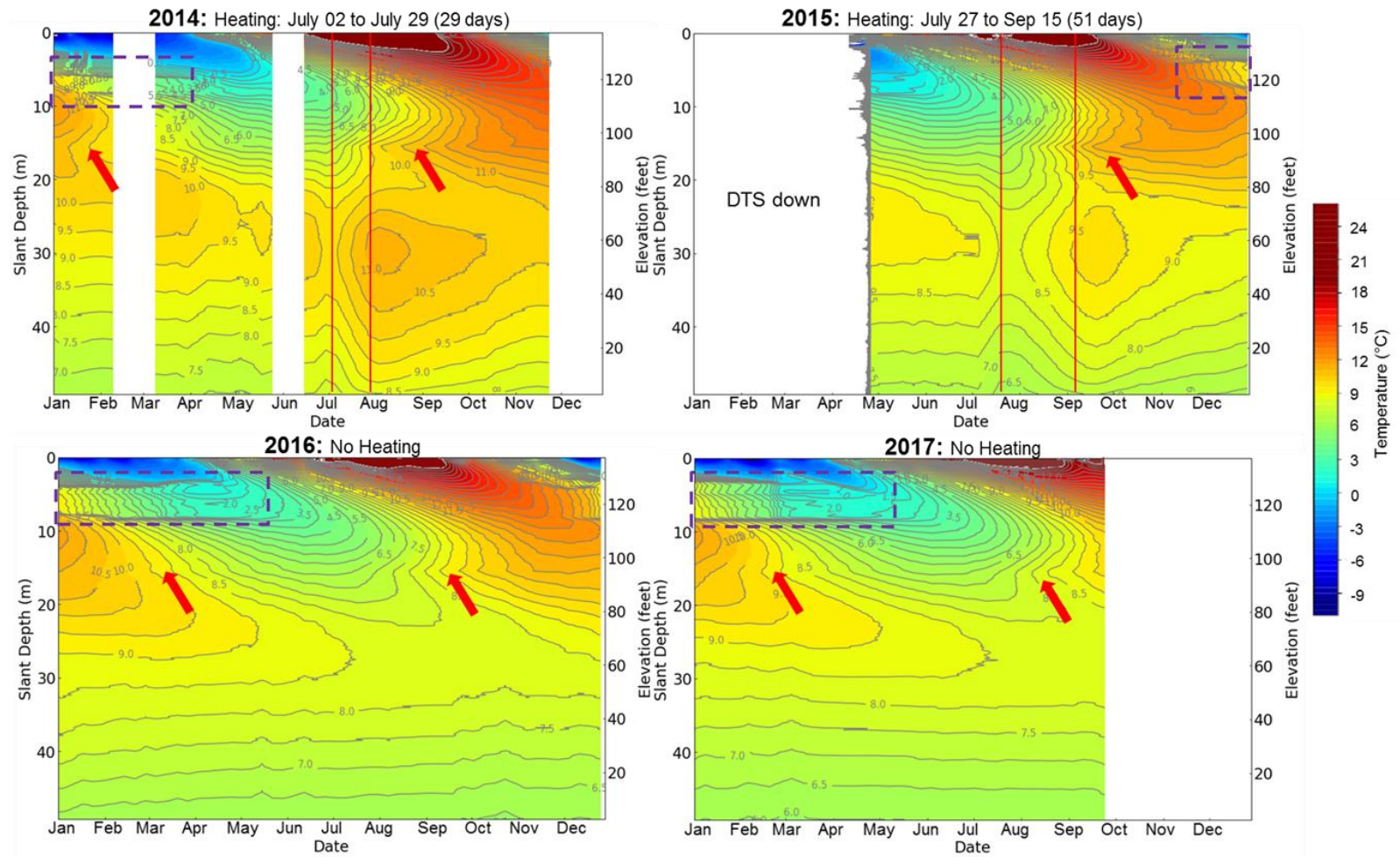


Figure 2-5: Plots of seasonal variations in weekly average temperature versus depth in borehole SEPI-3 for years 2014 to 2017. The red lines in the 2014 and 2015 plots indicate the duration of the heating experiments during those two years. The red arrows and purple dashed rectangles indicate the location of anomalous temperature zones.

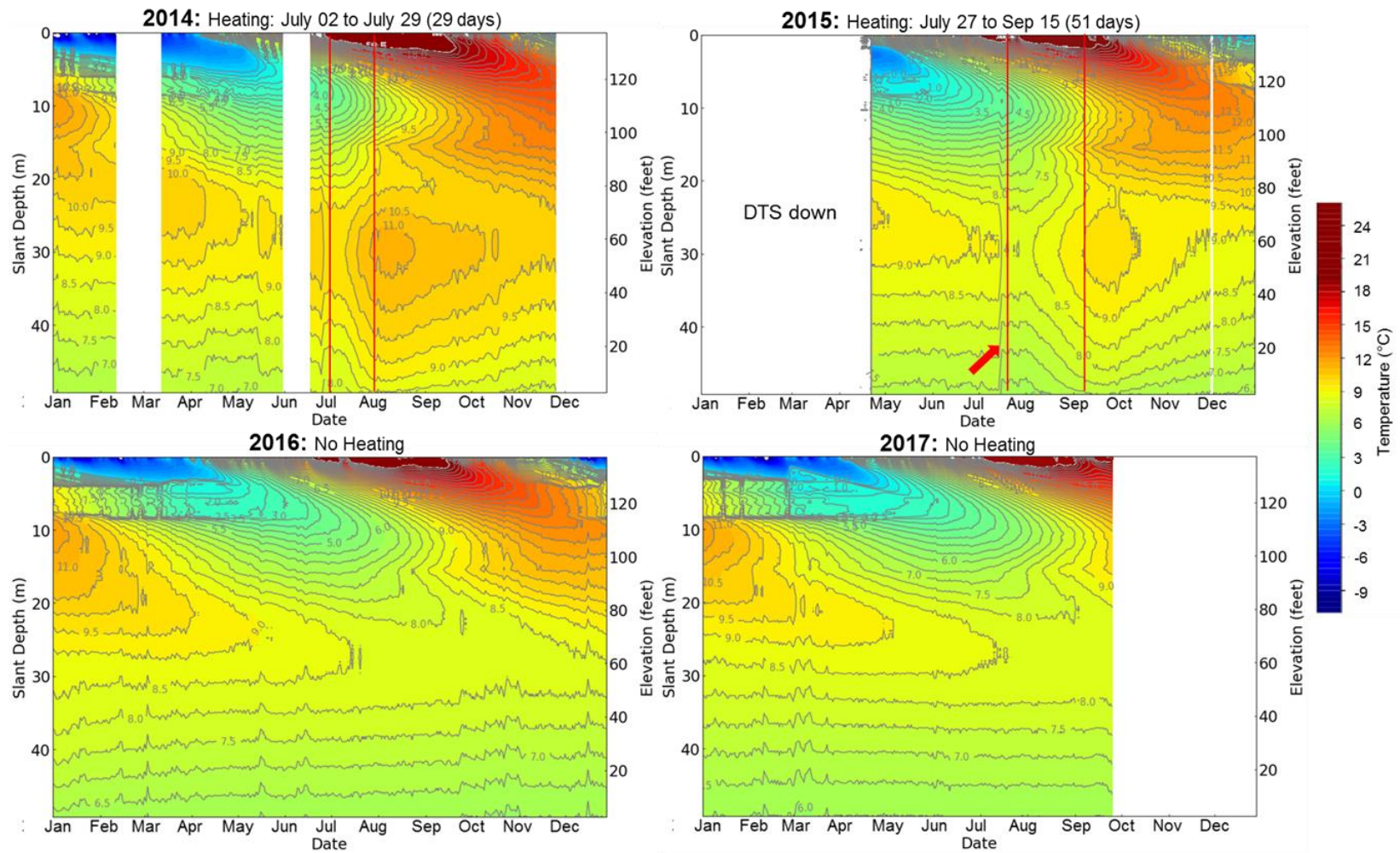


Figure 2-6: Plots of seasonal variations in daily average temperature versus depth in borehole SEPI-3 for years 2014 to 2017. The red arrow in the 2015 plot indicates the abrupt temperature shift observed on July 15, 2015.

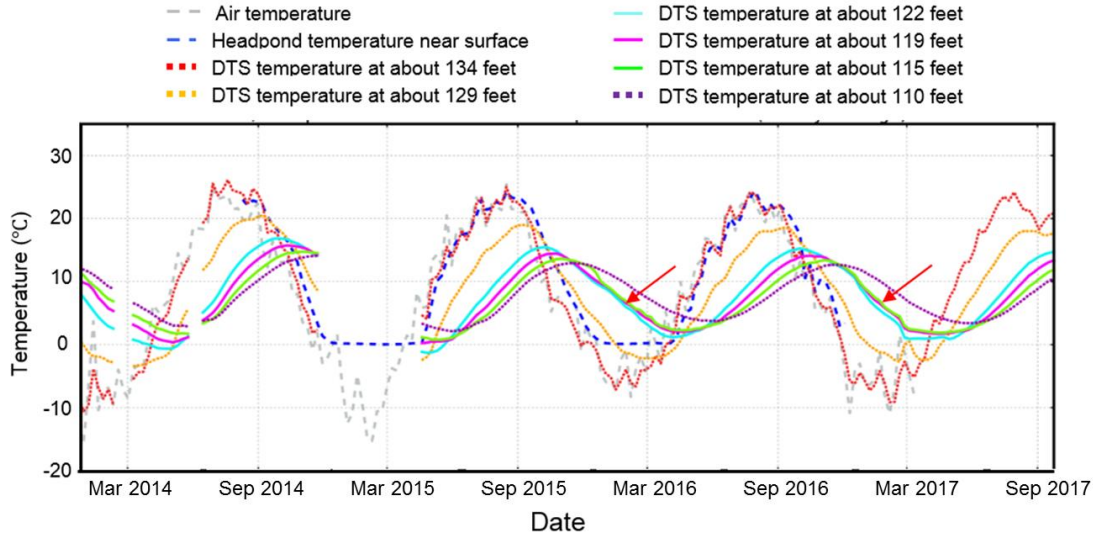


Figure 2-7: Air, headpond and potential shallow seepage zone temperature time series from Jan. 2014 to Sep. 2017 (weekly average). Temperature anomalies are indicated by red arrows.

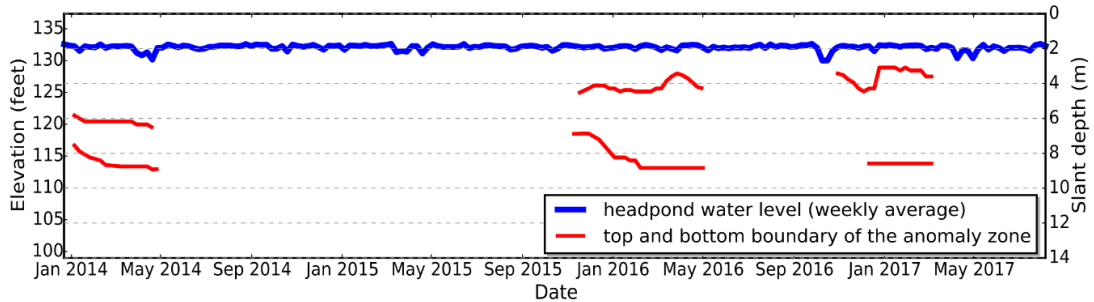


Figure 2-8: Weekly average headpond water level and elevations of the upper and lower boundaries of the shallow temperature anomaly from January, 2014 to July, 2017.

### 2.2.2 Visual evidence of possible seepage

Visual inspections at the Mactaquac Generating Station in recent years also show some evidence of potential seepage near the dam/concrete interface. For example, vegetation on the downstream slope of the embankment in the vicinity of the interface

was observed in November 2014 (Figure 2-9). This may indicate potentially increased seepage near the upper section of the dam. In April 2017, ice was observed emanating from a concrete crack on the back of the SEP concrete wall (Figure 2-10). This indicates seepage through the concrete structure, though not necessarily along the dam/concrete interface. Interestingly, the top of the ice fall shown on the photo is very close to elevation 95', which is the location of the deeper temperature anomaly observed in the DTS profiles.



Figure 2-9: Photo taken in November, 2014 showing the vegetation (indicated by red circle in the photo) observed near the dam-concrete interface on the downstream slope of the embankment. The regularly-spaced beige objects on the downstream slope of the embankment are tarpaulins covering the electrodes used for Self-Potential measurements (Ringeri & Butler, 2016).



Figure 2-10: Photo taken in April 2017, showing the residual ice observed emanating from a concrete crack on the back of the SEP concrete wall at elevation about 95'.

### 2.2.3 A conceptual model for possible seepage

Figure 2-11 shows a conceptual model illustrating the locations of potential seepage zones on a longitudinal section through the clay till core/concrete interface. Both potential seepage zones are located below the headpond water level. The first potential seepage zone is related to the shallower temperature anomaly observed in the weekly average temperature versus depth profiles during fall/winter. Cold water from the headpond carried by increased seepage flow along the interface at this location may influence the temperature measurements made in the borehole drilled into the concrete through the thermal conduction process. The minor temperature anomaly at elevation 95' may reveal another smaller potential seepage zone near the interface. The potential seepage zones may also be more directly related to cracks or more permeable zones in the concrete at the noted elevations.

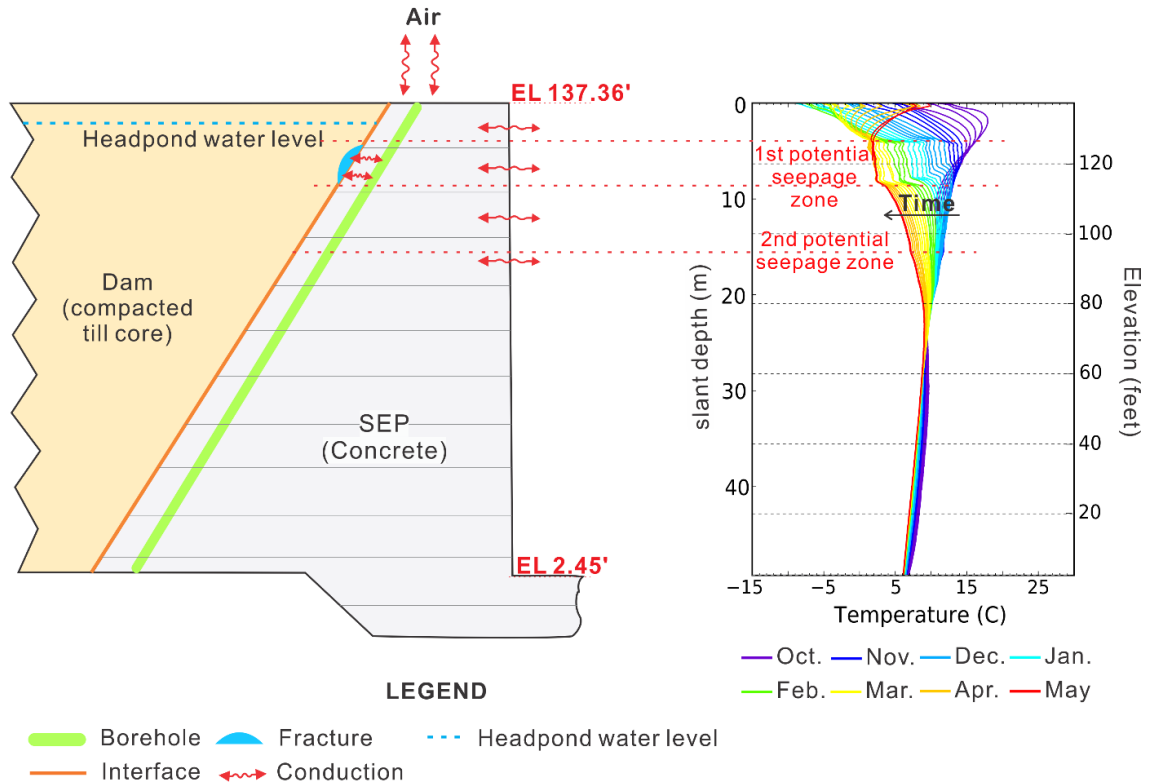


Figure 2-11: Left: Conceptual model illustrating the locations of potential increased seepage on a longitudinal section through the clay till core/concrete interface. Right: Weekly average temperature-depth profiles for October, 2015 to May, 2016.

#### 2.2.4 A conjecture about the origin of seepage

Figure 2-12 shows the thermally-induced seasonal movements of the SEP concrete structure in the longitudinal direction during 2004, which were measured by an inverted pendulum located within the SEP concrete structure (Sooch, 2016). A maximum displacement of 10.5 mm was measured at the top of the concrete from winter to summer due to large seasonal temperature variations near the surface. The top of the SEP moves away from the embankment dam in winter, while in summer it moves towards the embankment.

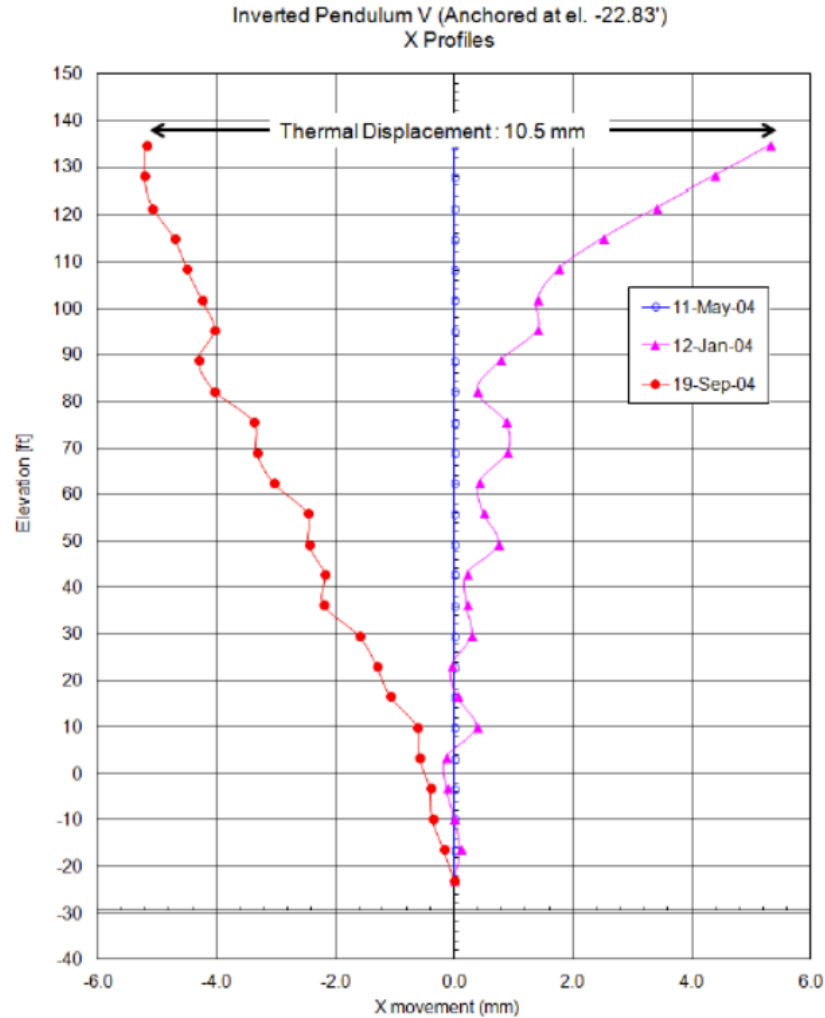


Figure 2-12: Measurements from the inverted pendulum at Mactaquac SEP located near upstream face showing the seasonal thermal displacement of the SEP concrete in the longitudinal direction during 2004 (Sooch, 2016).

The measurements from the inverted pendulum between 2004 and 2014 reveal that the concrete expansion induced by AAR has become more pronounced with time (B. Mclean, pers. comm., 2015). The rates of concrete expansion at Mactaquac are in the range of 2 to 3 times larger than any other typical dam or power station affected by AAR (Curtis et al., 2016). Figure 2-13 shows exaggerated deformed shapes of the longitudinal section of the SEP concrete to illustrate how the concrete deformation induced by AAR

may potentially affect seepage at the clay till core/concrete interface. According to B. Mclean (pers. comm., 2015), a maximum of about 13 mm differential displacement since 2004, mainly induced by AAR expansion, was measured at elevation 75' in September, 2014. A relatively small differential displacement of about 8.5 mm was measured at the top of the concrete and a minimum differential displacement of about 2.0 mm was measured at the bottom at the same time. This significant deformation of the concrete structure may cause a gap to form between the clay till core and the SEP concrete near the upper section of the dam, especially during winter when the concrete moves away from the embankment due to contraction; the ability of the embankment to move back with the SEP near the face may be decreasing with time, which would be consistent with observed growth in the height of the shallow temperature anomaly in recent years.

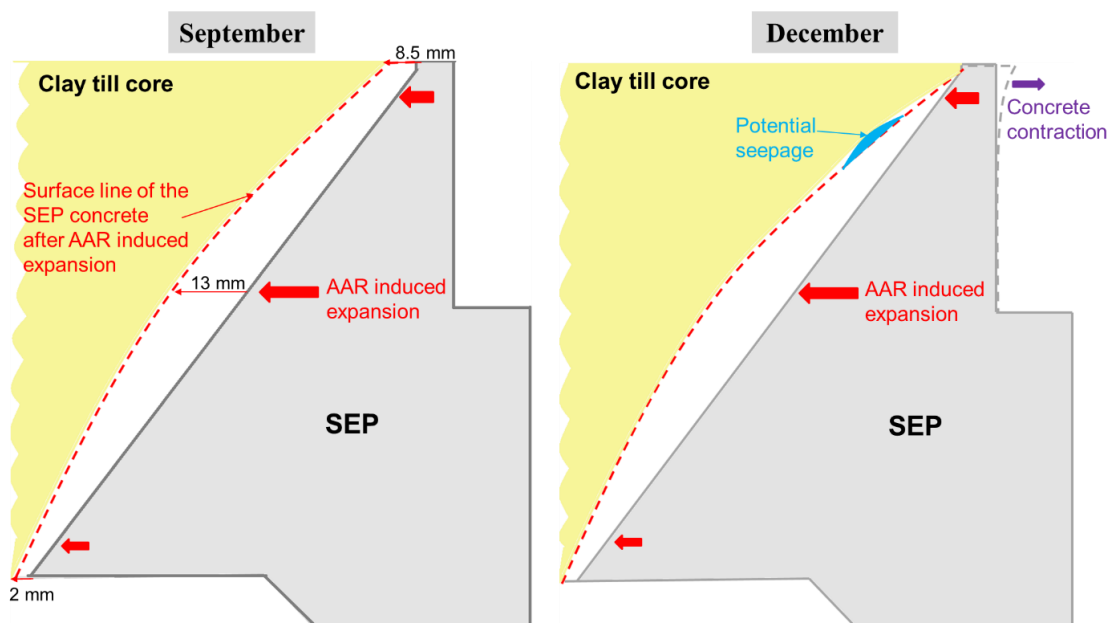


Figure 2-13: Exaggerated deformed shapes of the longitudinal section of the SEP concrete, illustrating how AAR induced concrete expansion may cause a potential seepage zone at the clay till core/concrete interface.

### **2.3 DTS data processing and calibration**

DTS systems are more effective for measuring temperature variations than absolute temperatures. The accuracy of standard calibration procedures provided with DTS systems is normally adequate for seepage detection applications (Hausner et al., 2011). However, transient or permanent damage to the fibres, connections between different fibres, and fusion splicing can all affect the attenuation of Stokes and anti-Stokes backscatter, which cannot always be calibrated within the instrument's standard calibration procedure (Hausner et al., 2011) and may cause significant errors in the absolute values of the measured temperature. Although seepage detection focuses more on temperature variations, the accuracy of the measured absolute temperature is very important for comparisons to the numerical simulations in this study, especially given that the foundation temperature was taken as the DTS temperature at the bottom of the borehole. Thus, DTS data processing and calibration are necessary before they can be applied to numerical simulations.

Regarding the fibre optic cable installed for this study, one connector and two splices were present between the Halo DTS control unit and the top of the SEPI-3 borehole, which may cause potential signal loss and trigger errors in the measured DTS temperature.

To improve the accuracy of DTS data, the temperature logged by two thermistors embedded in two vibrating wire piezometers (one at a slant depth of 33.4 m in SEPI-3, with the second at a slant depth of 21.4 m in SEPI-2) and one resistance temperature detector (RTD) (at slant depth of 7.6 m in SEPI-2) were compared with the DTS temperature at corresponding depths in SEPI-3. Thermistor temperature was logged

every 30 minutes while RTD temperature was manually recorded during site visits on seven dates. Daily average DTS temperature and thermistor temperature comparisons, as well as hourly average DTS temperature and RTD temperature comparison, are presented in Figure 2-14. The two temperature peaks shown in the thermistor temperature during the summer of 2014 and 2015 are due to the heating experiments performed in borehole SEPI-2. As the SEPI-2 thermistor and RTD are in a different borehole than the DTS cable, which is about 3 m away, comparison of temperature differences between them and the DTS was not made during the heating period. All the results indicate that the DTS measured lower temperatures than the thermistors and the RTD sensor at corresponding depths. Thus, an additional calibration procedure was required to process the instrument-calibrated DTS temperature data before applying them to numerical simulations.

Temperature comparisons between the DTS and the SEPI-3 thermistor data are considered most reliable as they were installed in the same borehole. An abrupt temperature drop was observed on July 15, 2015 in the DTS temperature data which did not appear in the thermistor temperature. This was caused by a change in the slope calibration value specified in the Halo DTS configuration file to adjust the value assumed for differential attenuation of Stokes and anti-Stokes backscatter. After that date, a nearly constant temperature difference of 2.5 °C was noted. The period of interest for modelling lies between June 2016 and June 2017 because the influence of the two prior heating experiments would have been very small. Thus the analysis was focussed on adjusting the DTS calibration for the period after July 15, 2015. However, the use of 2.5 °C as an offset value was questionable for the following reasons: 1) there was only

one thermistor in the borehole with the DTS cable, and the accuracy and reliability of that thermistor was difficult to estimate; 2) the comparison between temperature measured by SEPI-2 thermistor and DTS system at about 21.3 m shows temperature differences lower than 2.5 °C for most of the time and can be as low as 1.75 °C; 3) the temperature offset measured between the SEPI-3 thermistor and the DTS system in 2014 was only about 1 °C; however, the offset increased to 2 °C in mid-2015 right after a break was first observed in the up-going optical fibre. In November 2015, a further break in that cable (deeper in the borehole) coincided with another increase in the temperature offset by 0.25 °C. Thus, for reasons that are not understood, it seems that both optical fibre breaks tended to decrease the absolute DTS temperature; 4) several experimental numerical simulations were performed, and the results indicated that an offset correction yielding a temperature increase of 2.5 °C at 33.4 m depth tended to cause an unreasonable temperature gradient between the headpond temperature and the foundation temperature, which is taken as the DTS temperature at the bottom of the borehole. Thus, considering that the accuracy of the thermistor is +/- 1 °C (i.e. 0.5% of its 200 °C measurement range), a 1.0 °C temperature offset at 33.4 m was finally adopted as a basis for further calibration procedures.

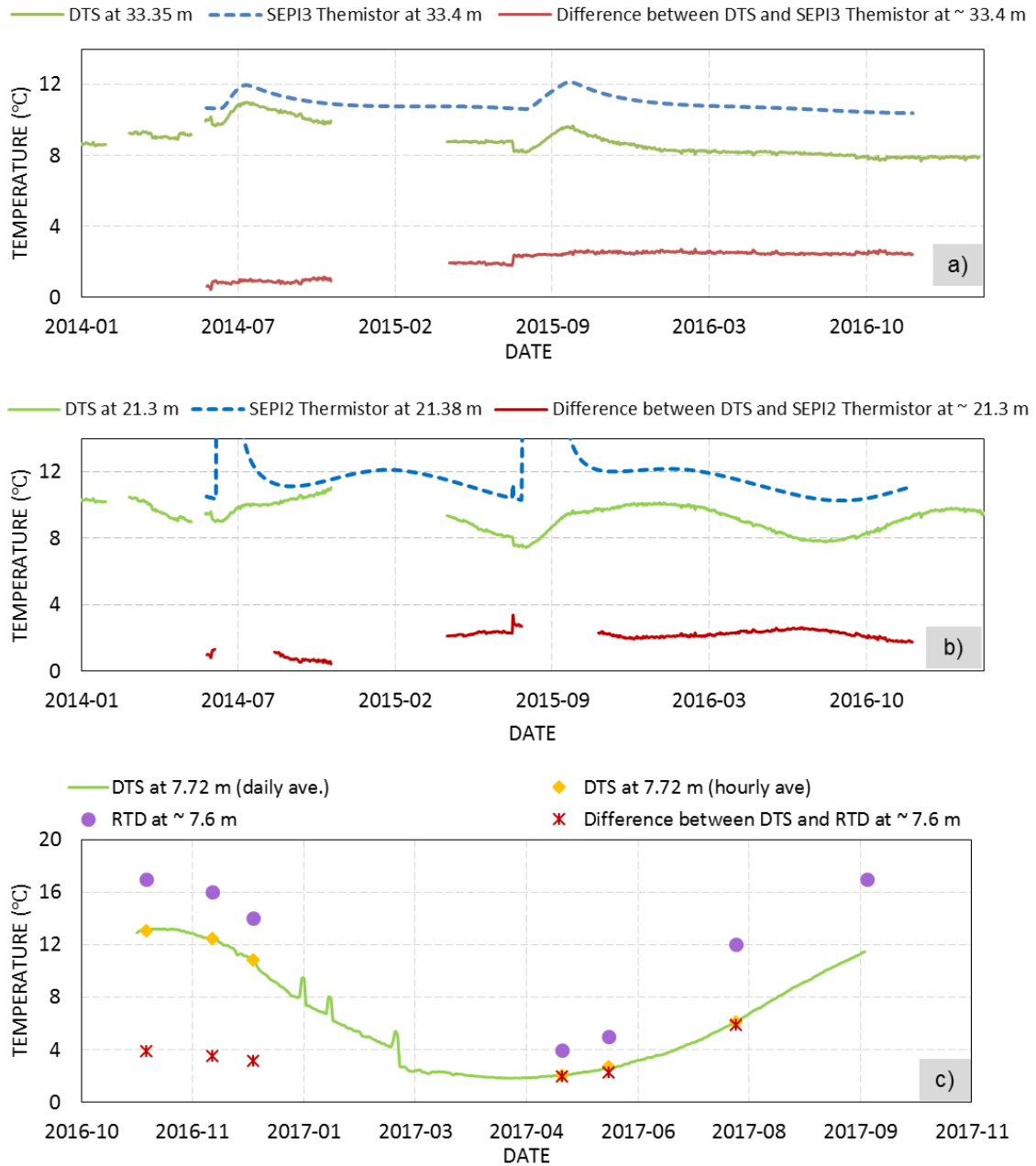


Figure 2-14: Comparisons of DTS measured temperature with thermistor and RTD temperature at different depths: a) Comparison of daily average DTS temperature and SEPI-3 thermistor temperature at depth about 33.4 m; b) Comparison of daily average DTS temperature and SEPI-2 thermistor temperature at depth about 21.3 m; c) Comparison of daily and hourly average DTS temperature and SEPI-2 RTD temperature at depth about 7.6 m.

### 2.3.1 Adjustment of DTS calibration parameters

The basic equation for determining temperature along an optical fibre from the power ratio of the Stokes and anti-Stokes backscattering is (Van De Giesen et al., 2012):

$$T(y, t) = \frac{\gamma}{\ln\left(\frac{P_s(y,t)}{P_{as}(y,t)}\right) + A(t) - \int_0^y \Delta\alpha(y') dy'} \quad (2.1)$$

where  $T$  is the temperature (K),  $t$  is time (T), and  $y$  is the distance along the cable with  $y = 0$  at the DTS instrument.  $P_s(y, t)/P_{as}(y, t)$  is the measured power ratio of the Stokes and anti-Stokes backscattering, and  $\gamma$  (K) is the shift in energy between a photon at the wavelength of the incident laser and the scattered Raman photon. The integral in the denominator represents the cumulative differential attenuation between the Stokes and anti-Stokes radiation caused by the differences in the absorption coefficients for their different frequencies.  $A(t)$  is a dimensionless calibration parameter that accounts for the properties of the incident laser and the sensitivities of the detectors. It is dependent on the instrument temperature. In the case of the Halo DTS system, which uses a laser of wavelength 1064 nm,  $\gamma$  is equal to 501.0146 K. Also, by default the differential attenuation factor  $\Delta\alpha(y)$  is assumed to have a constant value of 0.3772 dB/km.

To remove the influences of the differential attenuation associated with cable imperfections, such as the two splices between the instrument and the top of the sensing cable, and to allow for an intrinsic cable attenuation factor different than 0.3772 dB/km, an offset calibration value  $\beta$  and a slope calibration value  $\omega$  can be applied to the terms  $\ln\left(\frac{P_s(y,t)}{P_{as}(y,t)}\right)$  and  $\int_0^y \Delta\alpha(y') dy'$ , respectively. In that case, Eq. 2.1 can be rewritten as follows:

$$T(y, t) = \frac{\gamma}{\ln\left(\beta \frac{P_s(y,t)}{P_{as}(y,t)}\right) + A(t) - \int_0^y \omega \Delta\alpha(y') dy'} \quad (2.2)$$

In the Halo DTS system setup,  $\omega$  had been set to 1.2555 since July 15, 2015, while  $\beta$  was set to its default value of 1.0 for the entire measurement time, which means no offset correction has been performed in the instrument calibration procedures. The post-acquisition calibration adjustment described here involved estimating new values for  $\beta$  and  $\omega$  to better compensate for differential attenuation so as to reduce the discrepancy between DTS temperatures and the two reference thermistor temperatures as described above.

Values of  $A(t)$  at each measured point and time were firstly calculated based on Eq. 2.1, as the Halo DTS data files provide measurements of  $P_s(y, t)$  and  $P_{as}(y, t)$ . After that, the user-calibrated temperature was calculated by varying  $\beta$  and  $\omega$  to remove the artificial signal loss as described below. Figure 2-15 (a) illustrates graphically the analysis used to determine improved slope and offset calibration values. Temperature and intensity of the Stokes and anti-Stokes backscattering measured at midnight on Aug. 1, 2015 were used as a sample data set. Although part of the up-going optical fibre was broken, there still was a significant remaining length that could be used for comparison with the temperature measured by the down-going optical fibre. A proper slope calibrated value can be determined when the calculated temperature versus distance profile is symmetric for the down-going and up-going part. The slope calibration value  $\omega$  determined in this manner was 1.27. Then, using this slope calibration value, the offset value  $\beta$  was adjusted until the user-calibrated temperature was 1.0 °C higher than the instrument-calibrated data at depth of 33.4 m, which is about 434.1 m in the length

of fibre optic cable. The value determined for  $\beta$  in this way was 0.99424. To verify whether the determined calibrated values can be applied to the full data, differences between user-calibrated and instrument-calibrated temperature data at depth 33.4 m were plotted from June 2016 to June 2017 in Figure 2-15 (b). The results show a nearly constant 1.0 °C temperature difference at depth 33.4 m which proved the feasibility of this calibration method.

The weekly average user-calibrated temperature profile from June 2016 to June 2017 is shown in Figure 2-16. The calibration applied to the measured DTS temperature did not generate any obvious changes in the temperature variations, but did increase the absolute temperature along the borehole.

It is recommended for future applications of DTS technology in seepage monitoring, especially for DTS cables being installed in boreholes within dams, that precise ( $\pm 0.1$  °C) temperature sensors be installed in at least two locations along the cable to improve calibration of the DTS. One point temperature sensor should be installed at the end of the measured distance (e.g. at the bottom of the borehole in this study) to determine the DTS offset error. The other thermistor can be installed near the end of the measured distance (e.g. 1 m above the bottom of the borehole) for the purpose of double calibration. In this way, offset errors in the measured DTS temperature caused by artificial signal loss can be calibrated by comparing the temperature measured by DTS system and point sensors.

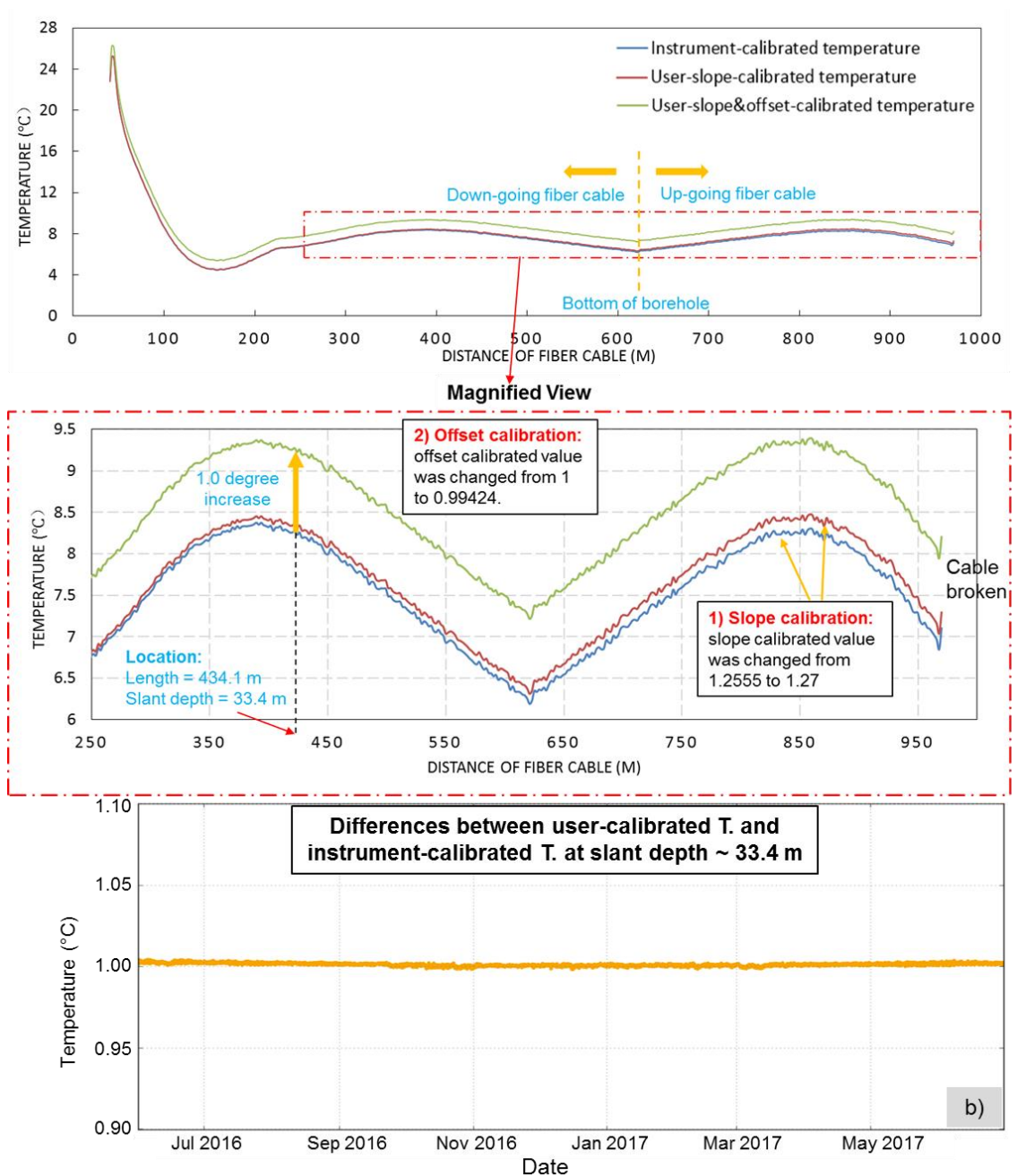


Figure 2-15: Description and verification of the calibration method applied on the instrument-calibrated data to remove the additional differential attenuation in the Stokes and anti-Stokes back scatter. a) Diagrams show the method of determining new offset and slope calibrated values. The instrument-calibrated temperature data is a sample data set measured at midnight on August 1, 2015. b) Differences between user-calibrated and instrument-calibrated temperature at depth about 33.4 m from June 2016 to June 2017 for the purpose of verifying the feasibility of the calibration method.

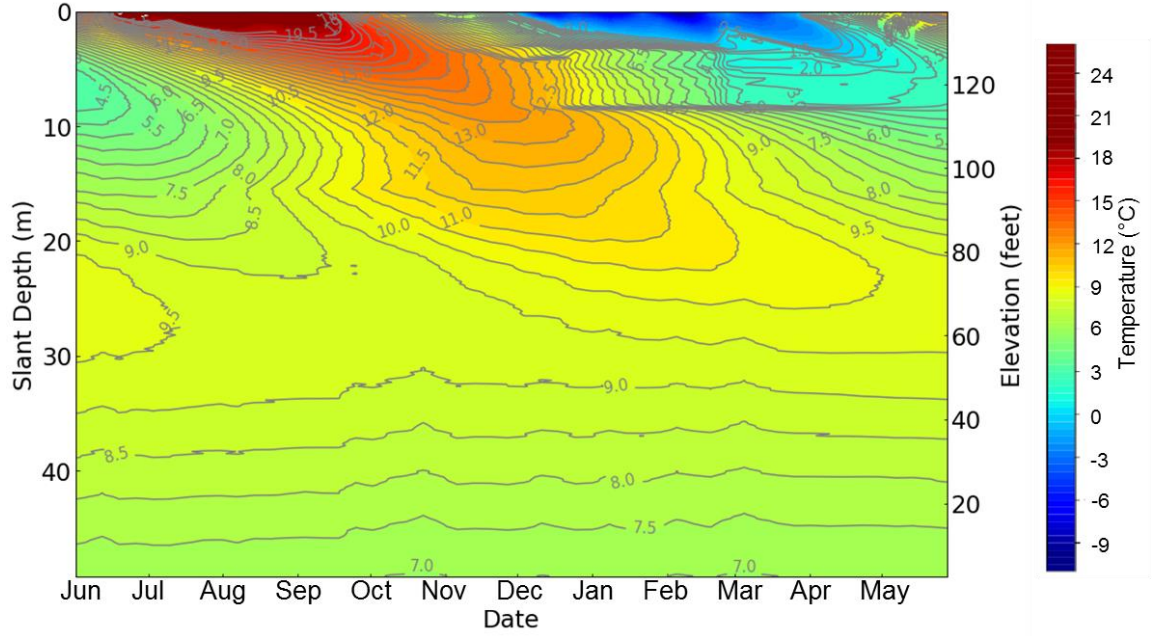


Figure 2-16: User-calibrated plot of temperature versus depth from June 2016 to June 2017 (weekly average).

## **Chapter 3 : Theoretical background**

### **3.1 Seepage and temperature fields in embankment dams**

The thermal-hydraulic processes occurring within embankment dams include heat conduction, convection and radiation (Johansson 2009). The process of heat conduction depends on having a temperature gradient between the dam surface and the dam interior, while heat convection is related to water seepage, or air circulation within unsaturated portions of the dam. Heat radiation can be divided into two categories: one being thermal radiation as a result of temperature differences between the dam surface and the air, the other being solar radiation from the sun (Venturelli, 1992). Typically, heat loss from a dam by thermal radiation is not expected to be significant, and thus can be ignored for most cases (Venturelli, 1992). Heat absorbed from solar radiation; however, may cause the dam surface temperature to exceed that of the surrounding air. The temperature increase is more significant for a concrete structure than it is for an embankment due to the higher absorption of solar radiation by concrete (Bofang, 2013). Thus, solar radiation should be taken into account when estimating the surface temperature of concrete. For an embankment dam, the influence of solar radiation is usually neglected, and the air-embankment interface is assumed to have the same temperature as the surrounding air.

The temperature of an embankment dam is mainly affected by the surrounding air and headpond water temperatures. Seasonal variations in air and water temperatures generate temperature fronts that propagate through the dam (Johansson, 1997). The influence of the geothermal heat flux through the foundation is also considered in this study, as for a moderate size dam, the temperature distribution at greater depths within

the dam may be influenced by both headpond temperature and geothermal heat fluxes (Johansson, 1997).

Normally the seepage flow within an embankment dam is small, such that heat transport is dominated by conduction due to temperature gradients between the dam interior and the surrounding air, headpond and foundation. For depths within the dam body that exceed about 10 m, especially for saturated materials, the influence from variations in the air temperature is less than 1°C and is therefore negligible (Johansson, 1997). At such depths the temperature within the dam depends largely on the headpond water temperature. When anomalously high seepage occurs, the flow of water from the headpond through the dam gives rise to heat transport by convection. Thus the normal conductive temperature field within the embankment dam will be disturbed.

### **3.2 Hydro-thermal coupling**

Seepage flow within embankment dams is driven by hydraulic head gradients that depend on both pressure gradients and on gravitational forces that can be influenced by temperature-dependent water density. Seepage also depends on the hydraulic conductivity of the dam materials, which in turn depends on the intrinsic permeability of the porous media and on the viscosity of water, which can vary with temperature and salinity. The specific discharge (i.e. volumetric discharge per unit area) of the seepage flow is usually described by a general form of Darcy's law (Fetter, 2000):

$$q = - K \frac{\Delta h}{\Delta L} \quad (3.1)$$

where

$q$  = specific discharge, also referred to as the Darcy velocity or Darcy flux [ $LT^{-1}$ ]

$K$  = hydraulic conductivity [ $LT^{-1}$ ]

$h$  = hydraulic head [L]

$L$  = distance along the direction of flow [L].

The constitutive relationships are (Fetter, 2000):

$$h = z + \frac{P}{\rho g} = z + \psi \quad (3.2)$$

$$K = \frac{\rho g}{\mu} \kappa \quad (3.3)$$

where

$z$  = elevation head [L]

$\psi$  = pressure head [L]

$P$  = fluid pressure [ $ML^{-1}T^{-2}$ ]

$\rho$  = fluid density [ $ML^{-3}$ ]

$\mu$  = dynamic viscosity [ $ML^{-1}T^{-1}$ ]

$\kappa$  = intrinsic permeability [ $L^2$ ]

$g$  = gravitational acceleration [ $LT^{-2}$ ].

When seepage occurs through an embankment dam, heat is exchanged between the flowing water and the surrounding porous medium. Conversely, variations in temperature affect the dynamic viscosity and density of water, thus changing the seepage velocity (Cuong et al., 2017b). As the viscosity and the density of water are temperature

dependent, heat conduction and convection are partly coupled to each other (Johansson, 2009). The problem is further complicated by heterogeneous and anisotropic material properties within the dam and spatially variable degrees of saturation.

Several assumptions are commonly applied when simulating the hydro-thermal coupling in variable-saturated embankment dam materials. Cuong et al. (2017a) have recently summarized in a review paper that in range of temperature and seepage variation inside an embankment dam, the assumptions presented below do not result in significant differences in the final computed results:

1) water is an incompressible fluid; 2) water flow in porous media is laminar; 3) locally, there is no temperature difference between solids and water; 4) heat transport related to air and water vapor, such as air flow conduction and convection, water evaporation and water vapor condensation, are neglected; and 5) soil deformation is ignored (Cuong et al., 2017a).

The effects of freezing and thawing cycles on the heat transport within the dam were also neglected in this study. The maximum frost depth estimated at the Mactaquac dam is 1.3 m (Appendix D). Since the maximum frost depth is above the maximum headpond water level of elevation 132.9' (1.6 m from the top of the dam), no significant influence from the freezing and thawing of water on the heat transport is expected.

With these assumptions, the governing three-dimensional heat transport equation for variably-saturated porous media can be written as follows (Cuong et al., 2017a; Diersch, 2009b; Shija & MacQuarrie, 2015):

$$\begin{aligned}
& [s(\psi)\varepsilon C_w + (1-\varepsilon)C_s] \frac{\partial T}{\partial t} \\
& = \nabla \cdot C_w \mathbf{D} \nabla T - C_w \mathbf{q} \cdot \nabla T + \nabla \cdot [\varepsilon s(\psi) \lambda_w \mathbf{I} + (1-\varepsilon) \lambda_s \mathbf{I}] \cdot \nabla T
\end{aligned}
\tag{3.4}$$

where

$s(\psi)$  = degree of saturation, described as a function of pressure head [-]

$\varepsilon$  = porosity [-]

$C_w$  = volumetric heat capacity of water [ML<sup>-1</sup>K<sup>-1</sup>T<sup>-2</sup>]

$C_s$  = volumetric heat capacity of solids [ML<sup>-1</sup>K<sup>-1</sup>T<sup>-2</sup>]

$T$  = temperature [K]

$t$  = time [T]

$\mathbf{q}$  = Darcy flux vector [LT<sup>-1</sup>]

$\mathbf{D}$  = tensor of mechanical dispersion [L<sup>2</sup>T<sup>-1</sup>]

$\mathbf{I}$  = unit tensor [1]

$\lambda_w$  = thermal conductivity of water [MLK<sup>-1</sup>T<sup>-3</sup>]

$\lambda_s$  = thermal conductivity of solids [MLK<sup>-1</sup>T<sup>-3</sup>]

$$\nabla = \frac{\partial}{\partial x} + \frac{\partial}{\partial y} + \frac{\partial}{\partial z}.$$

The tensor of mechanical dispersion is given by (Diersch, 2009b):

$$\mathbf{D} = (\alpha_L - \alpha_T) \frac{\mathbf{q} \otimes \mathbf{q}}{\|\mathbf{q}\|} + \alpha_T \|\mathbf{q}\| \mathbf{I} \tag{3.5}$$

where

$\alpha_L$  = longitudinal dispersivity [L]

$\alpha_T$  = transverse dispersivity [L].

$\otimes$  denotes Kronecker product of two matrices.

Water transport in variably-saturated porous media according to Darcy's law can be denoted as (Cuong et al., 2017a; Diersch, 2009b):

$$\mathbf{q} = - K_r(s) K \frac{\mu_0}{\mu} (\nabla h + \frac{\rho - \rho_0}{\rho_0} \mathbf{e}) \quad (3.6)$$

where

$K_r$  = relative hydraulic conductivity,  $0 < K_r \leq 1$ ,  $K_r = 1$  when  $s = 1$  [-]

$\mu_0$  = reference dynamic viscosity [ $ML^{-1}T^{-1}$ ]

$\rho_0$  = reference fluid density [ $ML^{-3}$ ].

$\mathbf{e}$  = gravitational unit vector [1]

The term on the left-hand side of Eq. 3.4 represents the ability of the solid-water system to store heat. The first term on the right-hand side of Eq. 3.4 accounts for heat transfer by dispersion due to the variability in seepage flow velocities. The second term on the right-hand side describes heat transport by convection, while the third term represents heat conduction in the solids and water.

One common model to solve for the transient distribution of hydraulic head, and subsequently the Darcy flux in Eq. 3.6, is Richards' nonlinear partial differential equation, which is commonly used to describe seepage in unsaturated porous media (Richards, 1931). The strong dependencies of relative (unsaturated) hydraulic

conductivity and pressure head on saturation make Richards' equation highly non-linear and difficult to solve. Several models based on experimental data have been proposed to determine the relative hydraulic conductivity and retention curve. A modified van Genuchten model (Diersch, 2016), which relates saturation, water pressure and hydraulic conductivity, is adopted in this research:

$$s_e = \begin{cases} 1/[1 + (\alpha|\psi|^n)]^m & \text{for } \psi < 0 \\ 1 & \text{for } \psi \geq 0 \end{cases} \quad (3.7)$$

$$K_r = s_e^\delta \quad (3.8)$$

$$m = 1 - \frac{1}{n} \quad (3.9)$$

with the effective saturation of fluid given by:

$$s_e = \frac{s - s_r}{s_s - s_r} \quad (3.10)$$

where:

$\alpha$  = van-Genuchten curve fitting parameter [ $L^{-1}$ ]

$m, n, \delta$  = van-Genuchten curve fitting parameters [-]

$l$  = pore-connectivity parameter, about 0.5 is optimum for many soils [-]

$s_e$  = effective saturation [-]

$s_r$  = residual saturation [-]

$s_s$  = maximum saturation that is equivalent to 1 [-].

To solve for temperature and Darcy velocity from nonlinear Eq. 3.4 and Eq. 3.6, a set of thermal-hydraulic parameters including hydraulic conductivity, effective porosity, thermal conductivity, volumetric heat capacity and dispersivity need to be determined. These parameters can be specified by either experiment methods or analytical models. A summary of different methods to determine these parameters for an embankment dam is presented in Cuong et al. (2017a).

### **3.3 Numerical model selection**

The numerical modelling code FEFLOW 7.0 (Diersch, 2013) developed by group WASY GmbH, was selected for this study mainly due to its ability to simulate three-dimensional, coupled steady state or transient seepage with transient heat transport in variably-saturated porous media. Other characteristics of FEFLOW that made it appropriate for this study included: 1. It allows for automatic time step control so that stable temporal discretization can be achieved easily; 2. It can solve problems involving complex boundary conditions with four types of boundary conditions for unsaturated flow and heat transport; 3. The complex three-dimensional geometries of the dam-concrete structure can be solved robustly and efficiently due to flexible mesh generation schemes and element deactivation capabilities; 4. Time-varying material parameters can be easily implemented making the simulation of seasonally varying seepage conditions possible; 5. Several previous studies have used FEFLOW to successfully solve coupled heat transport-seepage problems through dams (Velásquez, 2007; Shija & MacQuarrie, 2015; Cuong et al., 2016; Opaliński et al., 2016).

The governing equations for heat transport and water flow that are solved in FEFLOW have been discussed in Section 3.2. FEFLOW also uses a set of constitutive relations to couple seepage flow and heat transport processes. The temperature-dependent fluid viscosity is determined as follows (Diersch, 2013):

$$\mu(T_c) = \frac{\mu_0}{1 + 0.7063\xi - 0.04832\xi^3} \quad (3.11)$$

$$\text{with } \xi = \frac{T_c - 150}{100}$$

where

$T_c$  = temperature in degrees Celsius [ $^{\circ}\text{C}$ ]

$\mu$  = dynamic viscosity [ $\text{ML}^{-1}\text{T}^{-1}$ ]

$\mu_0$  = reference viscosity relating to zero concentration and temperature [ $\text{ML}^{-1}\text{T}^{-1}$ ].

There are two ways to compute the fluid density in FEFLOW according to its linear or nonlinear dependency on temperature. The equation below shows the nonlinear relationship between temperature and fluid density (Diersch, 2013), which was adopted in this study:

$$\rho(T_c) = a_0 + a_1 T_c + a_2 T_c^2 + a_3 T_c^3 + a_4 T_c^4 + a_5 T_c^5 + a_6 T_c^6 \quad (3.12)$$

where

$\rho$  = fluid density [ $\text{ML}^{-3}$ ]

$a_0$  = fluid density at  $T_c = 0$   $^{\circ}\text{C}$  [ $\text{ML}^{-3}$ ]

$a_0$  to  $a_6$  = coefficients for water [ $\text{ML}^{-3}$ ] with  $a_0 = 9.998396 \cdot 10^2$ ;  $a_1 = 6.764771 \cdot 10^{-2}$ ;

$a_2 = -8.993699 \cdot 10^{-3}$ ;  $a_3 = 9.143518 \cdot 10^{-5}$ ;  $a_4 = -8.907391 \cdot 10^{-7}$ ;  $a_5 = 5.291959 \cdot 10^{-9}$ ;

$$a_6 = -1.359813.$$

Both the effective thermal conductivity and the effective volumetric heat capacity used in FEFLOW are bulk values computed using the thermal properties of the solid and fluid phases, and the porosity of the solid matrix (Diersch, 2013):

$$\lambda_e = (1 - \varepsilon) \lambda_s + \varepsilon \lambda_w \quad (3.13)$$

$$C_e = (1 - \varepsilon) C_s + \varepsilon C_w \quad (3.14)$$

where

$\lambda_e$  = effective thermal conductivity [ $\text{MLK}^{-1}\text{T}^{-3}$ ]

$C_e$  = effective volumetric heat capacity [ $\text{ML}^{-1}\text{K}^{-1}\text{T}^{-2}$ ].

The gas phase is ignored in the equations above because it is usually assumed to be stagnant and to not influence heat transport significantly in unsaturated porous media (Diersch, 2013).

The finite element method is implemented within FEFLOW to solve the nonlinear differential equations (governing equations, boundary and initial conditions) by transforming them into a set of linear algebraic equations that can be expressed in the form of a matrix (Diersch, 2016). For solving the matrix, FEFLOW offers users multiple iterative and two direct equation solvers. The multiple iterative solvers use a preconditioned conjugate-gradient (PCG) solver for the symmetric (fluid flow) equation system and a BICGSTABP-type solver for the unsymmetric (heat transport) equation

system. The iterative solvers are the default setting in FEFLOW and were applied in this study because they can solve problems with arbitrary size (Diersch, 2016).

## **Chapter 4 : Numerical simulations of seasonal temperature variations for the case of bulk seepage only**

### **4.1 Introduction**

To investigate the effects of seepage flow on seasonal temperature variations within the Mactaquac dam, a three-dimensional flow and heat transport model of the dam-concrete structure was constructed in FEFLOW. The main purpose of this chapter is to simulate temperature distributions that would be expected near the dam/concrete interface for the case of bulk, or distributed, seepage only (i.e. no concentrated anomalous seepage paths). A parametric analysis was performed to investigate the influence of selected thermal-hydraulic properties of the concrete and embankment materials on the coupled hydro-thermal flow, and to determine the parameter values most applicable to conditions at the Mactaquac site.

The 3D geometry of the dam-concrete structure generated in FEFLOW is shown in Figure 4-1. The model domain measures 174.06 m long by 48.46 m tall, while the width is 30.6 m, plus 13.72 m for the concrete rollway structure found on the north side of the SEP. The crest of the SEP rollway structure is at an elevation of 80 ft or 24.4 m (above mean sea level) with the maximum elevation of the model at 138 feet (42.1 m). As shown in Figure 4-1, the clay till core-concrete interface is inclined  $56.3^\circ$  from horizontal in the longitudinal section through the plane where the borehole is located.

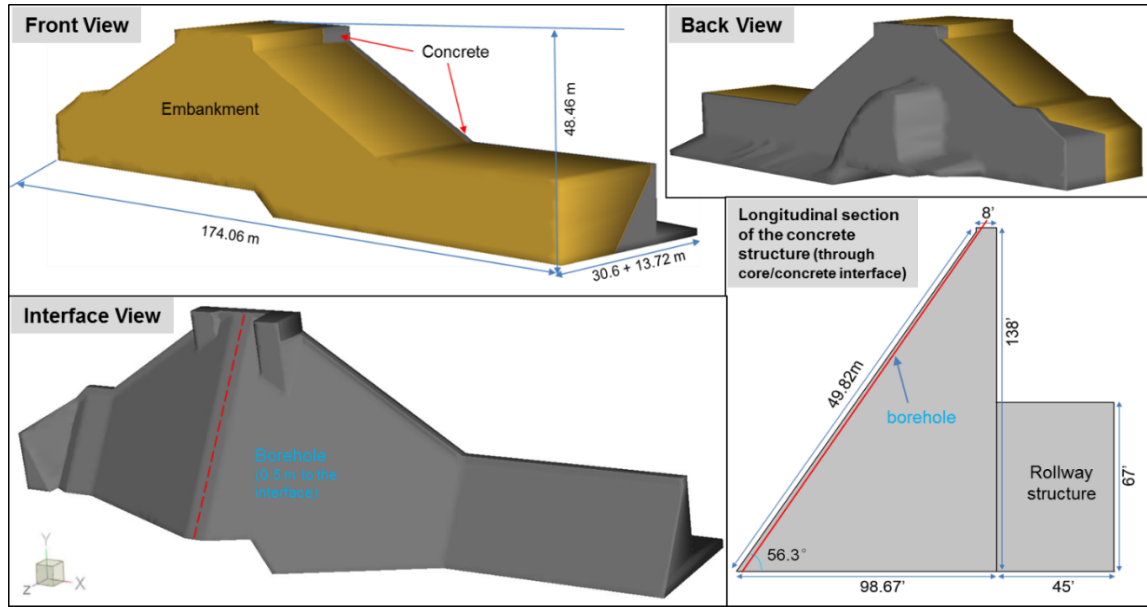


Figure 4-1: 3D geometry of the dam-concrete structure generated in FEFLOW along with a longitudinal section through the clay till core/concrete interface.

## 4.2 Simulation of heat transport near the dam/concrete interface – bulk seepage only

### 4.2.1 Finite element grid

The 3D model domain in FEFLOW was generated via layered meshes. All layers were constructed by horizontally extruding an existing 2D vertical mesh, which is also called a supermesh (Diersch, 2016). The supermesh defines outer boundaries and interior contacts within the model domain. Figure 4-2 shows the 2D supermesh and the 3D meshed domain. The 2D supermesh was divided into several small sections for the purpose of defining interface geometry, different material zones, locations of observation points (along the borehole), and so on. The 3D meshed domain consisted of 204,084 triangular prism elements, 112,294 nodes and 12 layers. The finite element meshes were generated using the GridBuilder algorithm (Diersch, 2010) within

FEFLOW with mesh refinement (elements subdivided into smaller ones) around the borehole, seepage zones and interface.

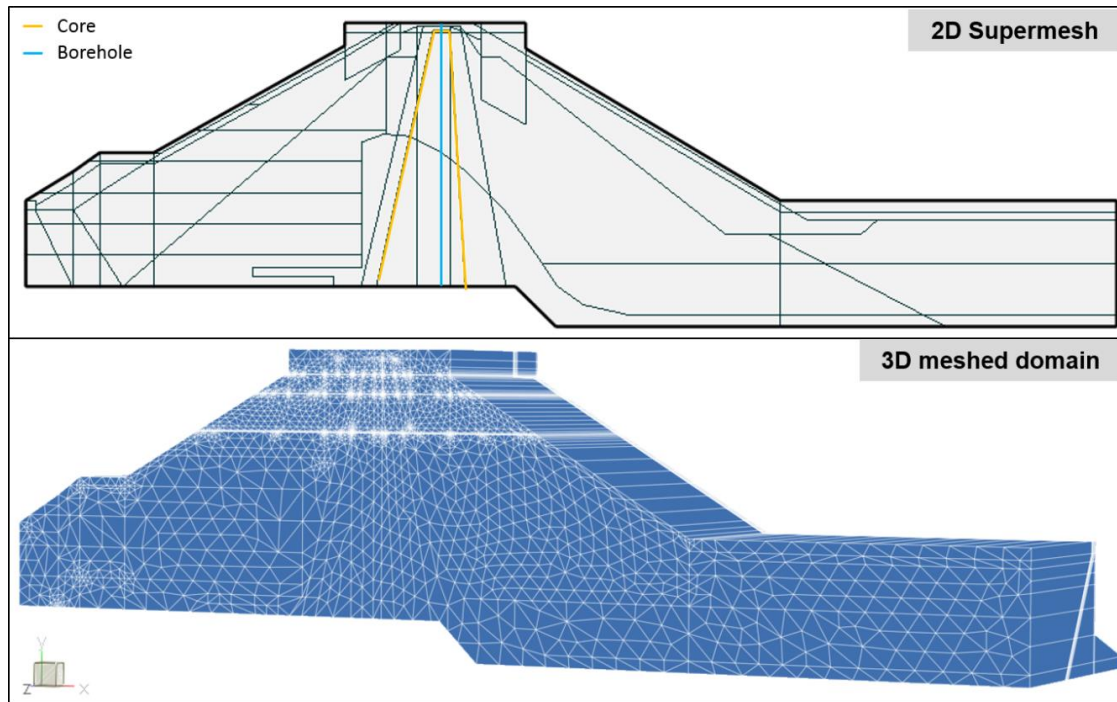


Figure 4-2: 2D supermesh and 3D meshed model domain for the dam/concrete structure.

To define the geometry of the dam/concrete interface and the SEP rollway structure, a combination of uniform model layers and deformed model layers was applied. Details of the layer discretization are shown in Figure 4-3. Four vertical slices (labelled 1, 11, 12, and 13) and nine slices following the interface geometry (labelled 2 - 10) were applied. Slice 6 is defined as the dam/concrete interface. The embankment portion of the model domain was discretized into 5 layers while the concrete segment was discretized into 7 layers. A set of 66 vertical linear observation points was arranged on slice 8 to represent the borehole SEPI-3, which is located 0.5 m from the interface (Figure 4-4).

An optimal spatial discretization for a 3D model should have a resolution that allows for the adequate representation of abrupt changes in the modelled quantities, but also uses as few elements and layers as possible to avoid extensive simulation times (Reilly & Harbaugh, 2004). Numerical effects, such as numerical dispersion, should be avoided or minimized when considering spatial discretization. A suggested criterion to constrain numerical errors for heat transport is the thermal Péclet criterion, which is defined as (Blecher et al., 2012; Wong et al., 2004):

$$P_e = \frac{\rho C_p \Delta l u}{\lambda_w} \leq 2 \quad (4.1)$$

where:

$P_e$  = Péclet number [-]

$\rho$  = fluid density [ $ML^{-3}$ ]

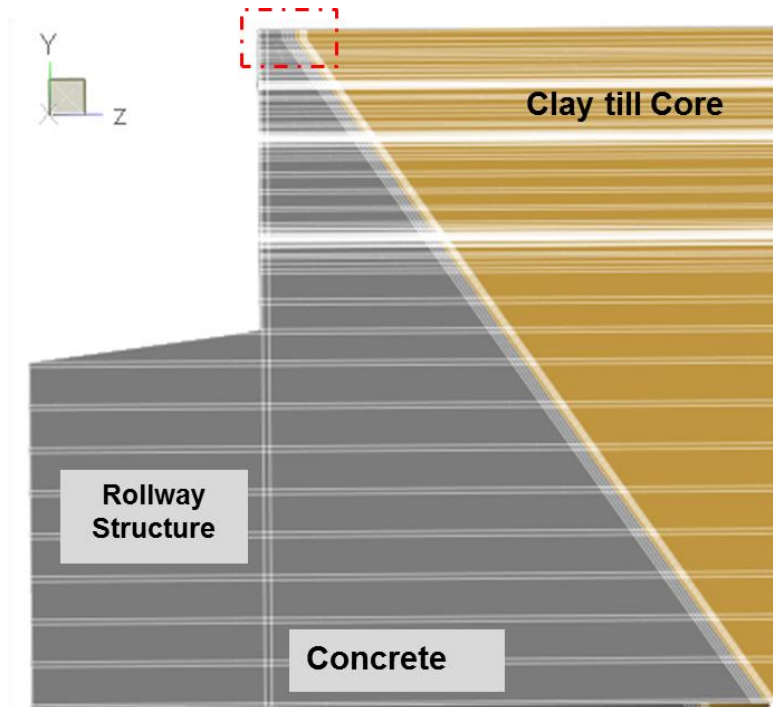
$C_p$  = specific heat of water [ $L^2K^{-1}T^{-2}$ ],  $C_p = \rho C_w$ , where  $C_w$  is the volumetric heat capacity of water [ $ML^{-1}K^{-1}T^{-2}$ ].

$\Delta l$  = maximum length of the finite element [L]

$u$  = average linear velocity [ $LT^{-1}$ ]

$\lambda_w$  = thermal conductivity of water [ $MLK^{-1}T^{-3}$ ].

Although the deformed layers between slice 1 and 2, as well as between slice 10 and 11, (Figure 4-3) introduced some elements with lengths as large as 28.7 m in the z direction, the mesh density is still acceptable compared to the Péclet criterion due to the very low average linear velocity in the z direction.



**Magnified view**

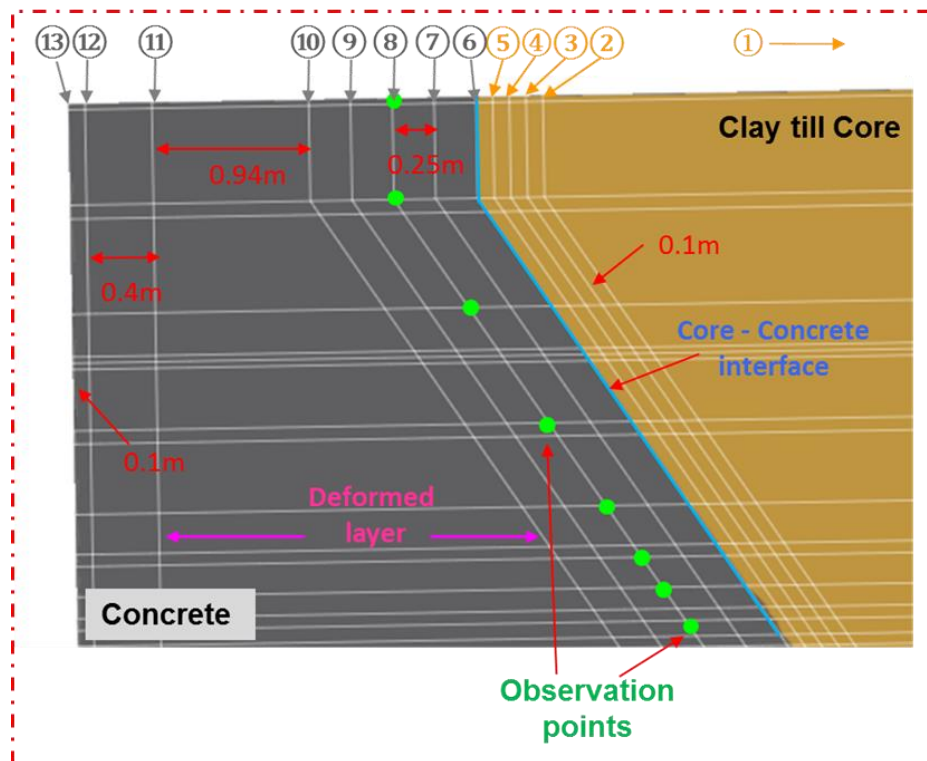


Figure 4-3: A longitudinal section through the clay till core/concrete interface showing details of the layer discretization within the 3D dam-concrete model domain. The circled numbers indicate the slice numbers, and the green dots represent observation points where simulated temperatures were extracted for comparison to the borehole DTS data.

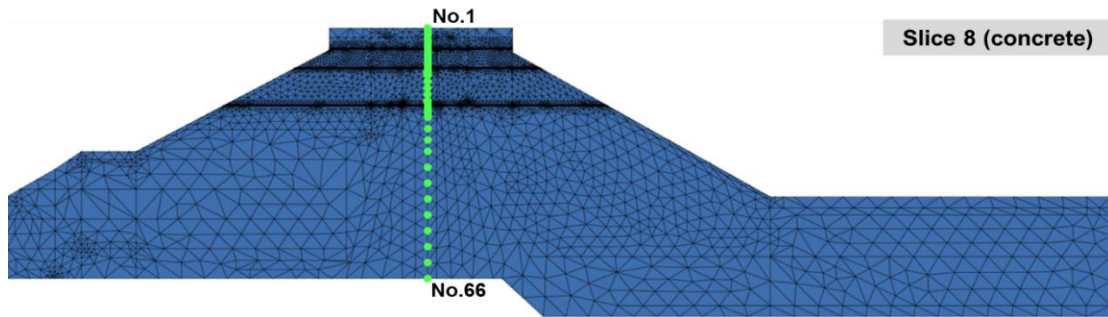


Figure 4-4: View of slice 8 showing the location of observation points (green dots) where temperatures were simulated for comparison to those measured along the DTS cable in borehole SEPI-3.

In reality, the embankment dam extends approximately 13 m (42') deeper and is 131 m (429') wider than the SEP concrete structure. However, the outer boundaries of the 2D supermesh were limited to the dimensions of the concrete structure and those portions of the embankment dam that extend beyond the concrete were not included in the model. As the upper surfaces of the embankment dam are at lower elevations than the concrete structure, mesh element deactivation was applied in FEFLOW to achieve different geometries for different segments in the model domain. Figure 4-5 shows the areas of inactive elements assigned to the meshed layers of the embankment segment. The mesh nodes surrounded by inactive elements are also inactive, which means FEFLOW does not compute results at these nodes for the entire simulation time.

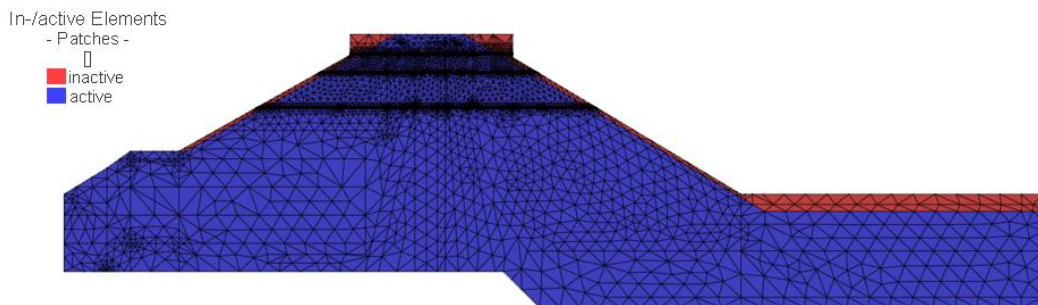


Figure 4-5: Elements deactivated (in red) for layers of the zoned rock-fill dam segment (slice 1 to 5) to achieve different geometry from the concrete segment in one model domain.

#### 4.2.2 *Initial and boundary conditions*

A spatially uniform temperature of 8 °C and a maximum headpond water surface elevation of 40.507 m (132.86') were set as the initial conditions for bulk seepage simulations.

The hydraulic boundary conditions for the embankment and the concrete segment are depicted separately in Figure 4-6. The boundary nodes along the upstream and downstream face of the embankment segment are slightly different from those of the concrete segment due to the element deactivation discussed above.

A Dirichlet (1<sup>st</sup> type) boundary condition for hydraulic head was imposed along the upstream dam face with a time-varying headpond water elevation. The maximum headpond water elevation was 40.507 m (132.86'). A constant tail-water elevation (1<sup>st</sup> type) of 3.658 m was specified at the dam toe. A seepage face boundary condition (1<sup>st</sup> type) was assigned along the downstream face of the dam which includes additional constraints (i.e. maximum flux = 0 m<sup>3</sup>/s) that only allows outflow (Diersch 2009a). For both the top and bottom boundaries, zero flux Neumann boundary conditions (2<sup>nd</sup> type) were set in FEFLOW by default, so that no water could enter or leave the domain through these boundaries.

Figure 4-7 shows the thermal boundary conditions for the embankment and the concrete segments along with special boundary conditions required for slices 13 and 6, which represented the outer concrete wall and the dam/concrete interface on the north and the south sides of the SEP, respectively. The time-varying water, air, and foundation

temperature profiles applied for thermal boundary conditions are presented in Figure 4-8.

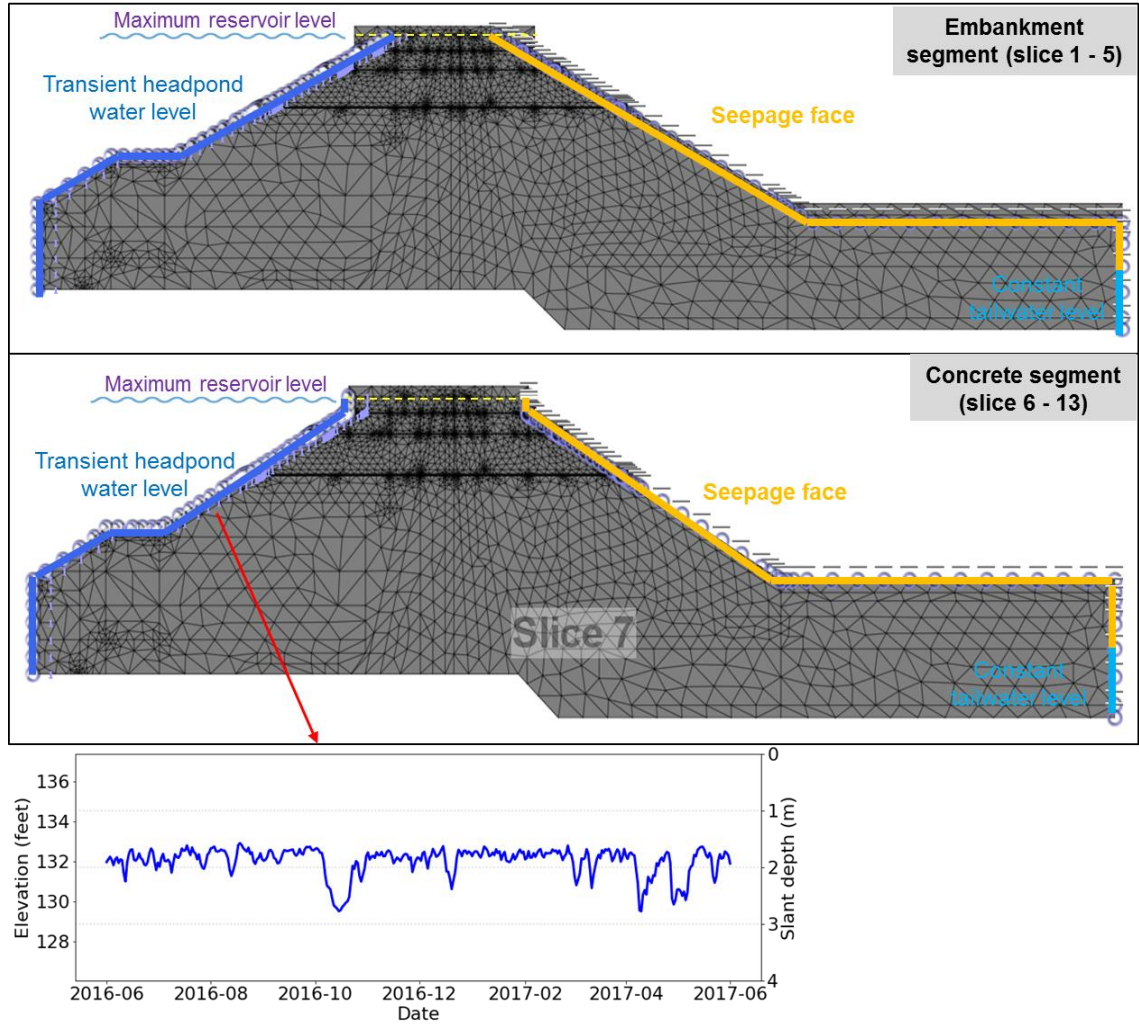


Figure 4-6: Hydraulic boundary conditions for the embankment and concrete segments of the model domain along with daily average time-varying headpond water elevations for June 1, 2016 – May 30, 2017.

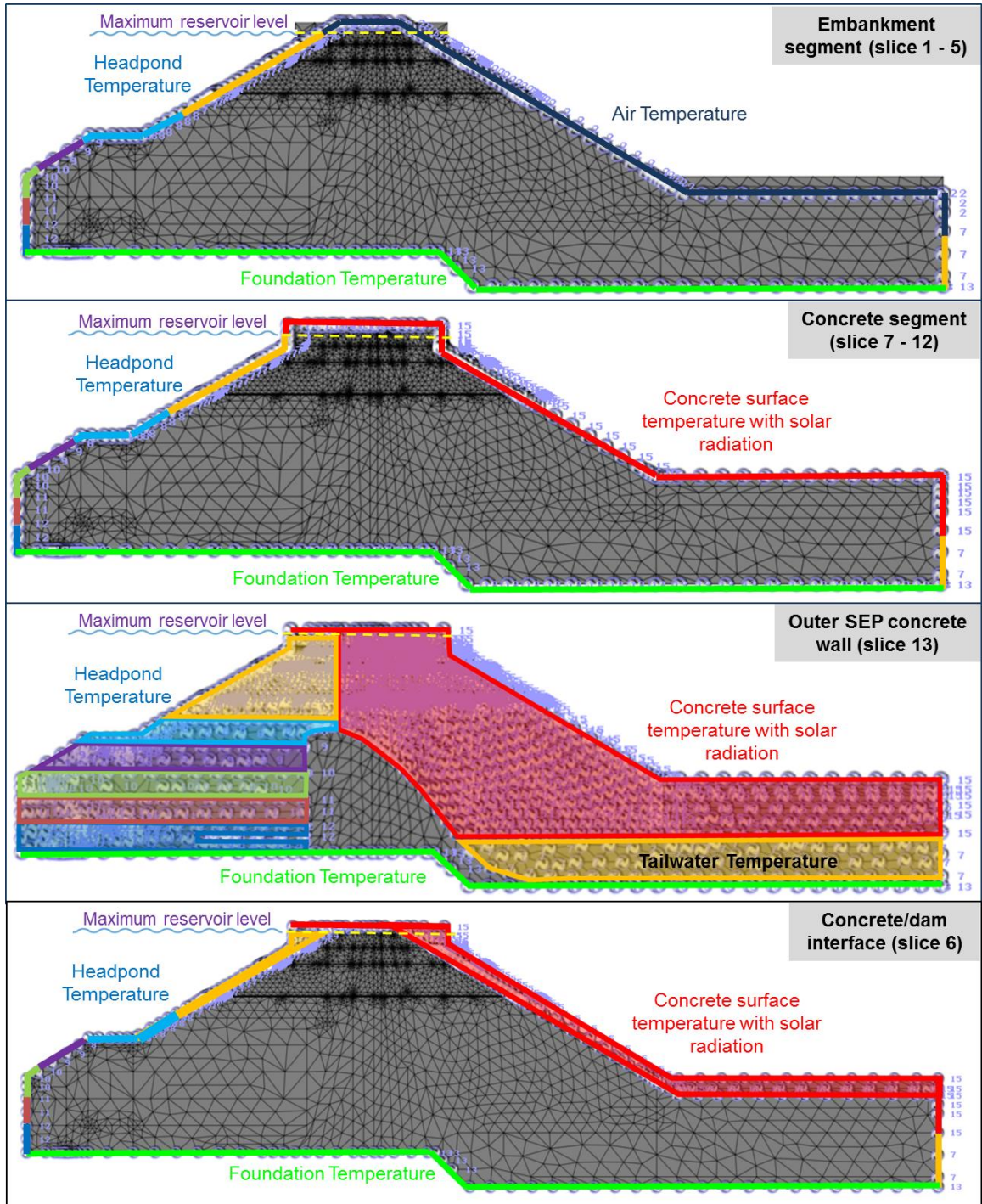


Figure 4-7: Thermal boundary conditions for the embankment and concrete segments along with the slices specified as the SEP concrete wall and the dam/concrete interface. The multiple colored line segments shown in the headpond correspond to temperatures at various depths as shown in Figure 4-8 a).

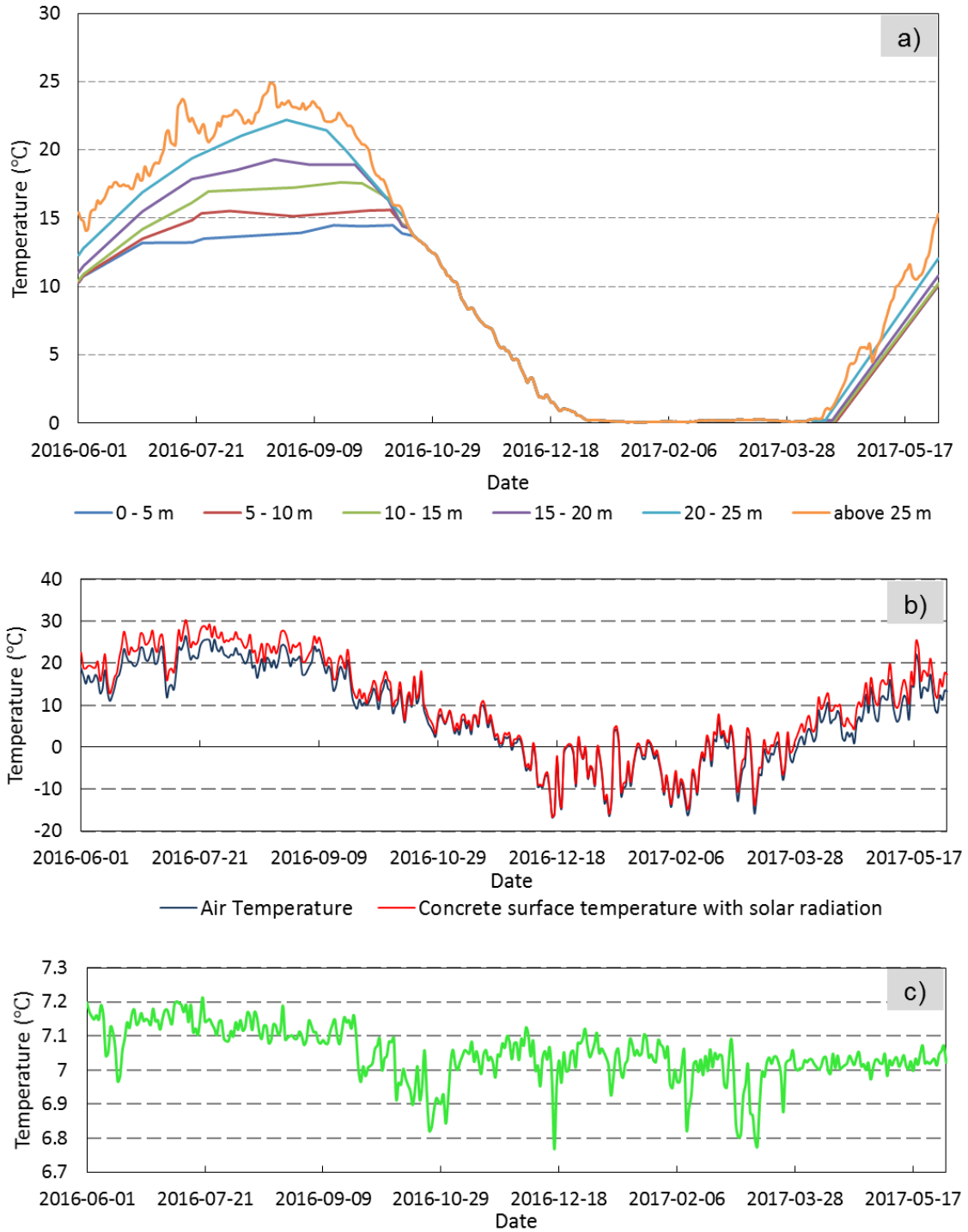


Figure 4-8: Temperature time series applied for thermal boundary conditions: a) daily average headpond temperatures, averaged over 5 m intervals from the bottom of the model domain; b) daily average air temperature and concrete surface temperature; c) daily average foundation temperature.

Time-varying headpond water temperatures, averaged over 5 m depth increments from the bottom of the model domain, were specified along the submerged upstream dam face. The headpond temperature during winter shows a vertically uniform temperature close to 0 °C, while the temperature in summer varies from as high as 25 °C at the surface to 14.5 °C at the bottom (Figure 4-8a). The time-dependent headpond temperature near the surface was also assigned as a boundary condition (1<sup>st</sup> type) for the tail water temperature along the submerged downstream toe of the dam. The temperature measured by the DTS system at the bottom of the borehole, which is assumed to be representative of the foundation temperature, was assigned to all nodes along the bottom boundary of the domain.

Daily average air temperatures were imposed along the top and downstream dam face for the unsubmerged embankment segment. The mean air temperature ranged from -15 °C in winter to a maximum of 25 °C in summer. The temperature increase caused by solar radiation was taken into account when estimating the surface temperature of the exposed concrete. The temperature increase due to solar radiation was estimated as follows (Bofang, 2013):

$$\Delta T = S (1 - k_1 c) \alpha_s k / \sigma \quad (4.2)$$

where  $\Delta T$  is the temperature increment (K) and  $S$  is the total solar radiation ( $MT^{-3}$ ). The constant  $k_1$  is the latitude coefficient which is equal to 0.66 at latitude 45 degrees for the Mactaquac site (Bofang, 2013), and  $c$  is the cloud coefficient which was roughly estimated to be 0.4.  $\alpha_s$  and  $\sigma$  are the concrete heat absorption coefficient (dimensionless) and the surface conductance ( $MK^{-1}T^{-3}$ ), which are equal to 0.5 and 80

$\text{kJ/m}^2\text{h}^\circ\text{C}$ , respectively (Bofang, 2013). The topography coefficient  $k$  was estimated to be 0.75 based on the downstream slope of the dam and surrounding topographies (Bofang, 2013). The mean annual increase in concrete surface temperature was estimated to be  $2.1\text{ }^\circ\text{C}$  with a maximum temperature increment of  $4.2\text{ }^\circ\text{C}$  in July and a minimum temperature increment of  $0.12\text{ }^\circ\text{C}$  in January.

Additional thermal boundary conditions on the interior nodes were assigned on slice 13 and slice 6. Thermal boundary conditions assigned on the interior nodes of slice 6 were required to account for different geometries between the concrete and the embankment segments, thus resulting in part of the concrete surface near the borders being directly exposed to air and headpond water. The outer (northern) concrete wall of the SEP is also directly exposed to air and headpond water except for the part in contact with the concrete rollway structure. The headpond temperature and the concrete surface temperature boundary conditions assigned on the interior nodes of slice 13 were divided by a vertical line above the SEP rollway structure, which represented the position of the floodgate.

#### *4.2.3 Material properties*

The properties of the concrete segment of the model domain are assumed to be homogeneous and isotropic. Distributions of different constructed materials in the zoned rock-fill embankment dam are depicted in Figure 4-9, which is based on an embankment design cross-section (Acres, 1968) generated during construction for the middle of the dam, about 300 m away from the dam/concrete interface (Figure E.1, Appendix E).

Photographic evidence (Figure E.2, Appendix E) from the time of dam construction indicates that the impervious clay till core was made wider at its southern abutment. Similarly, according to recollections of a senior geotechnical engineer involved in the dam construction (A. Landva, pers. comm., 2017) the core was widened at its northern end in order to wrap around the inclined ‘nose’ of the concrete SEP. However, no photographs, drawings or documentation could be found to more precisely constrain its dimensions. The core was constructed of a well-graded clay till, which was excavated from a borrow pit located about 1.4 km northwest of the Mactaquac Generating Station (Keenan, 1969). The mean grading of the till material was estimated to be 24% gravel, 27% sand, 31% silt and 18% clay (Keenan, 1969). Conlon & Ganong (1966) indicated that the rockfill for the shells of the embankment was to be obtained from excavations of the intensely folded and fractured/jointed metamorphosed Silurian bedrock – chiefly greywacke and slate – made for the channels and concrete structures of the generating station. The shells were further subdivided into four types (Figure 4-9) based on the gradation of the rock, and the compaction and dumping methods during the construction. Conlon & Ganong (1966) noted the transition zone between rockfill and core was expected to be constructed from “some of the very fine rock fill” obtained from excavations.

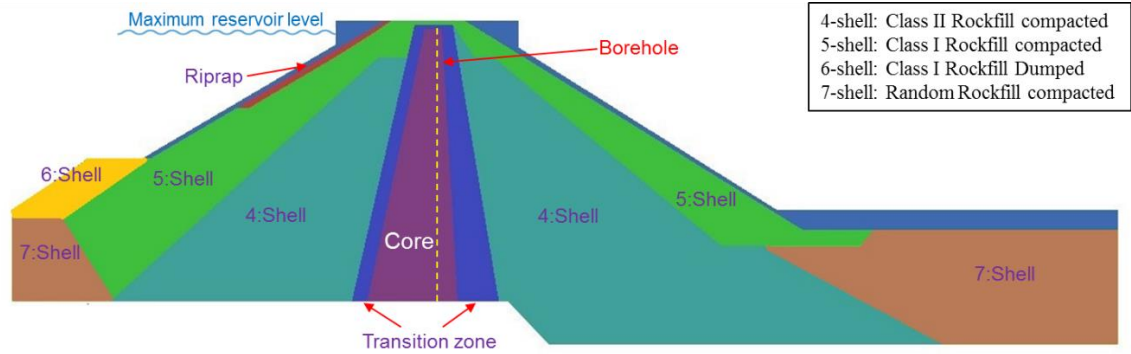


Figure 4-9: Distributions of different materials in the zoned rock-fill embankment dam. The yellow dashed line indicates the projection of SEPI-3 borehole into the embankment dam.

As we did not have access to the materials used for the dam construction to perform physical property testing, most of the thermal-hydraulic properties required for the numerical simulations were initially based on a review of experimental and field values published in the literature. Those initial thermal-hydraulic property estimates are shown in Table 4-1. Numerous bulk seepage simulations were then performed to refine, by trial and error, various material properties to improve the fit between simulated temperature variations and those measured by the DTS in borehole SEPI-3.

An average porosity of 0.15 was applied to the concrete based on Hanke's (2014) measurements on core from borehole SEPI-3 drilled into the SEP. The concrete hydraulic conductivity value was selected based on a published value ( $1 \times 10^{-12}$  m/s) for moderate-strength concrete used in dams (Mehta & Monteiro, 1993). The hydraulic conductivity and the porosity for different zones in the embankment dam were estimated based on the studies of Velásquez (2007), Song and Yosef (2017), and Alejandro (2014). The hydraulic conductivity for a clay till core used in these studies varies from  $1 \times 10^{-6}$  m/s to  $1 \times 10^{-9}$  m/s. The anisotropy ratio for the dam was derived from the study by

Mairaing and Lapkengkrai (1993), who reported an anisotropy ratio for relatively fine-grained and coarse-grained compacted soils in earth embankments ranging from 2.1 to 7.0, and 2.2 to 7.5, respectively.

The thermal conductivity and volumetric heat capacity of the solid and fluid phases are required separately in FEFLOW. Typical thermal properties of the solid phase of the concrete and the rock-fill shells in the embankment dam were estimated from the values in Leger et al. (1993), which reported the values of thermal properties in the form of constituent materials. For the core and filter, typical thermal properties for till and sand were applied as documented by Markle and Schincariol (2007). FEFLOW default values were used for the thermal conductivity and the heat capacity of water. Dispersivity values, which are also related to thermal transport processes, are strongly scale-dependent parameters. For a medium-sized dam, the longitudinal dispersivity should not be larger than 1.0 m as recommended by Velásquez (2007), while the transverse dispersivity is typically one order of magnitude smaller than the longitudinal dispersivity.

The modified van Genuchten model was chosen to describe the unsaturated flow characteristics of the porous media. The van Genuchten parameters and residual saturation assigned to both the concrete and the inner embankment zones were selected based on the values used by Shija and MacQuarrie (2015). The van Genuchten parameters for riprap were chosen from Diersch and Perrochet (2009).

Table 4-1: Thermal-hydraulic property values for FEFLOW simulations.

Parameters			Concrete	Core	Transiti	Rock-fill shells				9:	Water
Category	Parameter	Unit			on zone	4: shell	5: shell	6: shell	7: shell	riprap	
<b>Saturated flow</b>	Hydraulic conductivity, K	[ms <sup>-1</sup> ]	1.0 x 10 <sup>-12g</sup>	1.0 x 10 <sup>-7ij</sup>	5.21 x 10 <sup>-6ij</sup>	5.0 x 10 <sup>-5ij</sup>	4.6 x 10 <sup>-4ij</sup>	1.0 x 10 <sup>-3aj</sup>	1.0 x 10 <sup>-3aj</sup>	5.0 x 10 <sup>-2aj</sup>	
	Anisotropy ratio, r	[-]	1.0	4.0 <sup>d</sup>	4.0 <sup>d</sup>	3.5 <sup>d</sup>	3.5 <sup>d</sup>	3.5 <sup>d</sup>	3.5 <sup>d</sup>	1.0	
<b>Unsaturated flow</b>	Porosity, ε	[-]	0.15 <sup>c</sup>	0.46 <sup>ij</sup>	0.42 <sup>ij</sup>	0.35 <sup>ij</sup>	0.35 <sup>ij</sup>	0.30 <sup>aj</sup>	0.30 <sup>aj</sup>	0.30 <sup>aj</sup>	
	Curve fitting parameter, α	[m <sup>-1</sup> ]	5.10 x 10 <sup>-4h</sup>	1.10 <sup>h</sup>	2.80 <sup>h</sup>	2.80 <sup>h</sup>	2.80 <sup>h</sup>	2.80 <sup>h</sup>	2.80 <sup>h</sup>	3.60 <sup>h</sup>	
	Curve fitting parameter, n	[-]	1.50 <sup>h</sup>	1.40 <sup>h</sup>	2.24 <sup>h</sup>	2.24 <sup>h</sup>	2.24 <sup>h</sup>	2.24 <sup>h</sup>	2.24 <sup>h</sup>	3.03 <sup>h</sup>	
	Curve fitting parameter, m	[-]	0.34 <sup>h</sup>	0.29 <sup>h</sup>	0.55 <sup>h</sup>	0.55 <sup>h</sup>	0.55 <sup>h</sup>	0.55 <sup>h</sup>	0.55 <sup>h</sup>	0.67 <sup>h</sup>	
	Curve fitting parameter, δ	[-]	1.00 <sup>h</sup>	1.00 <sup>h</sup>	1.00 <sup>h</sup>	1.00 <sup>h</sup>	1.00 <sup>h</sup>	1.00 <sup>h</sup>	1.00 <sup>h</sup>	1.00 <sup>h</sup>	
	Maximum saturation, s <sub>s</sub>	[-]	1.00	1.00	1.00	1.00	1.00	1.00	1.00	1.00	
	Residual saturation, s <sub>r</sub>	[-]	0.20 <sup>h</sup>	0.23 <sup>h</sup>	0.10 <sup>h</sup>	0.08 <sup>h</sup>	0.08 <sup>h</sup>	0.08 <sup>h</sup>	0.08 <sup>h</sup>	0.08 <sup>h</sup>	0.025 <sup>b</sup>
<b>Heat transport</b>	Thermal conductivity of solid, λ <sub>s</sub>	[Wm <sup>-1</sup> K <sup>-1</sup> ]	3.90 <sup>d</sup>	4.05 <sup>f</sup>	3.00 <sup>f</sup>	3.00 <sup>d</sup>					
	Thermal conductivity of fluid, λ <sub>f</sub>	[Wm <sup>-1</sup> K <sup>-1</sup> ]									0.65 <sup>k</sup>
	Volumetric heat capacity of solid, C <sub>s</sub>	[MJm <sup>-3</sup> K <sup>-1</sup> ]	2.40 <sup>d</sup>	2.24 <sup>f</sup>	2.21 <sup>d</sup>	2.21 <sup>d</sup>	2.21 <sup>d</sup>	2.21 <sup>d</sup>	2.21 <sup>d</sup>	2.21 <sup>d</sup>	
	Volumetric heat capacity of fluid, C <sub>w</sub>	[MJm <sup>-3</sup> K <sup>-1</sup> ]									4.20 <sup>k</sup>
	Longitudinal dispersivity, α <sub>L</sub>	[m]	1.0 <sup>j</sup>	1.0 <sup>j</sup>	1.0 <sup>j</sup>	1.0 <sup>j</sup>	1.0 <sup>j</sup>	1.0 <sup>j</sup>	1.0 <sup>j</sup>	1.0 <sup>j</sup>	1.0 <sup>j</sup>
	Transverse dispersivity, α <sub>T</sub>	[m]	0.1 <sup>j</sup>	0.1 <sup>j</sup>	0.1 <sup>j</sup>	0.1 <sup>j</sup>	0.1 <sup>j</sup>	0.1 <sup>j</sup>	0.1 <sup>j</sup>	0.1 <sup>j</sup>	0.1 <sup>j</sup>

Note: a) Alejandro, 2014; b) Diersch & Perrochet, 2009; c) Hanke, 2014; d) Leger et al., 1993; e) Mairaing & Lapkrengrai, n.d.; f) Markle & Schincariol, 2007; g) Mehta & Monteiro, 1993; h) Shija & MacQuarrie, 2015; i) Song & Yosef, 2017; j) Velásquez, 2007; k) FEFLOW default value.

#### *4.2.4 Numerical settings for the simulation of bulk seepage*

The pressure head-based ( $\psi$ ) form of Richards' equation was adopted as the governing equation to solve for the variably-saturated flow, and the convection form of the transport equations was applied. Variable fluid viscosity which is dependent on temperature was used, and the fluid density was determined by a nonlinear relationship with temperature (Diersch, 2013).

A cyclic simulation of four years based on seasonal variations in air temperature, headpond temperature, and headpond water levels measured between June 2016 and June 2017 was carried out to reach a dynamic steady state condition, with the simulation results from the final year being used for analysis. A first-order accurate Forward Euler/Backward Euler (FE/BE) predictor-corrector scheme was selected to control the time-step length with an initial time step of 0.001 day.

A preconditioned conjugate-gradient (PCG) solver was used for the symmetric (fluid flow) equation system, and a BICGSTABP-type solver was selected for the unsymmetric (heat transport) equation system (Diersch, 2013). The error tolerance, defined as the averaged absolute error (change in the primary variable) divided by the maximum value occurring in initial or boundary conditions (Diersch, 2016), was set to be  $1.0 \times 10^{-3}$ , and the maximum number of iterations per time step was set to 12.

### **4.3 Parameter sensitivity analysis**

Before the initial choices of thermal-hydraulic parameters could be refined, parameter sensitivity analysis was undertaken to investigate the relative importance of

different properties on the coupled hydro-thermal flow within the dam. By conducting numerical modelling for bulk seepage only, with various values for selected parameters, it was determined that porosity, longitudinal and transverse dispersivity, modified van Genuchten fitting parameters, and residual saturation in the ranges recommended by Velásquez (2007) did not significantly affect the simulated temperature distributions and seepage rates within the dam. Besides, it was also determined that the hydraulic conductivity, thermal conductivity and volumetric heat capacity of the filter, shells and riprap did not significantly affect the simulated temperature along the borehole which was installed near the core/concrete interface. Thus, discussions below concentrate on analysing the effects of the hydraulic conductivity, thermal conductivity and volumetric heat capacity of the core and concrete.

The material property values presented in Table 4-1 were used as scenario B1, then the hydraulic conductivity, anisotropy ratio for hydraulic conductivity, and thermal conductivity were varied to build up another 8 scenarios as denoted in Table 4-2. As the variations of thermal conductivity produced very similar effects on the simulated temperature distributions and seepage rate, only the simulation results for variations in thermal conductivity are presented.

Table 4-2: Parameter analysis: variations of hydraulic conductivity, anisotropy ratio and thermal conductivity for scenarios B1 to B9.

No.	Parameter	Concrete	Core	Filter	Rock-fill shells				9: riprap
					4: shell	5: shell	6: shell	7: shell	
<b>B1</b>	K [ $\text{ms}^{-1}$ ]	$1.0 \times 10^{-12}$	$1.0 \times 10^{-7}$	$5.21 \times 10^{-6}$	$5.0 \times 10^{-5}$	$4.6 \times 10^{-4}$	$1.0 \times 10^{-3}$	$1.0 \times 10^{-3}$	$5.0 \times 10^{-2}$
	AR [-]	1.0	4.0	4.0	3.5	3.5	3.5	3.5	1.0
	$\lambda_s$ [ $\text{Wm}^{-1}\text{K}^{-1}$ ]	3.9	4.05	3.0	3.0	3.0	3.0	3.0	3.0
<b>B2</b>	K [ $\text{ms}^{-1}$ ]	$3.0 \times 10^{-11}$	x	x	x	x	x	x	x
	AR [-]	x	x	x	x	x	x	x	x
	$\lambda_s$ [ $\text{Wm}^{-1}\text{K}^{-1}$ ]	x	x	x	x	x	x	x	x
<b>B3</b>	K [ $\text{ms}^{-1}$ ]	x	$5.0 \times 10^{-7}$	x	x	x	x	x	x
	AR [-]	x	x	x	x	x	x	x	x
	$\lambda_s$ [ $\text{Wm}^{-1}\text{K}^{-1}$ ]	x	x	x	x	x	x	x	x
<b>B4</b>	K [ $\text{ms}^{-1}$ ]	x	x	x	x	x	x	x	x
	AR [-]	1.0	1.0	1.0	1.0	1.0	1.0	1.0	1.0
	$\lambda_s$ [ $\text{Wm}^{-1}\text{K}^{-1}$ ]	x	x	x	x	x	x	x	x
<b>B5</b>	K [ $\text{ms}^{-1}$ ]	x	x	x	x	x	x	x	x
	AR [-]	x	x	x	x	x	x	x	x
	$\lambda_s$ [ $\text{Wm}^{-1}\text{K}^{-1}$ ]	5.0	x	x	x	x	x	x	x
<b>B6</b>	K [ $\text{ms}^{-1}$ ]	x	x	x	x	x	x	x	x
	AR [-]	x	x	x	x	x	x	x	x
	$\lambda_s$ [ $\text{Wm}^{-1}\text{K}^{-1}$ ]	x	5.0	x	x	x	x	x	x
<b>B7</b>	K [ $\text{ms}^{-1}$ ]	x	$5.0 \times 10^{-7}$	x	x	x	x	x	x
	AR [-]	x	x	x	x	x	x	x	x
	$\lambda_s$ [ $\text{Wm}^{-1}\text{K}^{-1}$ ]	5.0	x	x	x	x	x	x	x
<b>B8</b>	K [ $\text{ms}^{-1}$ ]	x	$5.0 \times 10^{-7}$	x	x	x	x	x	x
	AR [-]	x	x	x	x	x	x	x	x
	$\lambda_s$ [ $\text{Wm}^{-1}\text{K}^{-1}$ ]	x	5.0	x	x	x	x	x	x
<b>B9</b>	K [ $\text{ms}^{-1}$ ]	x	$2.5 \times 10^{-7}$	x	x	x	x	x	x
	AR [-]	2.5	2.5	2.5	2.5	2.5	2.5	2.5	2.5
	$\lambda_s$ [ $\text{Wm}^{-1}\text{K}^{-1}$ ]	x	x	x	x	x	x	x	x

Note: “K” denotes the saturated hydraulic conductivity while “AR” denotes the anisotropy ratio for hydraulic conductivity. “ $\lambda_s$ ” denotes the thermal conductivity of the solids. “x” means the value of the parameter is the same as the value used in scenario B1.

#### 4.4 Results and discussion

The simulated temperature variations with depth, for 66 nodes located 0.5 m from the inclined till-concrete interface (Figure 4-4), are plotted in Figure 4-10 and Figure 4-11 for scenarios B1 to B8 over one year. The time series of daily average seepage rates for each scenario are shown in Figure 4-12 and Figure 4-13. The seepage rates represent the total outflow from the domain and were determined along the downstream slope of the dam. The annual average seepage rates are summarized in Table 4-3.

When compared to the DTS data (Figure 2-5), it is evident that the simulated temperature variations versus time plots show similar seasonal temperature variations near the surface and a relatively steady temperature pattern at greater depths. The temperature anomalies observed at elevation 113' to 120-129', and at elevation 95', in the DTS data do not appear in the simulated temperature distributions when considering bulk seepage only. All nine scenarios show similar seasonal variations for the simulated seepage rate, which is approximately 30% ( $20 \text{ m}^3/\text{d}$ ) higher in late summer than mid-winter. This is mainly due to the seasonal temperature variations in the air and headpond water (Figure 4-8) that affect the dynamic viscosity and density of the water, which in turn influence the seepage rate in the manner described in Chapter 3.

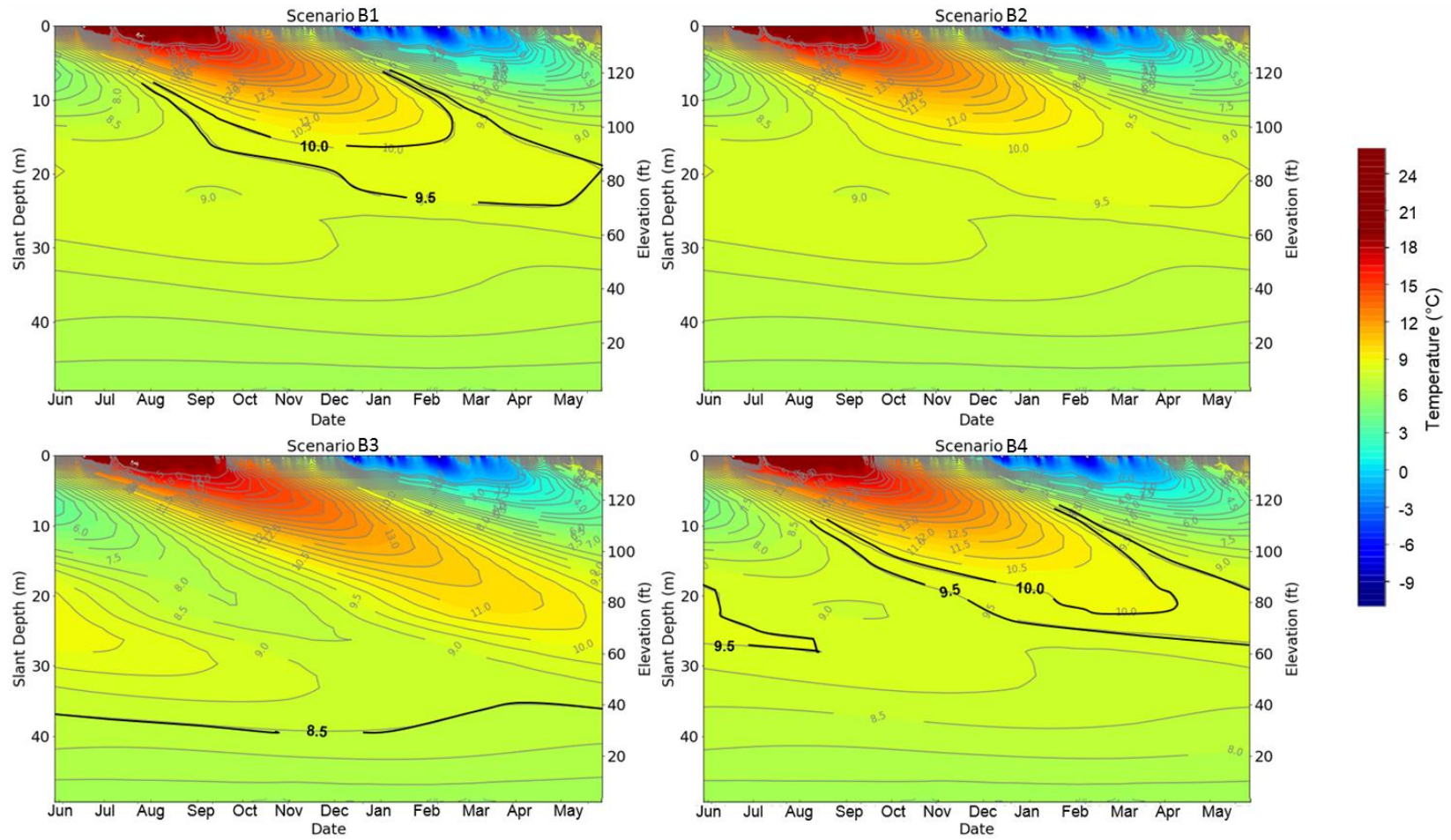


Figure 4-10: Simulated temperature variations versus time for scenarios B1 to B4. Several of the temperature contour lines have been highlighted in scenarios B1, B3 and B4 for easier visual comparison.

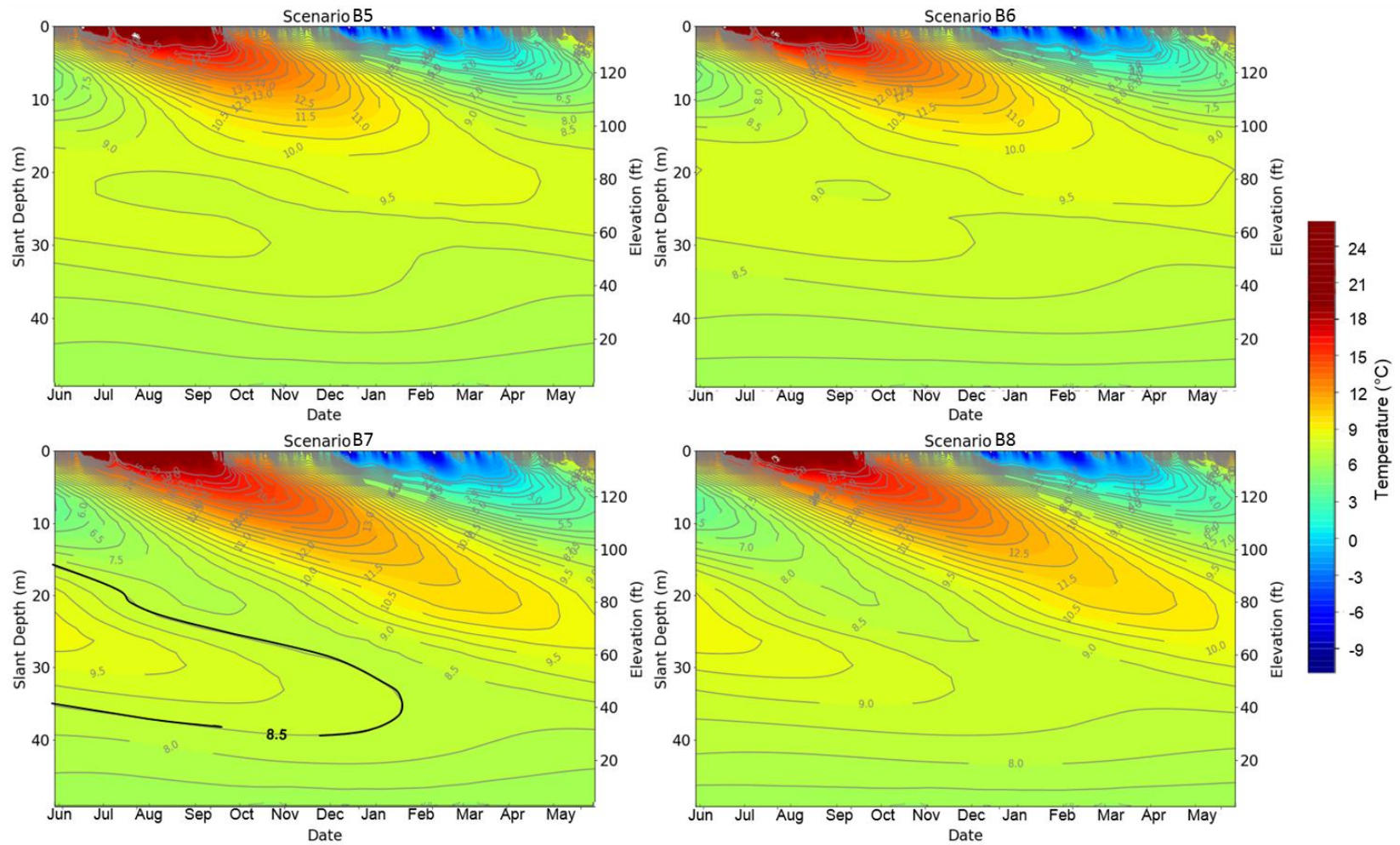


Figure 4-11: Simulated temperature variations versus time for scenarios B5 to B8. The 8.5 °C temperature contour line has been highlighted in scenario B7 for easier visual comparison.

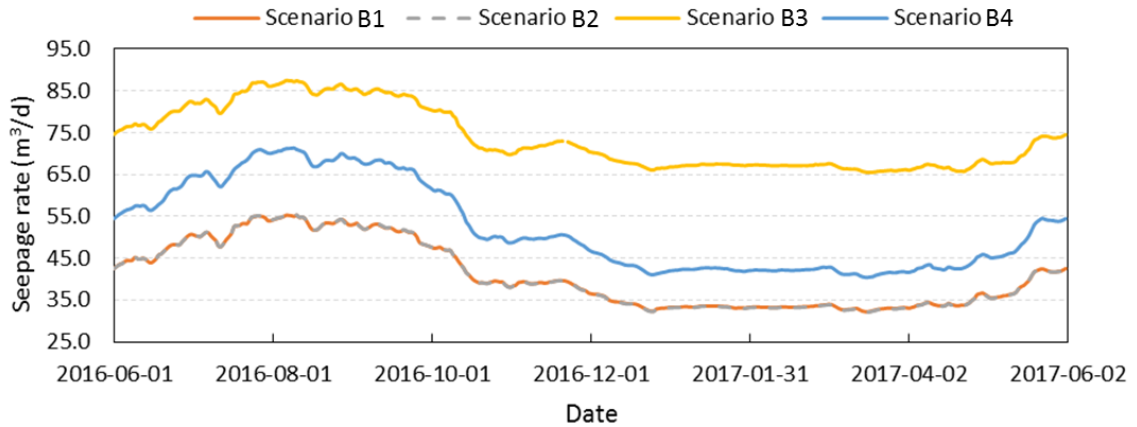


Figure 4-12: Bulk seepage simulations: comparison of seepage rate versus time for scenarios B1 to B4.

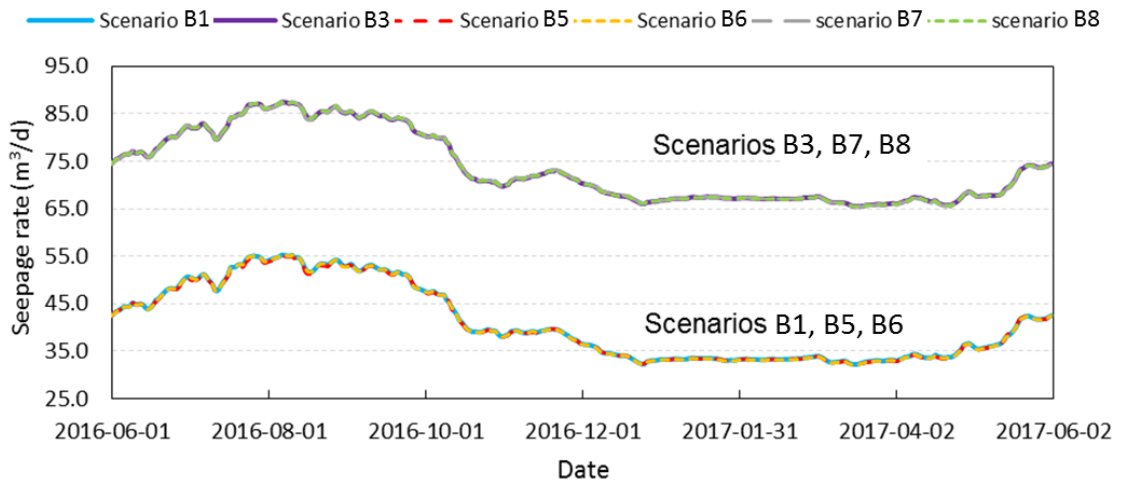


Figure 4-13: Bulk seepage simulations: comparison of seepage rate versus time for scenarios B1, B3 and B5 to B8.

Table 4-3: Bulk seepage simulations: annual average seepage rate for scenarios B1 to B9.

Scenario No.	B1	B2	B3	B4	B5	B6	B7	B8	B9
Seepage rate (m <sup>3</sup> /d)	41.0	41.0	73.7	52.3	41.0	41.0	73.6	73.7	57.1
(annual average)									

Comparisons between results for scenarios B2 to B4 with scenario B1 were implemented to analyze the effects of hydraulic conductivity and anisotropy ratio on the simulated temperature distributions and seepage rate.

The hydraulic conductivity of the concrete in scenario B2 is 30 times larger than the value assigned in scenario B1. However, no obvious differences between them can be found in the simulated temperature or the simulated seepage rate. Both scenarios show the simulated seepage rate ranges from 55.2 m<sup>3</sup>/d in August to 32.2 m<sup>3</sup>/d in January, with an average of 41.0 m<sup>3</sup>/d (Figure 4-12). This indicates that the simulated bulk seepage through the concrete is negligible compared to that through the embankment. This is not surprising given that the initial hydraulic conductivity assigned to the concrete was five orders of magnitude lower than that assigned to the core.

The hydraulic conductivity of the clay till core in scenario B3 ( $5.0 \times 10^{-7}$  m/s) is five times larger than that in scenario B1 ( $1.0 \times 10^{-7}$  m/s). The increase in the hydraulic conductivity of the core significantly increases the seepage rate, from an average of 41.0 m<sup>3</sup>/d (scenario B1) to 73.7 m<sup>3</sup>/d (scenario B3) (Figure 4-12). More heat is carried by the increased seepage flow and exchanged with the adjacent media, making the near-surface seasonal temperature variations for scenario B3 extend approximately 10 m deeper than in scenario B1 (Figure 4-10).

The hydraulic conductivity of the entire model domain in scenario B4 is assumed to be isotropic, as opposed to anisotropic, which means the hydraulic conductivity in the vertical direction is increased by 3.5 times for the embankment shells, and 4 times for

the core and the filter, when compared to scenario B1. A slightly deeper penetration of the seasonal temperature variations can be observed (identified by highlighted temperature contour lines of 9.5 °C and 10.0 °C in scenarios B1 and B4 in Figure 4-10) and the annual average seepage rate increased to 52.3 m<sup>3</sup>/d.

Comparisons of the results for scenarios B5 and B6 with scenario B1, and of scenario B7 and B8 with scenario B3 were carried out to investigate the influence of the thermal conductivity on the simulated temperature distributions and seepage rate.

The thermal conductivity of the concrete and the core were increased by a factor of 43% and 23% to 5.0 W m<sup>-1</sup>K<sup>-1</sup> in scenario B5 and B6, respectively. The results for these simulations exhibit no obvious differences in the simulated temperature and seepage rate when comparing to the results of scenario B1.

The thermal conductivities assigned in scenarios B7 and B8 are the same as those assigned in scenarios B5 and B6, respectively, but the hydraulic conductivity of the core was increased by a factor of five times to match that assigned in scenario B3. Increasing the hydraulic conductivity of the core along with the thermal conductivity of the concrete increases seasonal heat transport to greater depths than any of the previously considered scenarios (differences between scenarios B3 and B7 can be more easily identified by highlighted temperature contour lines of 8.5 °C in Figure 4-10 and Figure 4-11). This is mainly due to the enhancement of thermal conduction in the concrete. Comparisons between scenarios B1 and B5, along with scenarios B3 and B7, reveal that only when the seepage rate along the dam/concrete interface is large enough, which is related to the hydraulic conductivity of the core, is the influence of the thermal

conductivity of the concrete observed. In contrast, increasing the hydraulic and thermal conductivity of the core (scenario B8) does not produce any obvious change compared to only increasing the hydraulic conductivity of the core (scenario B3). One reason to explain these results is that the DTS cable was installed in the concrete, thus thermal conduction in the concrete is more important than that in the embankment. As expected, changes in the thermal conductivity had no influence on the seepage rate (Figure 4-13, Table 4-3).

According to the comparisons presented above, the following conclusions can be drawn: 1) of the parameters examined, the hydraulic conductivity of the core has the dominant influence on the bulk seepage rate and the temperature distributions, while changing the hydraulic conductivity of the concrete has insignificant influence as long as it remains much lower than that of the core (five orders of magnitude in this study); 2) by increasing the hydraulic conductivity of the core, the seasonal temperature variations controlled by the headpond water temperature extend to greater depths and the seepage rate will increase; 3) varying the thermal conductivity of the core (embankment) has an insignificant effect on the simulated temperatures, while increasing the thermal conductivity of the concrete will induce deeper penetration of the seasonal temperature variations, provided the hydraulic conductivity of the core is sufficiently high; and 4) varying the thermal conductivity does not influence the simulated seepage rate.

After the parameter sensitivity analysis (scenarios B1 to B8), scenario B9 was generated and adopted as the most representative bulk seepage simulation. The material property values for scenario B9 differ from the initial estimates in scenario B1 in that the core hydraulic conductivity was increased by a factor of 2.5, and the anisotropy ratios of

all materials were set to 2.5, which are still within the range recommended by Velásquez (2007) and Mairaing and Lapkengkrai (1993), for a moderate-sized dam. The temperature and hydraulic head fields on the last day (May 31, 2017) of the scenario B9 simulation were adopted as the initial conditions for subsequent anomalous seepage simulations to be discussed in Chapter 5. The simulated temperature distributions along the embankment/concrete interface (slice 6 in Figure 4-3) and on slice 1 through embankment, which is 30.6 m from the top of the SEP interface are shown for the first day of each month in Appendix F. The temperature variations versus time plot for scenario B9 and DTS data as well as the seepage rate time series for scenario B9 are shown in Figure 4-14. The simulated seepage rate ranges from 72.7 m<sup>3</sup>/d in August to 47.5 m<sup>3</sup>/d in January, with an average of 57.2 m<sup>3</sup>/d. The average seepage rate per unit width (divided by the average width of 23 m of the embankment segment) is 2.5 m<sup>3</sup>/d/m, which is lower than the reported values for seepage discharge between 14.6 – 21.3 m<sup>3</sup>/d/m for the Karkheh earth dam in Iran (Kamanbedast and Shahosseini, 2011). However, the Karkheh dam is approximately three times the height of the Mactaquac dam (Kamanbedast and Shahosseini, 2011). Although the seasonal temperature variations shown in scenario B9 do not extend as deep as they do for the DTS data, further influences from anomalous seepage were anticipated; that is, the simulated seasonal temperature variations were expected to extend to greater depth after increased hydraulic conductivities were incorporated for anomalous seepage zones.

To quantitatively assess how well the simulated temperatures from scenario B9 agree with the DTS temperature data, weekly average temperature profiles as a function of depth were plotted at 35 day intervals from June 2016 to June 2017 (Figure 4-15).

The average root-mean-square (RMS) deviations of the simulated temperatures from the DTS temperatures were also calculated. The simulated temperature variations versus time plots show relatively large misfits, with the RMS averaging 1.0 to 2.5 °C above 20 m depth, while the average RMS values below 20 m depth are smaller than 0.5 °C. The RMS deviation over all depths over the course of the year is about 1.34 °C. The temperature deviations during winter (Dec. to May) are mainly due to the temperature anomalies that existed in the DTS data at the shallower depths. Better fits were expected to be achieved following the simulation of anomalous seepage to be discussed in Chapter 5.

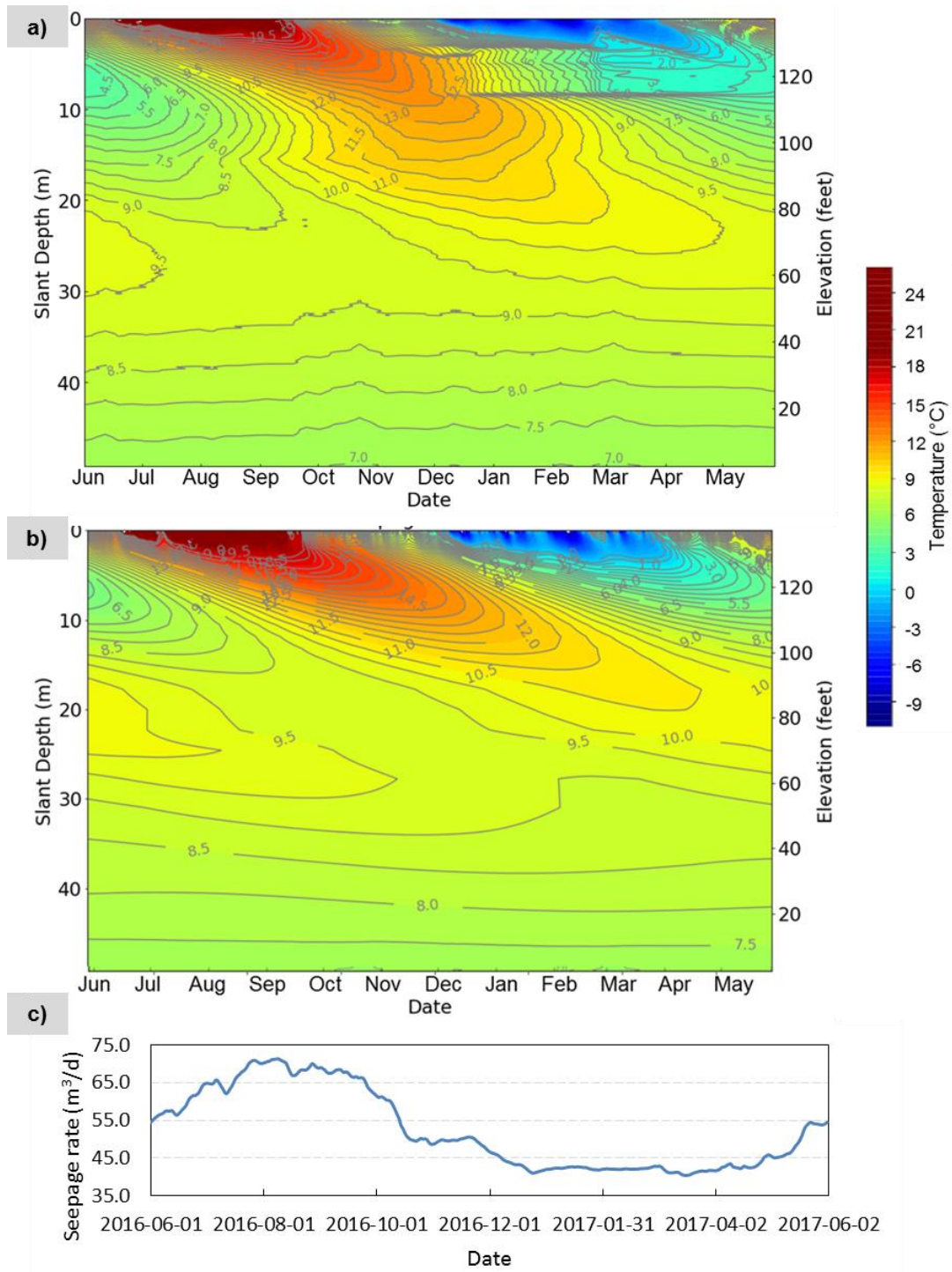


Figure 4-14: Temperature variations versus time plots for a) DTS data and b) scenario B9, as well as c) seepage rate versus time for scenario B9.

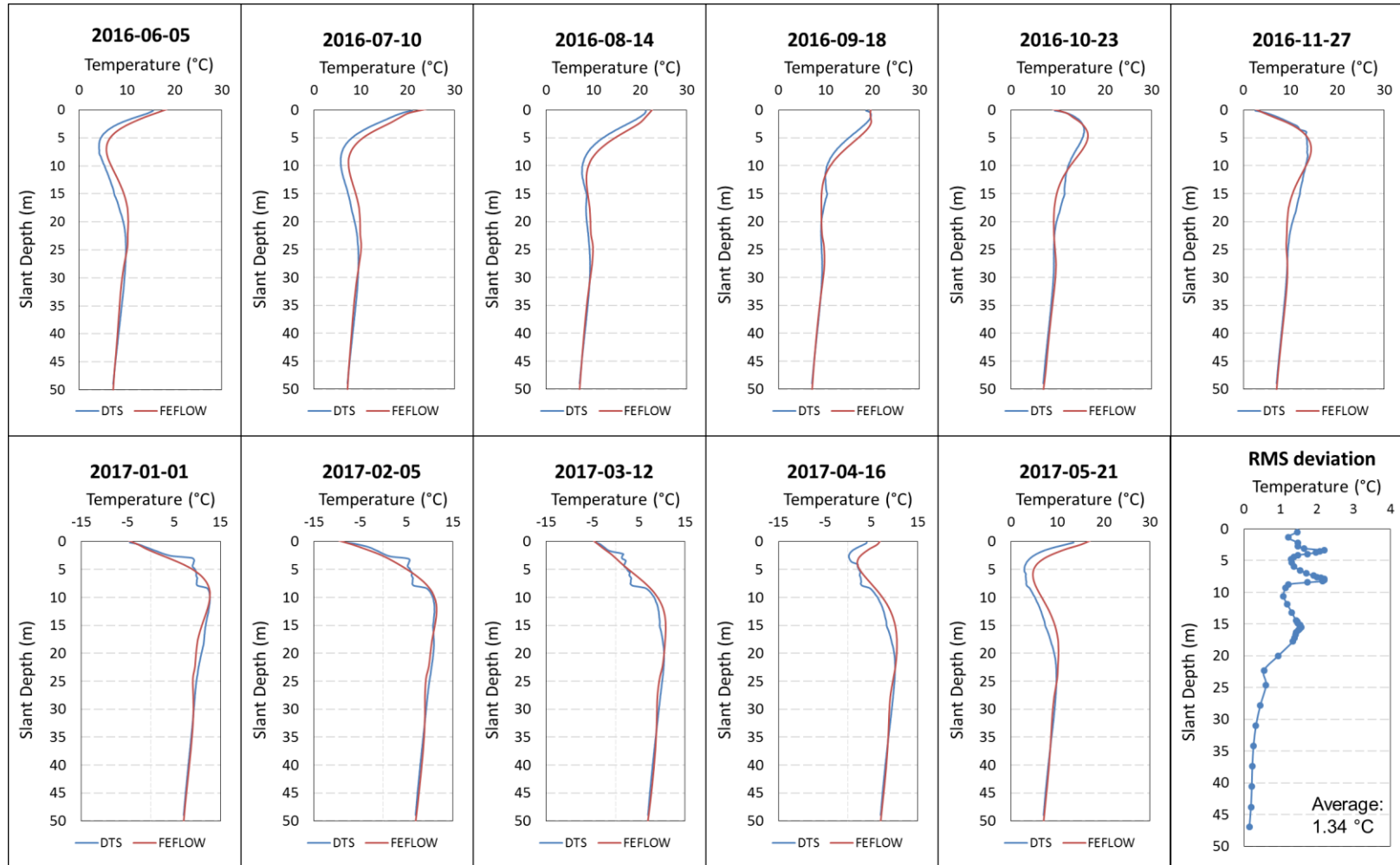


Figure 4-15: Comparisons of weekly average DTS temperature profiles (in blue) to the simulated bulk seepage temperature profile (in red) for scenario B9 at intervals of 35 days along with annual average RMS deviation as a function of depth. These temperature profiles were determined at borehole SEPI-3 (Figure 2-2).

## **Chapter 5 : Numerical simulations for anomalous seepage analysis**

### **5.1 Introduction**

The main purpose of this chapter is to simulate anomalous seepage near the dam/concrete interface, with attempts to reproduce the temperature anomalies observed at elevation 113' to 120-129' (slant depth 8.9 m to 6.3-3.1 m) and at elevation 95' (slant depth 15.5 m) (Figure 2-5) in the DTS data.

A simplified heat transport model, which was effectively 2D, was first developed to investigate how close a seepage zone would have to be to an instrumented borehole in order to generate the high temperature gradients observed at the top and the bottom of the shallow temperature anomaly. These simulations represented limiting cases, with constant temperatures assumed for an anomalously cold seepage zone and surrounding materials. Therefore, with a given borehole to seepage zone separation, the maximal steady state temperature anomalies and gradients at the boundaries of the seepage zone could be estimated.

Secondly, the 3D dam/concrete model developed in Chapter 4 was modified for anomalous seepage simulations. The effects of the hydraulic conductivity, location and geometry of the anomalous seepage zone on the simulated temperature distributions and the seepage rates were analyzed through several numerical simulations. The computed seepage rates represent the total outflow from the domain and were determined along the downstream slope of the dam.

## 5.2 Simplified model for temperature gradients investigation

The temperature versus depth profiles for borehole SEPI-3, and the corresponding temperature gradient versus depth profiles from November 2016 to March 2017, during which the shallow temperature anomaly was strongest, are presented in Figure 5-1. The strongest temperature gradients near the upper and lower boundaries of the shallow temperature anomaly were about  $14.7\text{ }^{\circ}\text{C}/\text{m}$  in January and  $7.9\text{ }^{\circ}\text{C}/\text{m}$  in March, respectively, which were much higher than the other locations along the borehole where temperature gradients were around  $0\text{ }^{\circ}\text{C}/\text{m}$ .

To investigate whether seepage along the dam/concrete interface could generate such strong temperature gradients, a simplified model (Figure 5-2) was used to represent the concrete segment, with a discrete interval along the dam/concrete interface held at a constant temperature.

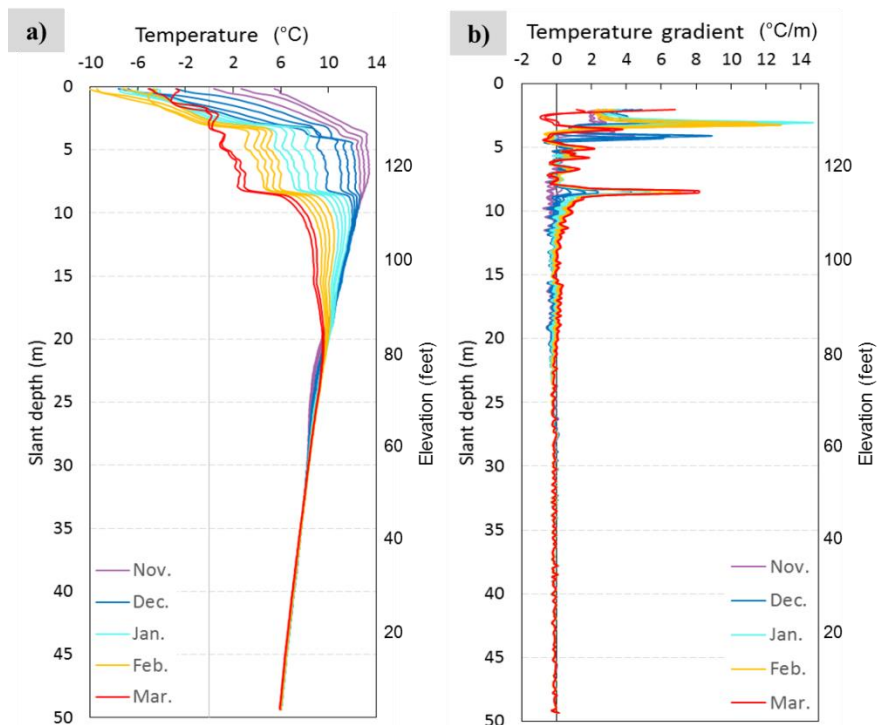


Figure 5-1: Weekly average temperature versus depth (a) and temperature gradient versus depth (b) profiles for November 2016 to March 2017.

### 5.2.1 *Simulation descriptions*

The simplified model domain, measuring 50 m by 50 m in the vertical section and 6 m in thickness (Figure 5-2), was discretized into a finite element grid consisting of 54,020 triangular elements, 30,294 nodes, and 10 layers. The thickness of the layers varied from 0.1 m to 2.4 m. The first slice of the domain represented the dam/concrete interface while the last slice represented the outer SEP concrete wall. The entire model domain was assigned the same thermal properties as used for concrete in the bulk seepage simulation in scenario B9 (Table 4-2). An interface zone of colder temperature was simulated on the first slice, located between 20 m and 30 m depth, with mesh refinement around this interval. The nodal observation points (representing temperature measurement points within the borehole) were located along a vertical line in the middle of the section, with the separation distance from the interface varying from 0.1 m to 0.6 m.

Only thermal conduction was considered in this model. A spatially uniform temperature of 10 °C was adopted as the initial conditions. The total simulation time was 200 days with an initial time step of 0.001 day.

A constant temperature of 0 °C (Dirichlet boundary condition), which represents the coldest headpond water temperature that would be expected, was assigned to the interface interval between 20 m and 30 m depth to represent an anomalously cool water seepage zone. A constant temperature of 10 °C, representing the average temperature that would be expected in January at the bottom of the shallow temperature anomaly (elevation 113') according to the bulk seepage simulations (Figure 4-15), was assigned

to the remaining interface and outer boundary nodes. The outer SEP concrete wall (last slice) was assigned a constant temperature of 10 °C (Case 1) or 0 °C (Case 2).

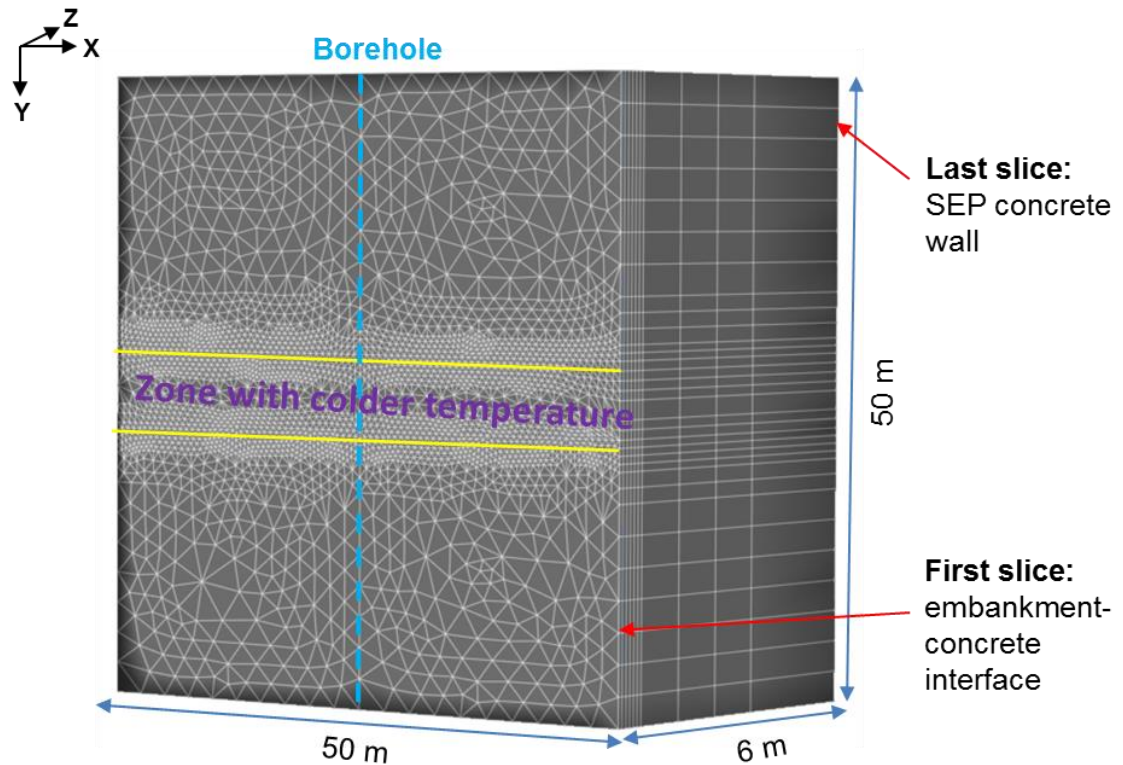


Figure 5-2: 3D geometry and meshing of the simplified cubic model. The  $z$  direction is magnified five times for easier viewing of the layers.

### 5.2.2 Results and discussions

It required approximately 60 days of simulation time for the temperature distributions to reach steady state. The simulated temperature versus depth profiles on the last time step of the simulation (200 days), and the corresponding gradient versus depth profiles, for Case 1 and Case 2 with borehole-interface separation varying from 0.1 m to 0.6 m, are depicted in Figure 5-3.

Comparing the results for Case 1 and 2 shows that the simulated temperatures along the borehole exhibit some dependence on the temperature assigned to the outer SEP concrete wall, while the simulated temperature gradients are insensitive to that boundary condition. The largest simulated temperature anomalies (i.e. difference between the temperatures within the seepage zone and the nearby temperatures along the borehole) in both cases vary from about 8.6 °C to 9.8 °C. The strongest temperature gradients vary from 4.5 °C /m to 12.5 °C /m.

The results indicate that the strongest DTS temperature gradient recorded at the upper boundary (14.7 °C/m) of the shallow temperature anomaly cannot be reproduced even for a borehole-interface separation as small as 0.1 m. However, the strongest DTS temperature gradient at the lower boundary (7.9 °C/m) could theoretically be achieved with a borehole-interface separation of 0.3 m or less. The vertical section in Appendix E, which shows the interpreted position of the dam/concrete interface relative to the planned position of the DTS SEPI-3 borehole, indicates that the borehole-interface separation is possibly as small as 0.3 m for the upper part of the borehole where the shallow temperature anomaly is present. This implies that concentrated water seepage along the dam/concrete interface could be a viable explanation for the strong temperature gradients at the bottom of the shallow DTS temperature anomaly.

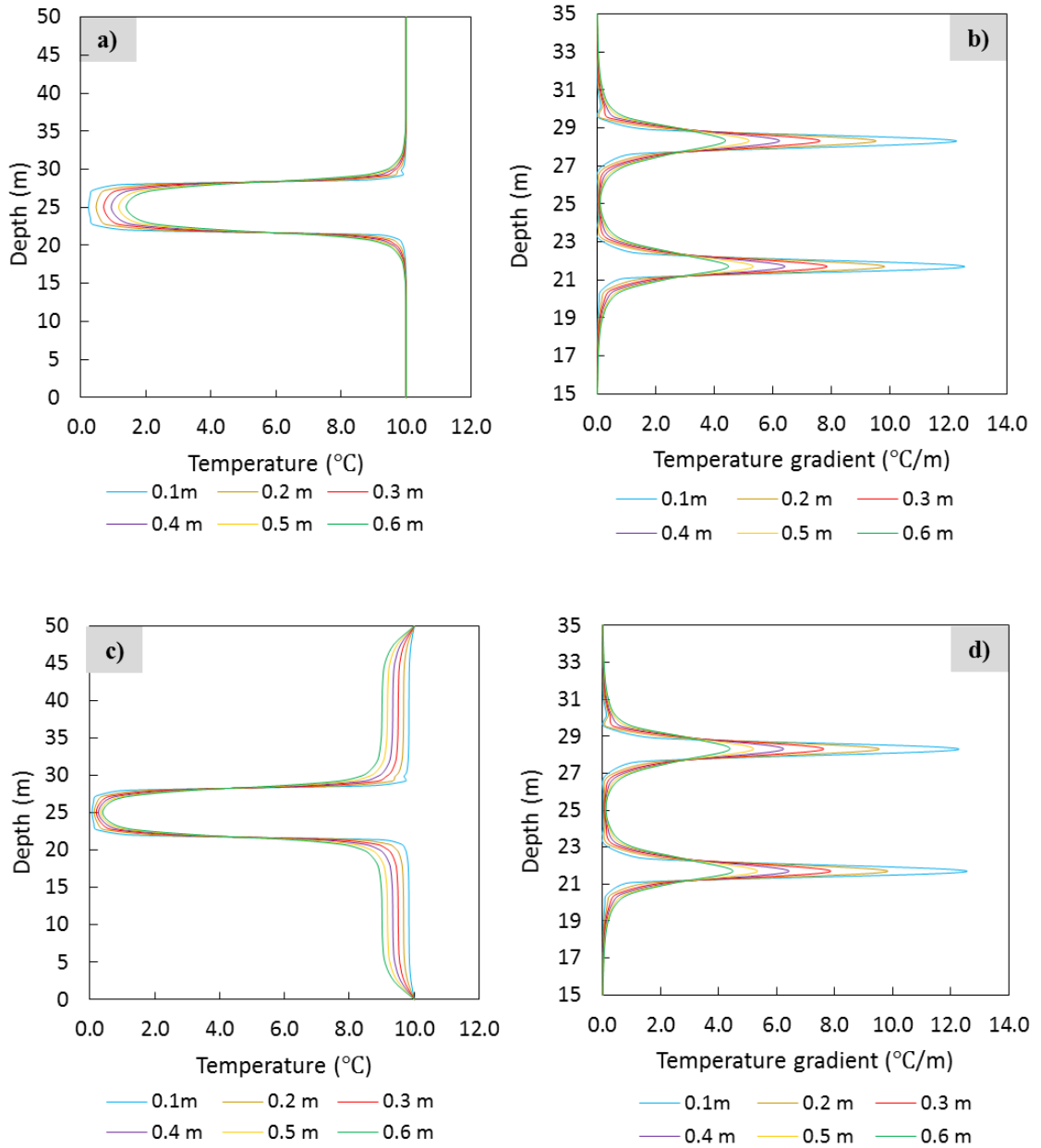


Figure 5-3: Simulated temperature versus depth and temperature gradient versus depth profiles for Case 1 (a, b) and Case 2 (c, d) with borehole-interface separations varying from 0.1 m to 0.6 m.

### 5.3 Simulation of the shallow temperature anomaly

The 3D dam/concrete model constructed in Chapter 4 was iteratively modified for anomalous seepage simulations which, unlike those presented in Section 5.2, include the direct simulation of water seepage. In the modified models, anomalous seepage was simulated: a) in the concrete surrounding the DTS borehole, b) along the dam/concrete interface, and c) both locations simultaneously. The simulated temperatures and hydraulic heads on the last simulation day (May 31, 2017) of scenario B9 (bulk seepage; Section 4.4) were adopted as the initial conditions, with cyclic boundary conditions imposed for a total simulation time of two years. The results from the final year of these two-year simulations were adopted for analysis. The thermal-hydraulic properties for the anomalous seepage zone (Table 5-1) were derived from the study of Shija and MacQuarrie (2015). The hydraulic conductivity of the seepage zone was varied from  $5.0 \times 10^{-5}$  m/s to  $1.0 \times 10^{-3}$  m/s, which is 200 to 4000 times larger than that of the clay till core ( $2.5 \times 10^{-7}$  m/s). All the other material property values remained the same as those in scenario B9.

Figure 5-4 illustrates the location and the geometries of the simulated seepage zones. Three characteristics of the simulated seepage zone were analyzed in each case: hydraulic conductivity, height in the vertical direction (**y** direction), and horizontal extent in the longitudinal direction (**z** direction). As the nodal elevations of each layer are not uniform and deformed layers are included in the 3D model, the horizontal extent of the simulated seepage zone refers to the distance measured in the **z** direction from the embankment-concrete interface and passing through the SEPI-3 borehole (Figure 5-4). The very thin seepage zones simulated in the concrete represent potential concrete

cracks. For all simulations, the separation distance between the embankment-concrete interface and the SEPI-3 borehole was 0.5 m.

Simulations including a shallow seepage zone will induce temperature anomalies both in summer and winter, as shown in the example in Appendix H. However, because the shallow temperature anomaly was only observed in the DTS data during the winter months, perhaps related to the effects of the AAR-induced concrete expansion as discussed in Section 2.2.4, time-varying thermal-hydraulic properties were applied to simulate the shallow temperature anomaly. Specifically, between December 1 and May 1, the properties provided in Table 5-1 were applied to the seepage zone, while for the remaining time, no seepage zone was simulated.

Table 5-1 Thermal-hydraulic parameters for anomalous seepage zone (Shija and MacQuarrie, 2015).

<b>Category</b>	<b>Parameter</b>	<b>Unit</b>	<b>Seepage zone</b>
Saturated flow	Hydraulic conductivity, $K$	$[\text{ms}^{-1}]$	$5.0 \times 10^{-5}$ to $1.0 \times 10^{-3}$
Unsaturated flow	Porosity, $\epsilon$	[-]	0.35
	Curve fitting parameter, $\alpha$	$[\text{m}^{-1}]$	2.8
	Curve fitting parameter, $n$	[-]	2.2
	Curve fitting parameter, $m$	[-]	0.55
	Curve fitting parameter, $\delta$	[-]	1.0
	Maximum saturation, $s_s$	[-]	1.0
	Residual saturation, $s_r$	[-]	0.08
Heat transport	Thermal conductivity of solid, $\lambda_s$	$[\text{Wm}^{-1}\text{K}^{-1}]$	3.9
	Volumetric heat capacity of solid, $C_s$	$[\text{MJm}^{-3}\text{K}^{-1}]$	2.21
	Longitudinal dispersivity, $\alpha_L$	[m]	1.0
	Transverse dispersivity, $\alpha_T$	[m]	0.1

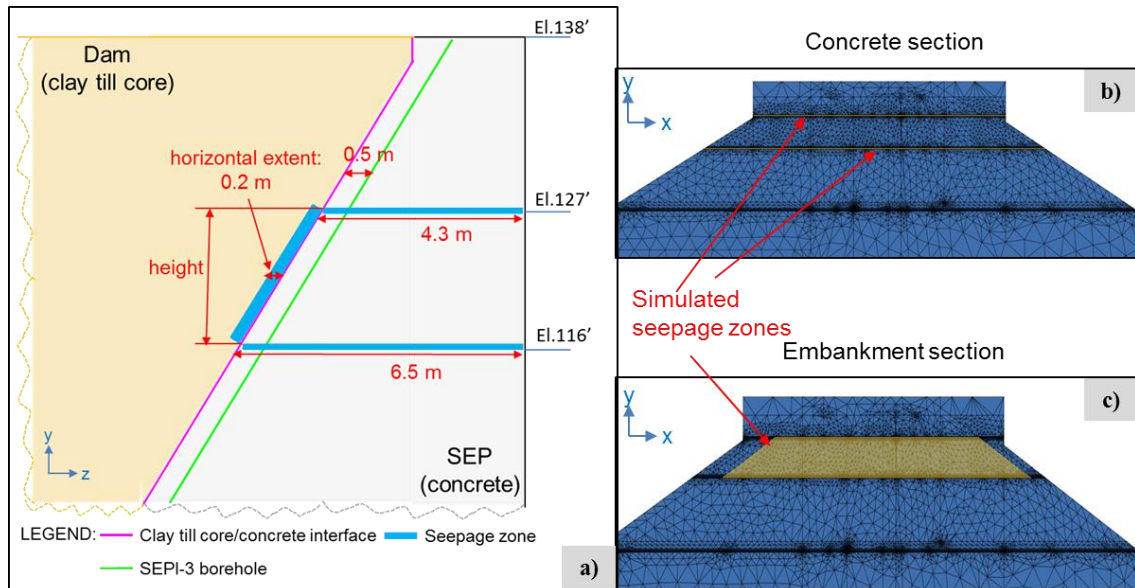


Figure 5-4: Longitudinal section of the dam/concrete structure through the clay till core-concrete interface and the SEPI-3 borehole (a) along with the slice views of the 3D model illustrating the location and geometry of the simulated seepage zone in the concrete (b) and embankment (c).

### 5.3.1 Case 1: Anomalous seepage zone in the concrete only

Five scenarios with seepage in the concrete only were simulated. All seepage zones simulated in the concrete extended from the upstream headpond boundary to the downstream boundary of the domain, but were assigned different heights, horizontal extents, and hydraulic conductivities (Table 5-2). The time series of daily average seepage rates for each scenario are shown in Figure 5-5. An example of the temperature variations with depth, for 66 nodes located 0.5 m from the inclined embankment-concrete interface (Figure 4-4), is shown in Figure 5-6 for scenario A1 for the final year of the simulation (results for scenarios A2 to A5 are presented in Appendix I).

Comparisons between the simulated temperatures and DTS temperatures, as presented in Section 4.4, are provided in Figure 5-7 and Figure 5-8; only the results from January to

March, during which the shallow temperature anomalies are most obvious, are presented. Plots of annual average RMS deviations as a function of depth are also included in Figures 5-7 and 5-8.

Table 5-2: Key parameter values for the concrete anomalous seepage simulations (A1 to A5) for the shallow temperature anomaly.

Scenario No.	A1	A2	A3	A4	A5
Hydraulic conductivity (m/s)	$4.6 \times 10^{-4}$	$4.6 \times 10^{-4}$	$4.6 \times 10^{-4}$	$4.6 \times 10^{-4}$	$1.0 \times 10^{-3}$
Horizontal extent (m)	4.3; 6.5	6.5	6.5	0.75	0.75
Related layer numbers	6 - 12	6 - 12	6 - 12	6 - 9	6 - 9
Height (m)	0.15	0.15	0.09	0.09	0.09
Slant depth range (m)	4.0 - 3.8 8.0 - 7.8	8.0 - 7.8	7.9 - 7.8	7.9 - 7.8	7.9 - 7.8
Elevation range (feet)	126.5 - 127 115.5 - 116	115.5 - 116	115.7 - 116	115.7 - 116	115.7 - 116

Note: two seepage zones were simulated in scenario A1 at different depths.

With anomalous seepage zones simulated only during the winter, an increase of the seepage rate can be observed from December to May for all five scenarios when compared to the results from the bulk seepage simulation (Figure 5-5). As expected, simulation A1, which had two seepage zones that extended through the entire concrete structure, produced the greatest increase in seepage. The temporal temperature results for scenario A1 (Figure 5-6) show that lower temperatures were induced within the anomalous seepage zones due to the increased water flow coming from the headpond, which had a lower temperature than that of the concrete during winter. Although large temperature gradients were generated near the simulated seepage zones for scenario A1, the weekly average temperature versus depth profiles in Figure 5-7 a) clearly show that the strong temperature gradients in the DTS data near slant depth 3.8 m are induced by

an abrupt temperature increase. Thus the simulated abrupt temperature decrease increased the misfit when compared to the observed DTS profile. Other simulations with a seepage zone simulated near slant depth of 3.8 m were also carried out to try to improve the fit between the simulated and DTS temperatures, through varying the hydraulic conductivity and geometry of the seepage zone, but neither of them could reproduce the observed abrupt temperature increase at that location.

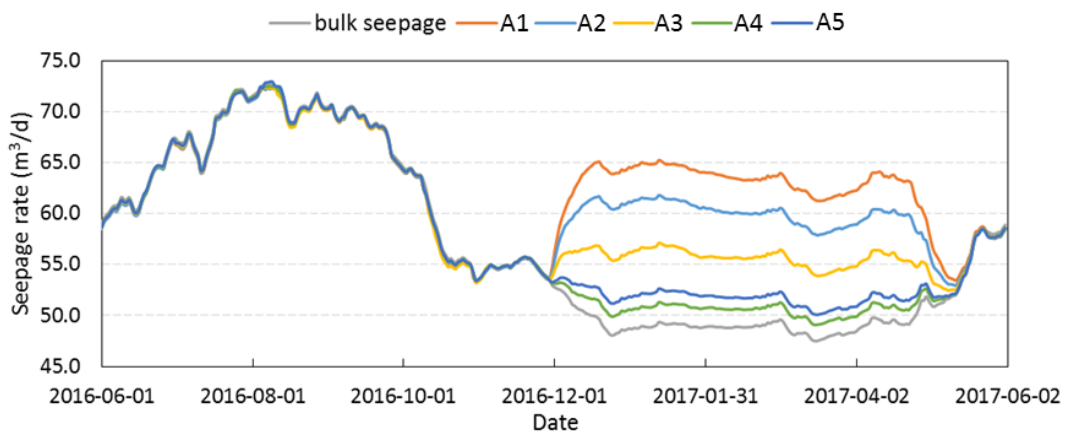


Figure 5-5: Seepage rate (daily average) versus time for scenarios A1 to A5 and B9 (bulk seepage).

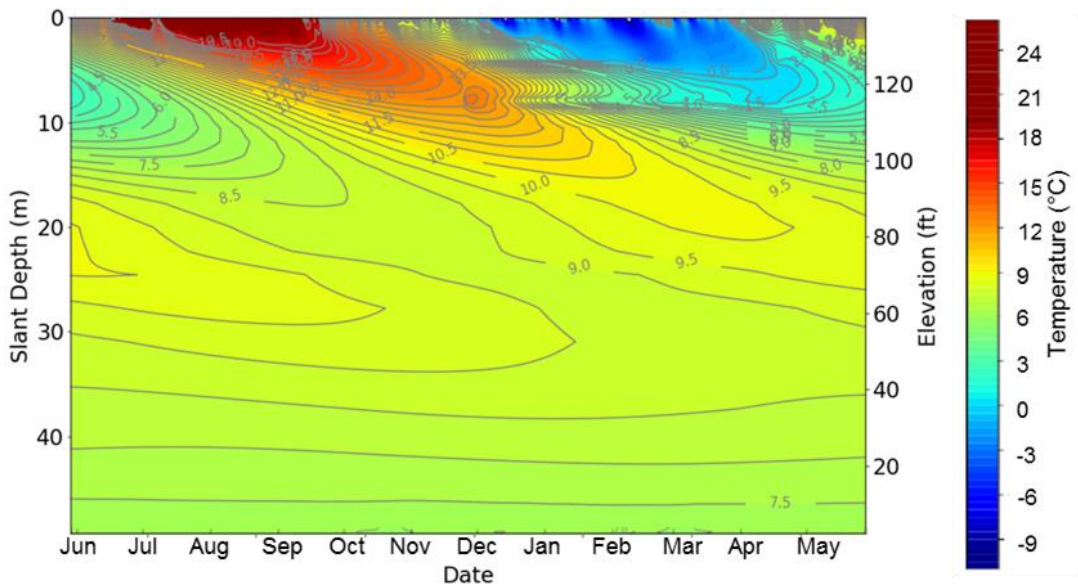


Figure 5-6: Simulated temperature variations versus time for scenario A1

Scenarios A2 to A5 focused on a single seepage zone that extended through the entire concrete structure at a slant depth of 7.9 m. A seepage zone with a horizontal extent penetrating the entire SEP concrete wall was simulated in scenarios A2 and A3 (Table 5-2). The reduced height of the seepage zone in scenario A3, compared to scenario A2, resulted in smaller seepage rates during December to May (Figure 5-5), thus the heat transported by convection was also reduced. As a result, the simulated temperature drop at a slant depth of 7.9 m in scenario A3 is smaller than that of scenario A2 (Figure 5-7 b) and c)). Scenario A3 provides a better fit to the DTS temperature results at this slant depth, but neither scenario is able to reproduce the full height of the near-constant temperature zone observed in the DTS data (i.e. between slant depth of 3.8 m and 8.0 m).

Comparisons between scenario A3 and A4 show that the reduction of the horizontal extent of the enhanced seepage zone from 6.5 m to 0.75 m will also decrease the seepage rate (Figure 5-5) and the resulting temperature drop in and around the seepage zone (Figure 5-7 c) and Figure 5-8 a)).

The influence of changing the hydraulic conductivity of the seepage zone can be seen through comparisons between scenarios A4 and A5. A higher seepage rate was obtained for scenario A5 than for scenario A4 (Figure 5-5), while a slightly larger temperature drop was simulated for scenario A5 within the seepage zone (i.e. slant depth of 7.9 m, Figure 5-8).

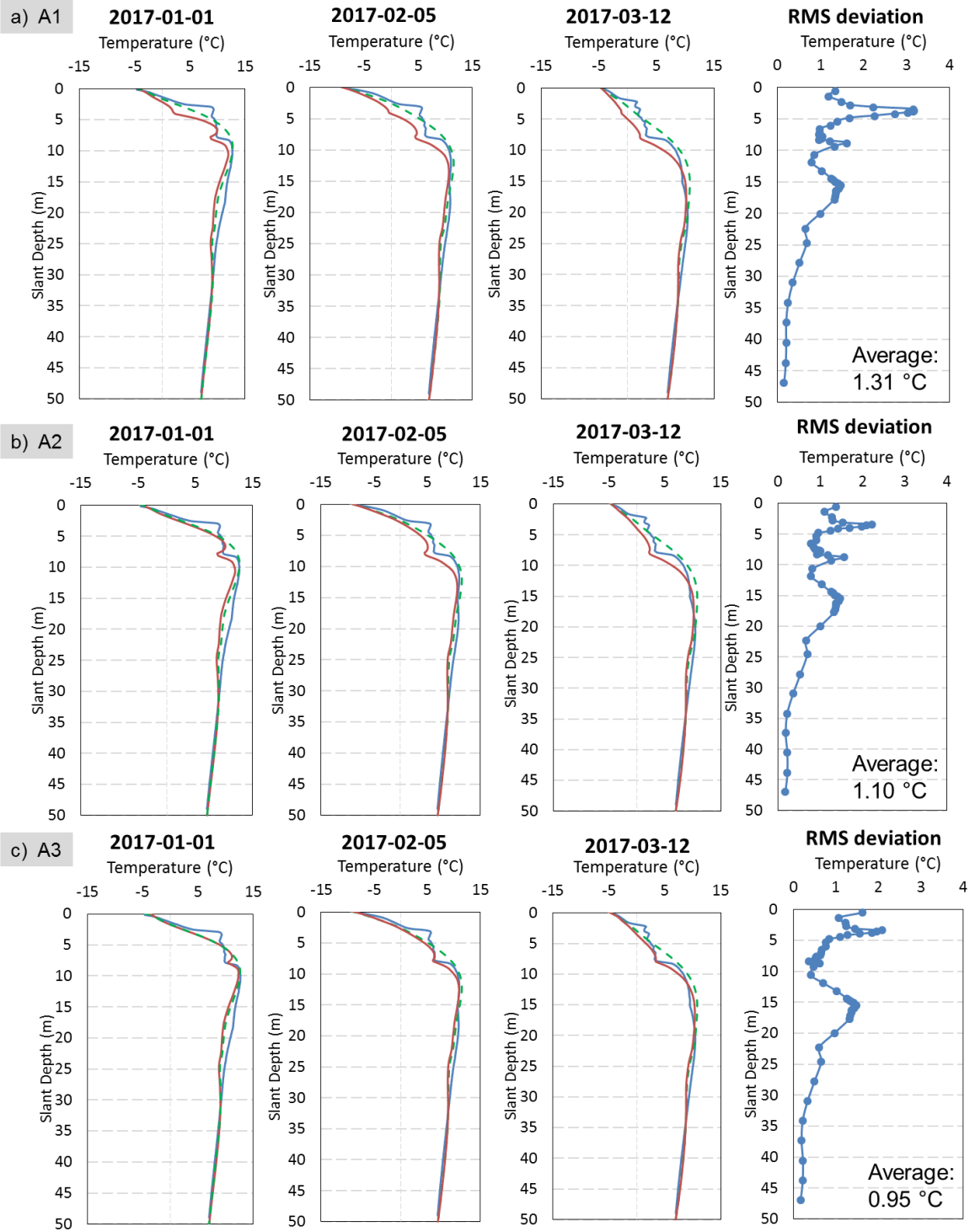


Figure 5-7: Comparisons of weekly average DTS temperature profiles (in blue) to the simulated anomalous temperature profile (in red) and bulk seepage profile (in dashed green) for January, February and March in 2017, along with annual average RMS deviation as a function of depth for scenarios a) A1, b) A2, and c) A3.

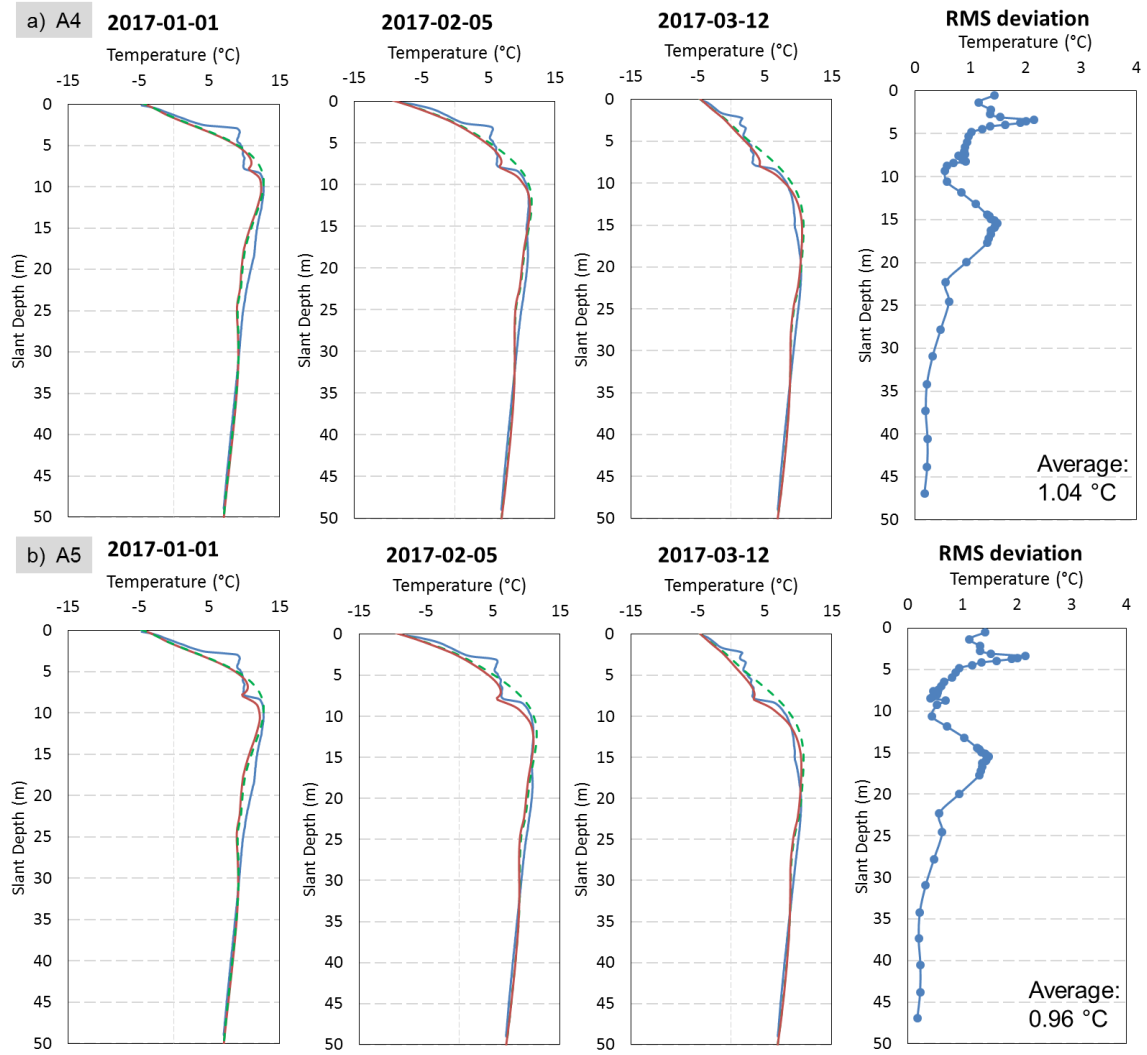


Figure 5-8: Comparisons of weekly average DTS temperature profiles (in blue) to the simulated anomalous temperature profile (in red) and bulk seepage profile (in dashed green) for January, February and March in 2017, along with annual average RMS deviation as a function of depth for scenarios a) A4 and b) A5.

Table 5-3 shows the annual average seepage rate, the increased seepage rate relative to the bulk seepage simulation (scenario B9) and the annual and spatial average RMS deviations of the simulated temperatures from the DTS data. It can be seen that the RMS values were decreased for all scenarios, when compared to the bulk seepage simulation. The lowest RMS value was obtained for scenario A3, which has an annual

average seepage rate of 59.7 m<sup>3</sup>/d. The simulated anomalous seepage rates are orders of magnitude lower than the reported values for leakage of between 0.1 m<sup>3</sup>/s – 0.36 m<sup>3</sup>/s (2.6 x 10<sup>4</sup> m<sup>3</sup>/d – 3.1 x 10<sup>4</sup> m<sup>3</sup>/d) from case studies at dams that have experienced internal erosion without or before breaching (Fell et al. 1992; Flores et al. 2011; Al-Ansari et al., 2017). However, the dam leakage in these case studies was visibly high, for example, the seepage rate of 3.1 x 10<sup>4</sup> m<sup>3</sup>/d in the Mosul Dam Iraq was determined from a spring that appeared on the downstream face of the dam (Al-Ansari et al., 2017).

Table 5-3: Annual average seepage rate, the increased seepage rate, and the annual and spatial average RMS deviations for scenarios A1 to A5.

Scenario No.	Seepage rate (annual average) m <sup>3</sup> /d	Increased seepage rate (relative to bulk seepage) m <sup>3</sup> /d	RMS deviations (annual average) °C
B9 (bulk)	57.1	-	1.34
A1	62.9	5.8	1.31
A2	61.5	4.4	1.10
A3	59.7	2.6	0.95
A4	57.7	0.6	1.04
A5	58.2	1.1	0.96

To summarize, a single discrete seepage zone within the concrete during December to May at an elevation of 116' (slant depth of 7.8 m) was simulated to induce an abrupt temperature drop at this location, thus resulting in higher temperature gradients around it. However, the vertical extent of the shallow temperature anomaly cannot be reproduced with a thin seepage zone simulated in the concrete only. The hydraulic conductivity and horizontal extent of the seepage zone have similar effects on the simulated temperature variations. Increasing the hydraulic conductivity, and the

cross-sectional area (height and thickness) of the seepage zone will both result in a higher seepage rate and temperature drop within the seepage zone.

The strong temperature gradient at the upper boundary (i.e. slant depth 3.8 m) of the shallow temperature anomaly observed in the DTS data cannot be reproduced using scenarios with seepage zones that extend from the upstream to the downstream face of the concrete SEP structure. The upper part of the shallow temperature anomaly is warmer than would be expected based on the bulk seepage simulation (Figure 5-7 and Figure 5-8); however, the simulated seepage zone within the concrete could only produce cooler temperature in this location during winter.

### 5.3.2 *Case 2: Anomalous seepage zone along the dam/concrete interface*

In this section, four modelling scenarios with seepage simulated along the interface (between the embankment and concrete), assumed to lie 0.5 m away from the borehole are presented. Instead of simulating a thin seepage zone, or zones, as was done for the concrete, the height of the seepage zone along the interface ranges from 2.9 m to 3.5 m. Unlike the convective heat transfer associated with seepage through a crack in the concrete that intersects the borehole, increased seepage along the interface can only influence the temperature at the borehole through heat conduction because it is assumed that homogeneous concrete separates the interface and borehole.

The hydraulic conductivities and geometries of the four simulated seepage zones are presented in Table 5-4. The anisotropy ratio assigned to the simulated seepage zone is 2.5, which is the same as the value applied to the other embankment materials. The

seepage zones simulated in scenarios A6, A8 and A9 extended from the upstream to downstream, excluding the riprap, as shown in Figure 5-4. In contrast, the simulated seepage zone in scenario A7 only penetrated through the core and the filter. The seepage zones in each scenario were only simulated during the winter.

Table 5-4: Key parameter values for the interface anomalous seepage simulations (A6 to A9) for the shallow temperature anomaly.

Scenario No.	A6	A7	A8	A9
$K_{xx}$ (m/s)	$4.6 \times 10^{-4}$	$5.0 \times 10^{-5}$	$4.6 \times 10^{-4}$	$4.6 \times 10^{-4}$
$K_{yy}$ (m/s)	$1.84 \times 10^{-4}$	$2.0 \times 10^{-5}$	$1.84 \times 10^{-4}$	$1.84 \times 10^{-4}$
Horizontal extent (m)	0.2	0.2	0.4	0.2
Related layer numbers	4 - 5	4 - 5	2 - 5	4 - 5
Height (m)	3.5	3.5	2.9	2.9
Slant depth range (m)	8.0 - 3.8	8.0 - 3.8	7.6 - 4.2	7.6 - 4.2
Elevation range (feet)	115.5 - 127	115.5 - 127	116.5 - 126	116.5 - 126

The resulting contour plots of temperature variations versus time and seepage rate time series are presented in Figure 5-9 and Figure 5-10, respectively. Comparisons between the simulated and measured temperature profiles are presented in Figure 5-11 and Figure 5-12. The annual average seepage rate, the increased seepage rate relative to the bulk seepage simulation (scenario B9), and the annual and spatial average RMS temperature misfits for each scenario are listed in Table 5-5.

With the exception of scenario A7, all the simulations produced a temperature drop of varying magnitude within the simulated seepage zone. In the case of scenario A7, the influence of the concentrated seepage on the temperature variations versus time profile (Figure 5-9) is not obvious due to the small hydraulic conductivity and volume of the seepage zone.

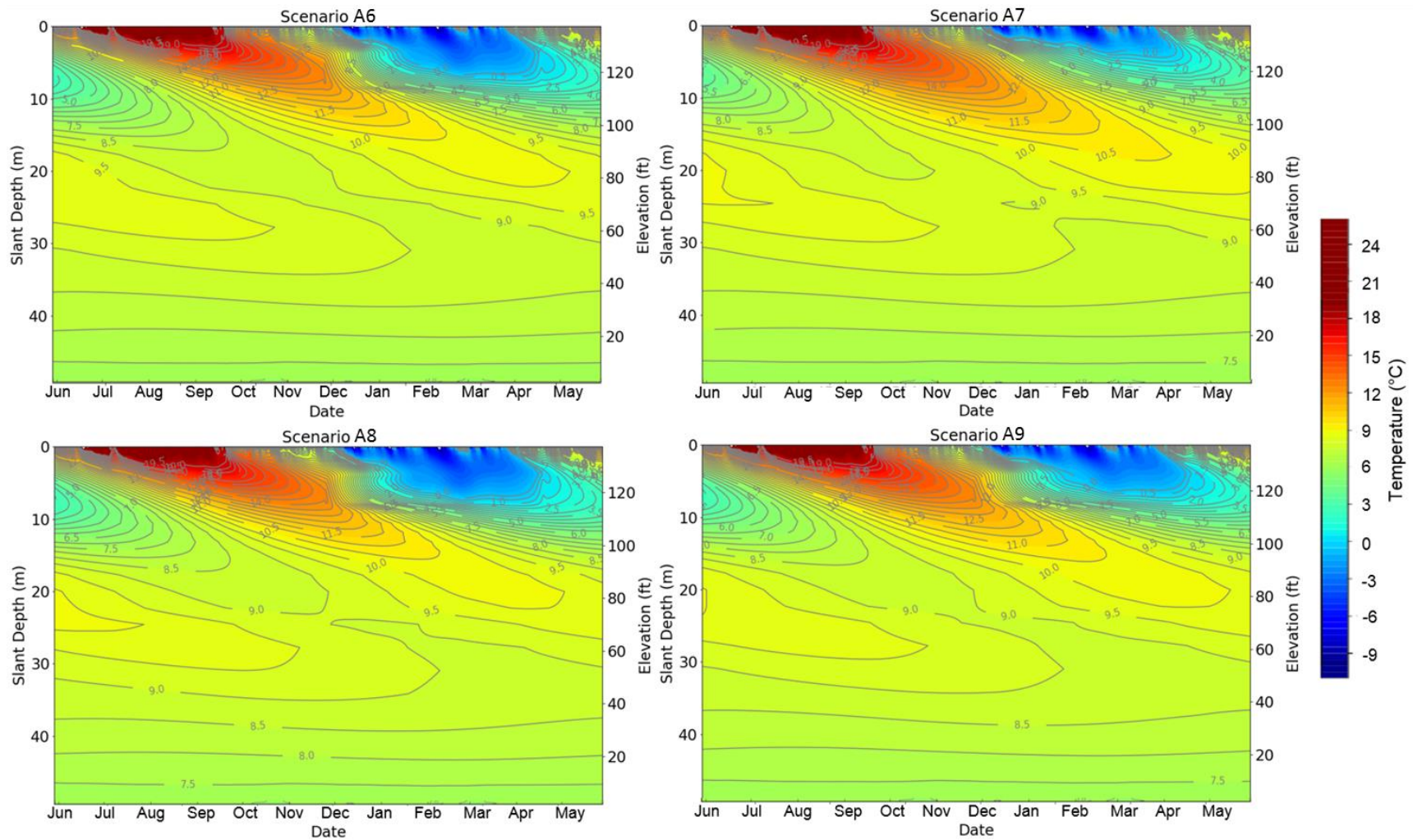


Figure 5-9: Simulated temperature variations versus time for scenarios A6 to A9.

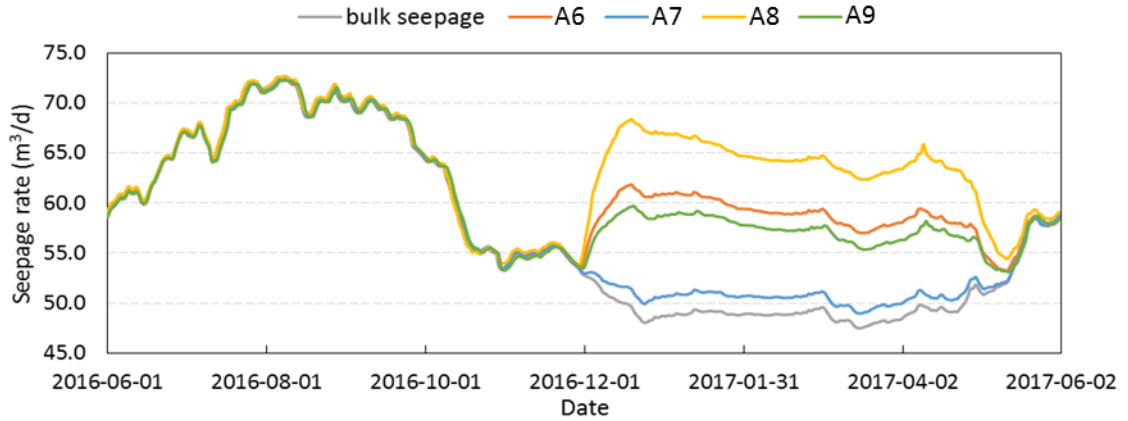


Figure 5-10: Seepage rate (daily average) versus time for scenarios A6 to A9 and B9 (bulk seepage).

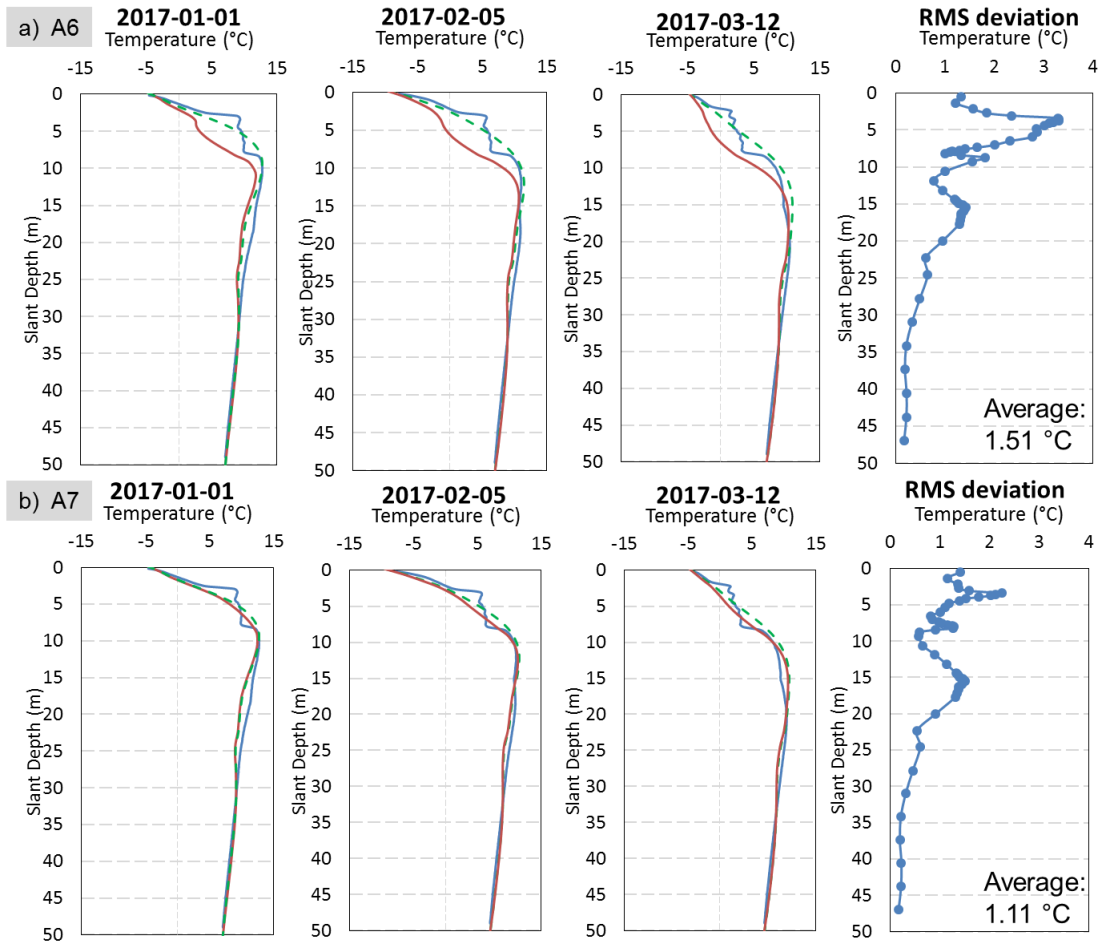


Figure 5-11: Comparisons of weekly average DTS temperature profiles (in blue) to the simulated anomalous temperature profile (in red) and bulk seepage profile (in dashed green) for January, February and March in 2017, along with annual average RMS deviation as a function of depth for scenarios a) A6 and b) A7.

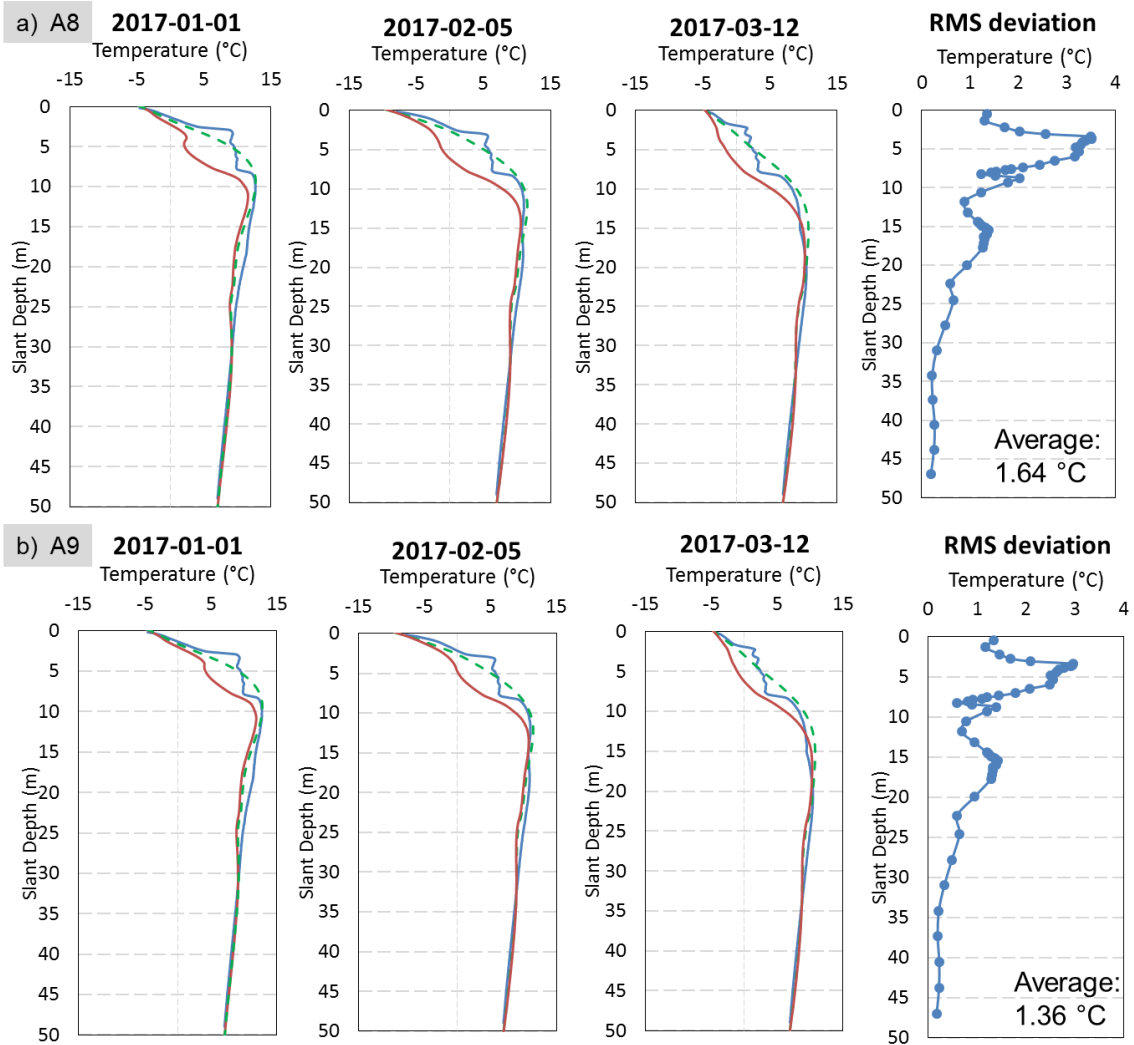


Figure 5-12: Comparisons of weekly average DTS temperature profiles (in blue) to the simulated anomalous temperature profile (in red) and bulk seepage profile (in dashed green) for January, February and March in 2017, along with annual average RMS deviation as a function of depth for scenarios a) A8 and b) A9.

Table 5-5: Annual average seepage rate, the increased seepage rate, and the annual and spatial average RMS deviations for scenarios A6 to A9.

Scenario No.	Seepage rate (annual average) m <sup>3</sup> /d	Increased seepage rate (relative to bulk seepage) m <sup>3</sup> /d	RMS deviations (annual average) °C
B9 (bulk)	57.1	-	1.34
A6	61.2	4.1	1.51
A7	57.7	0.6	1.11
A8	63.8	6.7	1.64
A9	60.6	3.5	1.36

Comparisons between scenarios A6, A8 and A9 reveal that the temperature drop within the seepage zone and the simulated seepage rate increase with an increase in the cross-sectional area of the seepage zone (Figure 5-10, Figure 5-11 a) and Figure 5-12). However, none of the simulations could replicate the strong observed DTS temperature gradients at the boundaries of the simulated seepage zone. As expected, the vertical extent of the simulated seepage zone determines the vertical extent of the zone of temperature drop (Figure 5-9). Due to the larger heights of the seepage zones simulated along the interface, higher seepage rates and temperature drop within the seepage zones were induced when compared with the case of seepage within the concrete alone (Figure 5-10, Figure 5-11 and Figure 5-12). Thus, seepage zones simulated along the interface increased the temperature deviations when compared to the bulk seepage simulation, except for scenario A7, which did not have any significant influence on the simulated temperature (Table 5-5).

A seepage zone simulated along the dam/concrete interface can reproduce the vertical extent of the shallow anomaly; however, the resulting anomalous temperature zone is too cold, and the strong temperature gradients at the upper and lower boundaries

of this zone are not replicated. The latter observation is consistent with the conclusions obtained in Section 5.2.

### 5.3.3 Case 3: Anomalous seepage zone in concrete and along interface

Scenario A10 was formed by combining the concrete seepage scenario A2 with the interface seepage scenario A6. The increase in daily and annual average seepage rate (Figure 5-13 and Table 5-6), compared to the bulk seepage case, is consistent with the sum of the individual increases associated with scenarios A2 and A6. The strong DTS gradients at the upper boundaries of the shallow temperature anomaly could not be reproduced using scenario A10 (Figure 5-14). The simulation produced strong temperature gradients at the lower boundaries of the shallow seepage zone and the height of the near-constant temperature zone was similar to that observed in the DTS data (Figures 5-14 and 5-15). However, the increased seepage flow in scenario A10 made the anomalous zone much colder than the DTS data (Figure 5-14).

Table 5-6: Annual average seepage rate, the increased seepage rate, and the annual and spatial average RMS deviations for scenarios A2, A6 and A10.

Scenario No.	Seepage rate (annual average) m <sup>3</sup> /d	Increased seepage rate (relative to bulk seepage) m <sup>3</sup> /d	RMS deviations (annual average) °C
B9 (bulk)	57.1	0	1.34
A2	61.5	4.4	1.10
A6	61.2	4.1	1.51
A10	65.6	8.5	1.95

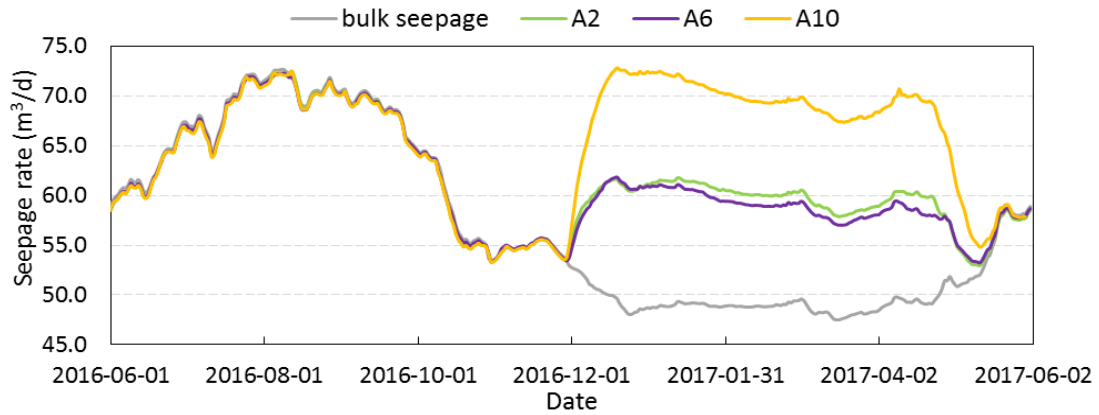


Figure 5-13: Seepage rate versus time for scenarios A2, A6 and A10 and B9 (bulk seepage).

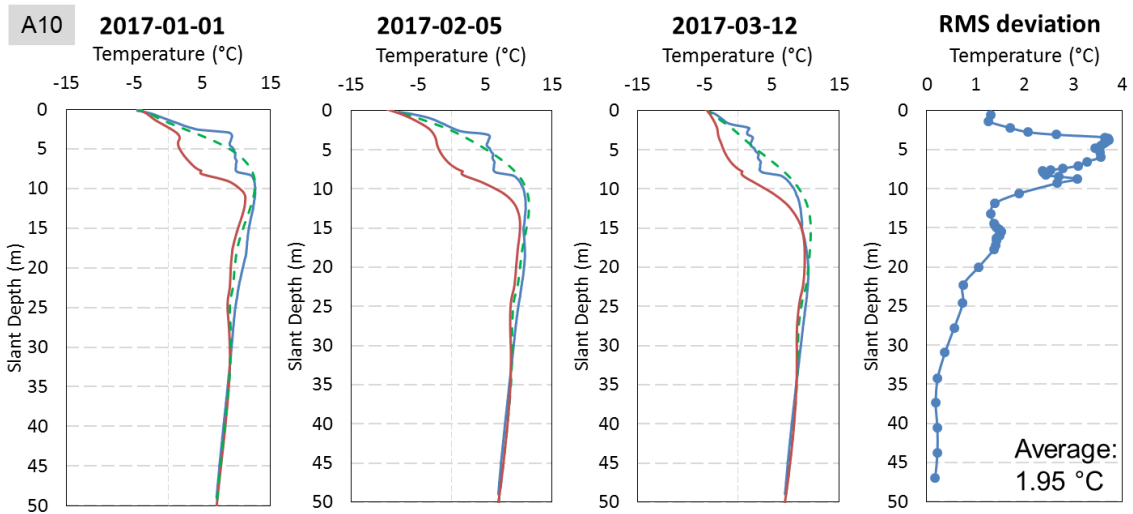


Figure 5-14: Comparisons of weekly average DTS temperature profiles (in blue) to the simulated anomalous temperature profile (in red) and bulk seepage profile (in dashed green) for January, February and March in 2017, along with annual average RMS deviation as a function of depth for scenario A10.

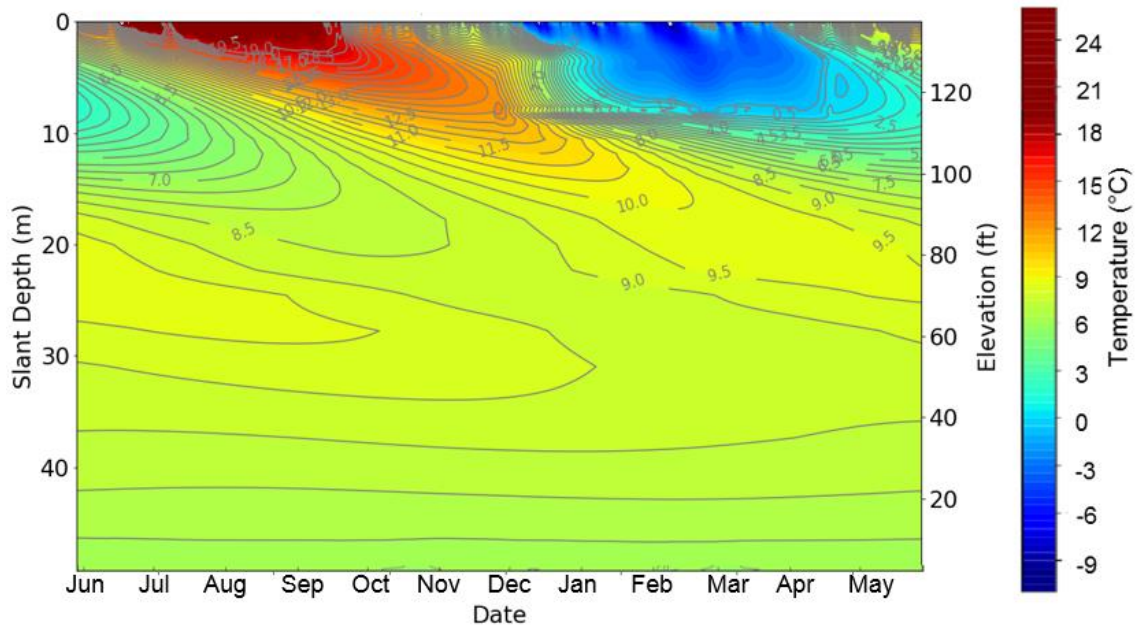


Figure 5-15: Simulated temperature variations versus time for scenario A10.

#### 5.4 Simulation of the temperature anomaly at elevation 95'

The deeper, more subtle temperature anomaly observed at elevation 95' (slant depth 15.5 m) was investigated with several simulations. All of the scenarios were modified versions of scenario A3, which had a single seepage zone in the concrete at elevation 115.7' (slant depth of 7.9 m), and yielded the lowest average RMS deviation among the simulations of the shallow temperature anomaly. The results show that the hydraulic conductivity, height and horizontal extent of a seepage zone at elevation 95' influence temperature variations along the borehole in a manner that is similar to what was demonstrated in Section 5.3. Thus, only selected representative scenarios are presented here.

Table 5-7: Key parameter values for the anomalous seepage simulations (A11 to A14) for the deep temperature anomaly.

Scenario No.	A11	A12	A13	A14
Location of the seepage zone	concrete	interface	concrete	interface
Hydraulic conductivity (m/s)	$5.0 \times 10^{-5}$	$1.0 \times 10^{-4}$	$5.0 \times 10^{-5}$	$1.0 \times 10^{-4}$
Horizontal extent (m)	10.7	0.2	10.7	0.2
Related layer numbers	6 to 12	4 to 5	6 to 12	4 to 5
Height (m)	0.15	0.3	0.15	0.3
Slant depth range (m)	15.5 – 15.3	15.5 – 15.1	15.5 – 15.3	15.5 – 15.1
Elevation range (feet)	95 - 95.5	95 - 96	95 - 95.5	95 - 96

Note: All the scenarios described above were combined with scenario A3 (Table 5-2). In scenarios A13 and A14, the hydraulic conductivity of the core were both increased to  $3.0 \times 10^{-7}$  m/s and the anisotropy ratio was decreased to 2.0 for the entire model domain.

In scenarios A11 and A13 (Table 5-7), the seepage zone was assumed to occur in the concrete only, while in scenarios A12 and A14, it was located along the interface only. The hydraulic conductivity of the core in scenarios A13 and A14 was increased slightly from  $2.5 \times 10^{-7}$  m/s to  $3.0 \times 10^{-7}$  m/s. In addition, the anisotropy ratio for the entire embankment domain excluding riprap was reduced from 4.0 (core and filter) and 3.5 (shells) to 2.0. The new bulk seepage simulation related to these changes was denoted as scenario B10. The purpose for the parameter changes in scenarios A13 and A14 was to investigate whether varying the hydraulic conductivity of the embankment would influence the increased seepage rate associated with the addition of seepage zones, and the intensity of the induced temperature anomaly. More details about the parameter values assigned to the seepage zones in each scenario, which were simulated for an entire year, are listed in Table 5-7.

A cross-section showing the simulated temperature distribution within the concrete, 0.5 m from its interface with the embankment, for scenario A11 on January 1 is shown in Figure 5-16. The location of the two discrete zones with higher seepage can be clearly identified by the anomalous lower and higher temperatures at elevation 116' and 95', respectively. The modelled saturation line was observed to extend to the downstream direction at the shallow temperature anomaly.

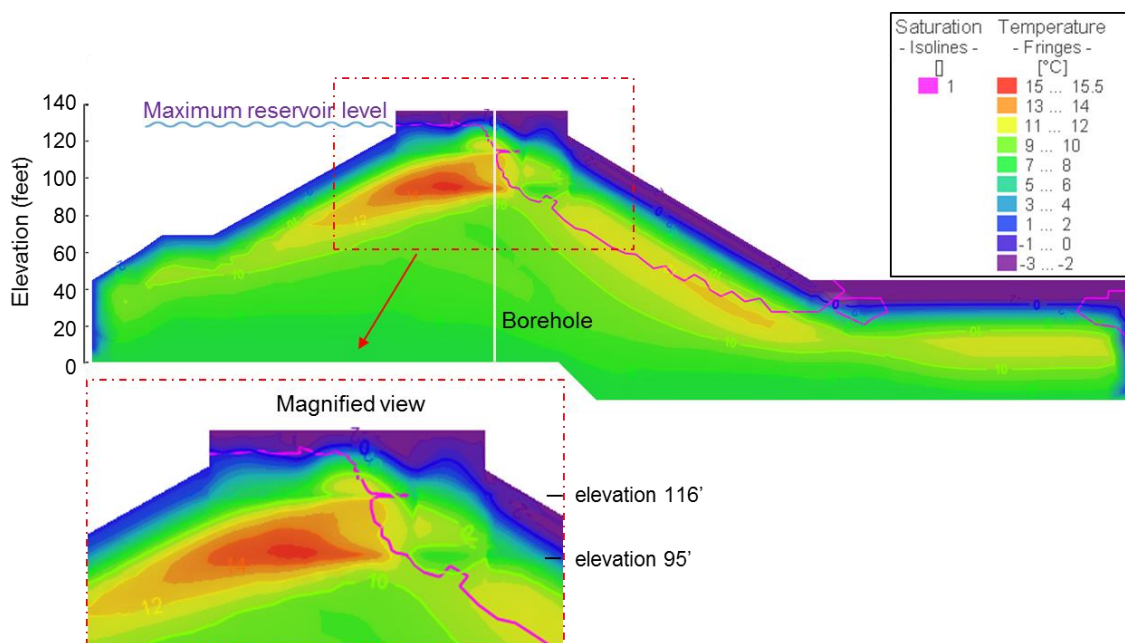


Figure 5-16: Simulated temperature distribution within the concrete, 0.5 m from its interface with the embankment, for scenario A11 on January 1, 2017.

The 0.15 m height seepage zone simulated in the concrete (scenarios A11 and A13) at elevation 95' induces a narrow temperature peak similar to that measured, except that it is present throughout the entire year (Figure 5-17), suggesting that opening of that crack in the concrete (presumed to lie along a concrete pour lift) may also be seasonally controlled. Seepage zones simulated along the interface (scenario A12 and A14) can also induce a narrow temperature peak, but the total height of the area

influenced by the anomalous seepage is much smaller than that in the concrete. It can therefore be surmised that the deep temperature anomaly is more likely to be related to seepage within the concrete.

The temperature profile comparisons between the simulated temperatures and DTS data for all four seepage scenarios are shown in Figure 5-18 and Figure 5-19 for August, September and October – the time of year during which the deep temperature anomaly was most obvious in the DTS data. The observed temperatures at elevation 95' (slant depth of 15.5 m) during that time were anomalously warm; however, simulated temperatures were anomalously cold. Thus, the misfit with the DTS temperature profiles was increased when compared to scenario A3 (simulation of the shallow potential seepage zone alone), especially for scenarios A11 and A13, in which the seepage zones were simulated in the concrete. Recent consideration of the deep temperature anomaly has led to another hypothesis for the origin of this anomaly, involving seepage along a concrete fracture that is effectively hydraulically isolated from the embankment. This is discussed further in Section 5.5.2 below.

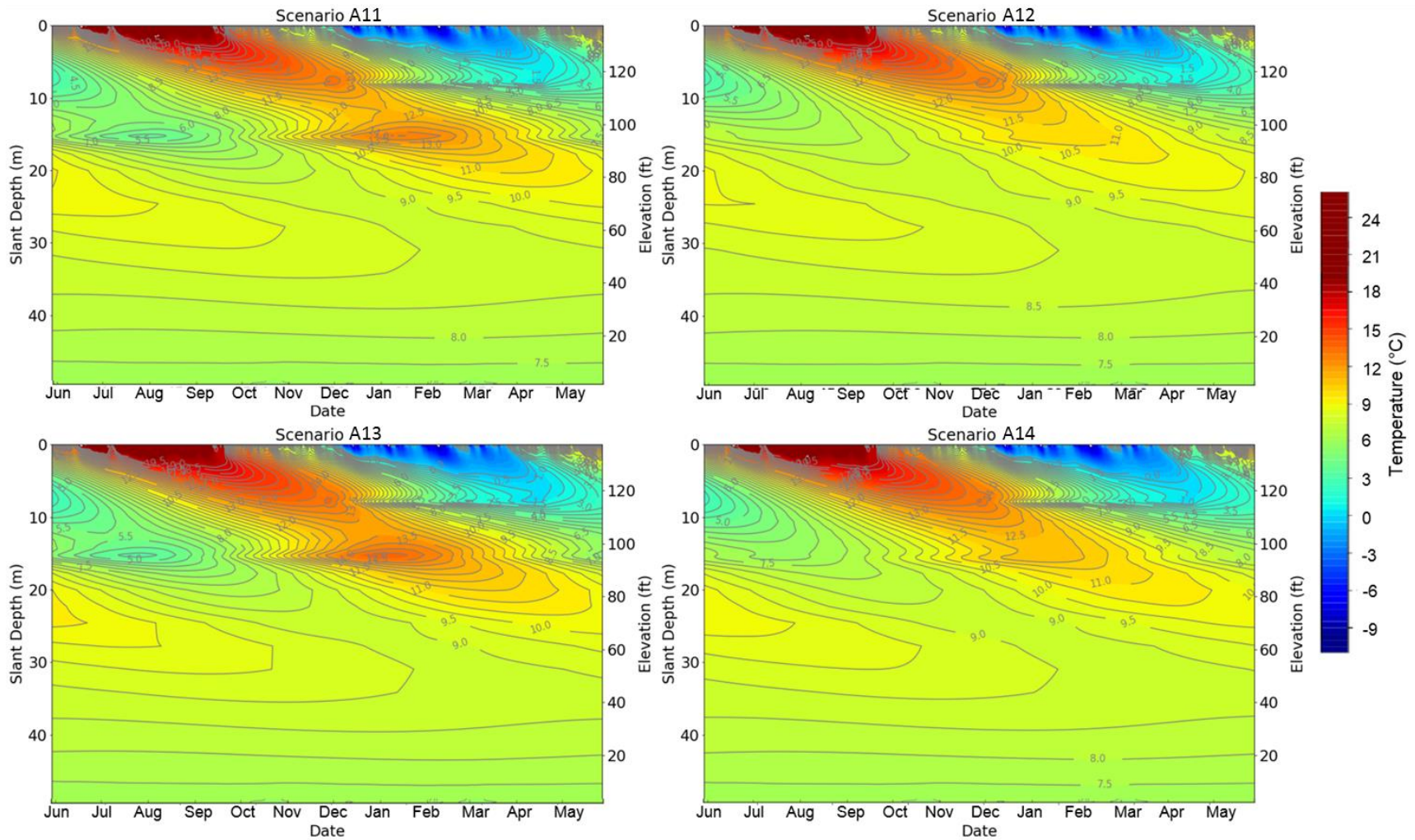


Figure 5-17: Simulated temperature variations versus time for scenarios A11 to A14.

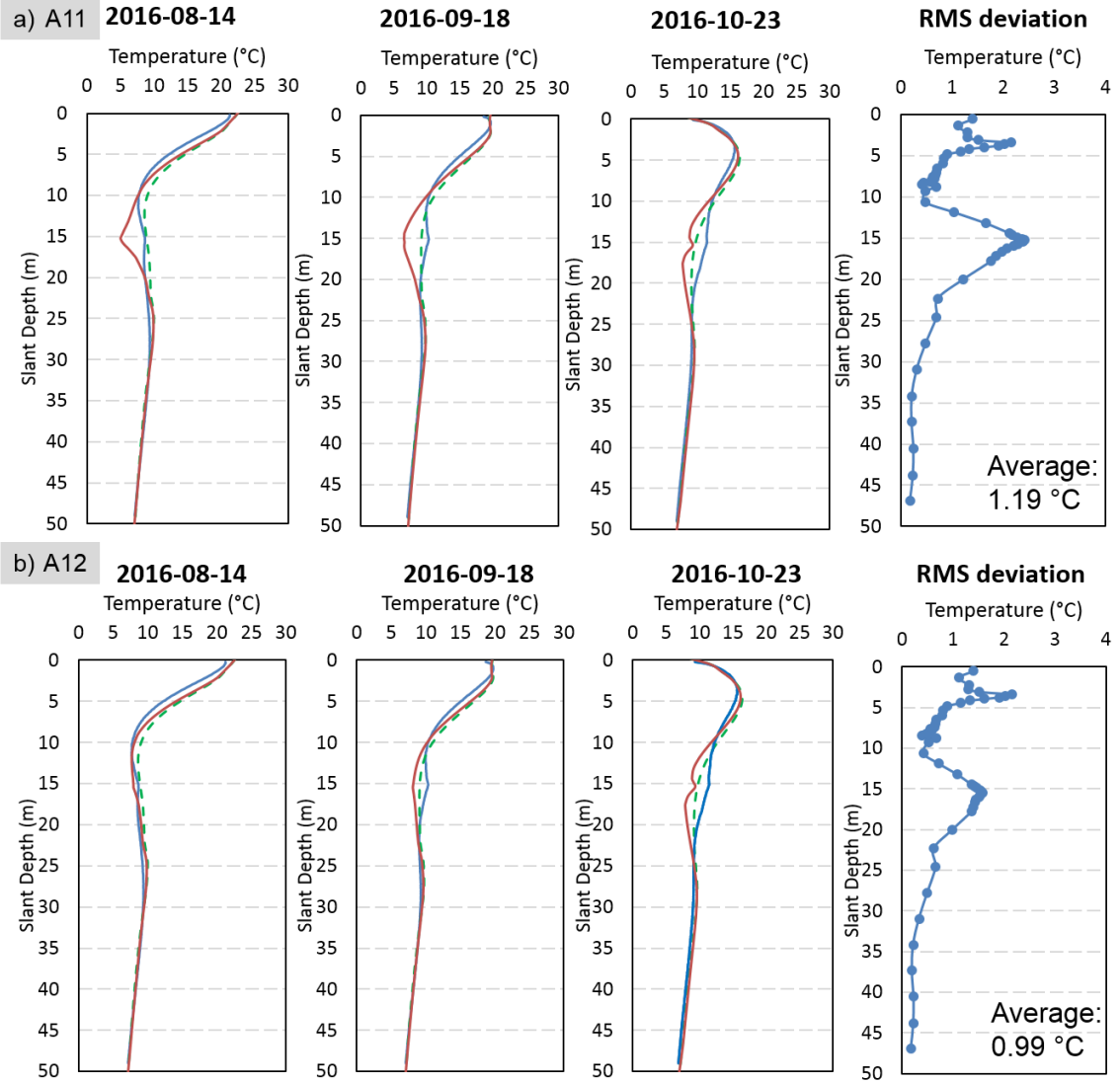


Figure 5-18: Comparisons of weekly average DTS temperature profiles (in blue) to the simulated anomalous temperature profile (in red) and bulk seepage profile (in dashed green) for August, September and October in 2017, along with annual average RMS deviation as a function of depth for scenarios a) A11 and b) A12.

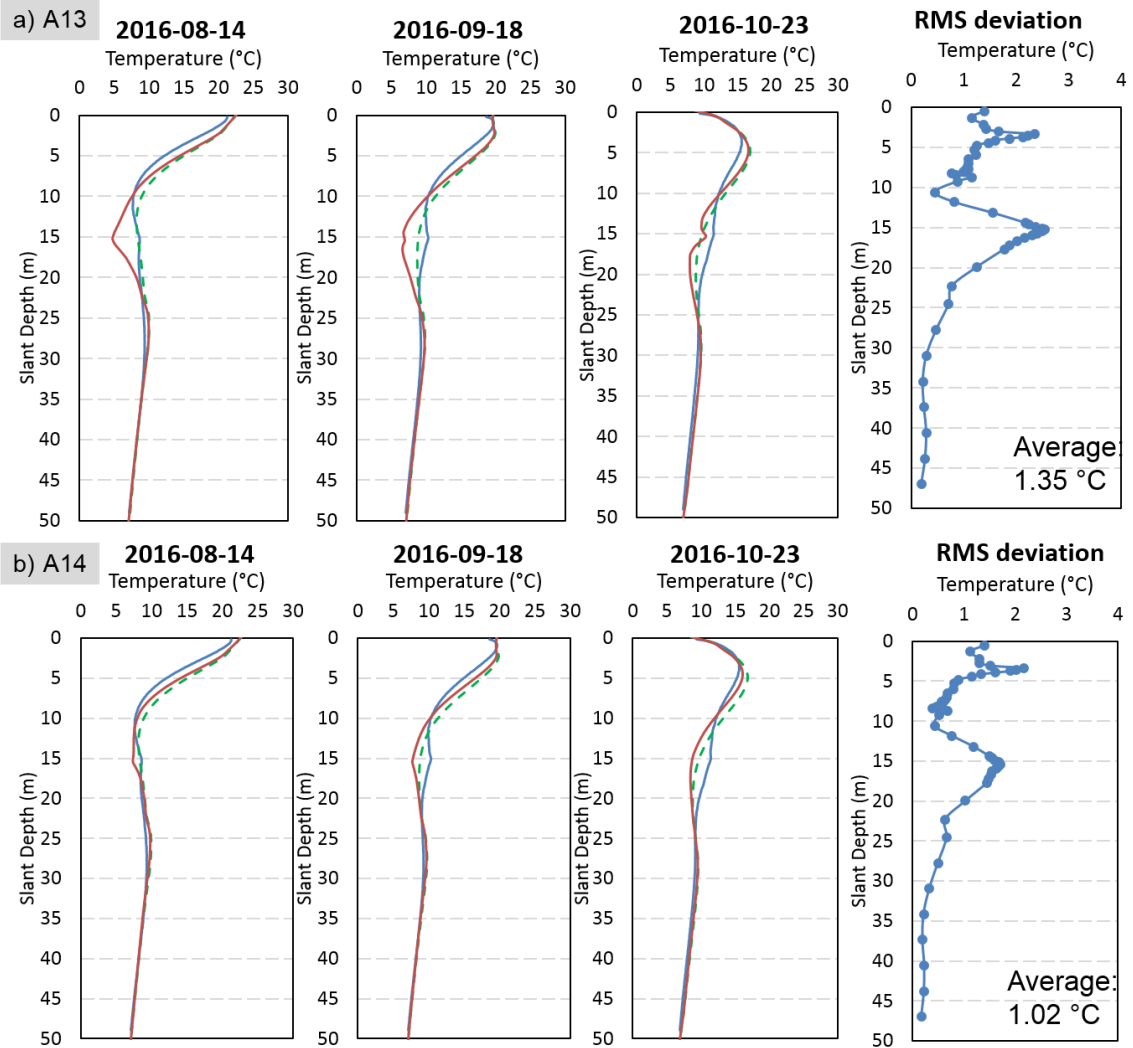


Figure 5-19: Comparisons of weekly average DTS temperature profiles (in blue) to the simulated anomalous temperature profile (in red) and bulk seepage profile (in dashed green) for August, September and October in 2017, along with annual average RMS deviation as a function of depth for scenarios a) A13 and b) A14.

The seepage rate time series for scenarios A11 to A14 and two bulk seepage scenarios (B9 and B10) are plotted in Figure 5-20. The annual average seepage rate and the increased seepage rate relative to the bulk seepage are summarized in Table 5-8. Although the hydraulic conductivity of the embankment core simulated in scenario A13 is larger than that in scenario A11, which resulted in a larger seepage rate in scenario

A13, the increased seepage associated with the addition of the concrete seepage zone at elevation 95' (slant depth 15.5 m) remains the same. However, the intensity of the temperature anomaly induced at the seepage zone is larger in scenario A13 than in scenario A11 (Figure 5-18 a) and Figure 5-19 a)) due to the increase of the total seepage, which brings more heat by convection. The same observations can also be made when comparing scenarios A12 and A14.

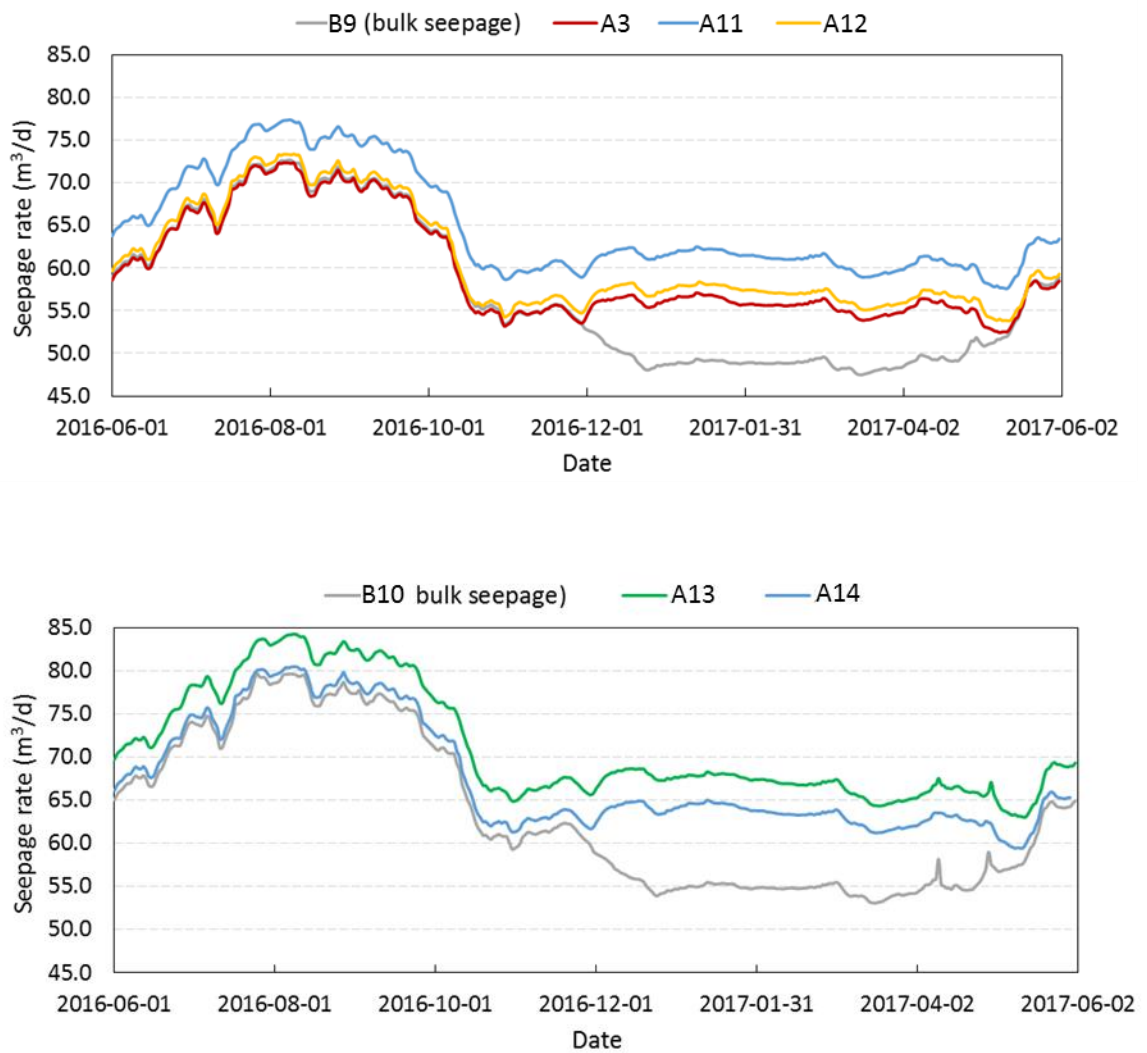


Figure 5-20: Seepage rate (daily average) versus time for scenarios A11 to A14 and A3 as well as bulk seepage scenarios B9 and B10.

Table 5-8: Annual average seepage rate, the increased seepage rate, and the annual and spatial average RMS deviations for scenarios A11 to A14.

Scenario No.	Seepage rate (annual average) m <sup>3</sup> /d	Increased seepage rate (relative to bulk seepage) m <sup>3</sup> /d	RMS deviations (annual average) °C
B9 (bulk)	57.1	-	1.34
A3	59.7	2.6	0.95
A11	64.9	7.8	1.19
A12	60.9	3.8	0.99
B10 (bulk)	63.3	-	1.30
A13	71.1	7.8	1.35
A14	67.1	3.8	1.02

## 5.5 Discussion

### 5.5.1 Influence of grouting on seepage

Some data obtained after a SEP grouting program in the fall of 2017 also support the conclusions derived from the simulations above, that the shallow temperature anomaly was likely caused by seepage along the interface and in the concrete, while the deep temperature anomaly was more likely related to seepage within the concrete. Grouting was performed by drilling a fan-shaped pattern of seven boreholes on the upstream side of the road just inside the south-facing sloped surface of the SEP from September 11 to 15, 2017. These seven boreholes were spaced 0.2 m at the top of the dam with grouting depths varied from elevation 72' to elevation 82.5' (R. Mugume, pers. comm., 2018). A cement-sand grout was injected from the top of the dam. Figure 5-21 compares the daily average DTS temperature profiles measured before and after the concrete grouting on December 19, 2016/2017 and February 16, 2017/2018. The results show that the shallow temperature anomaly is still present but slightly diminished in

height. The bottom of the shallow anomaly remained at the same depth before and after the grouting, but the top of the shallow anomaly dropped from about 128' to 124'. This suggests that the uppermost part of the shallow temperature anomaly is controlled by seepage in the concrete; however, the persistence of the lower part of the shallow anomaly adds credence to the interpretation that there is also seepage along the interface (or in the embankment), which was not affected by concrete grouting. It can also be seen from the comparison of temperature profiles on February 16, 2017/2018 that the deep temperature anomaly at elevation 95' disappeared in 2018 after concrete grouting. Furthermore, photos of the SEP concrete wall (Figure 5-22) show that an icefall emanating from a crack in the concrete at 95' elevation in April 2017 did not recur in April 2018.

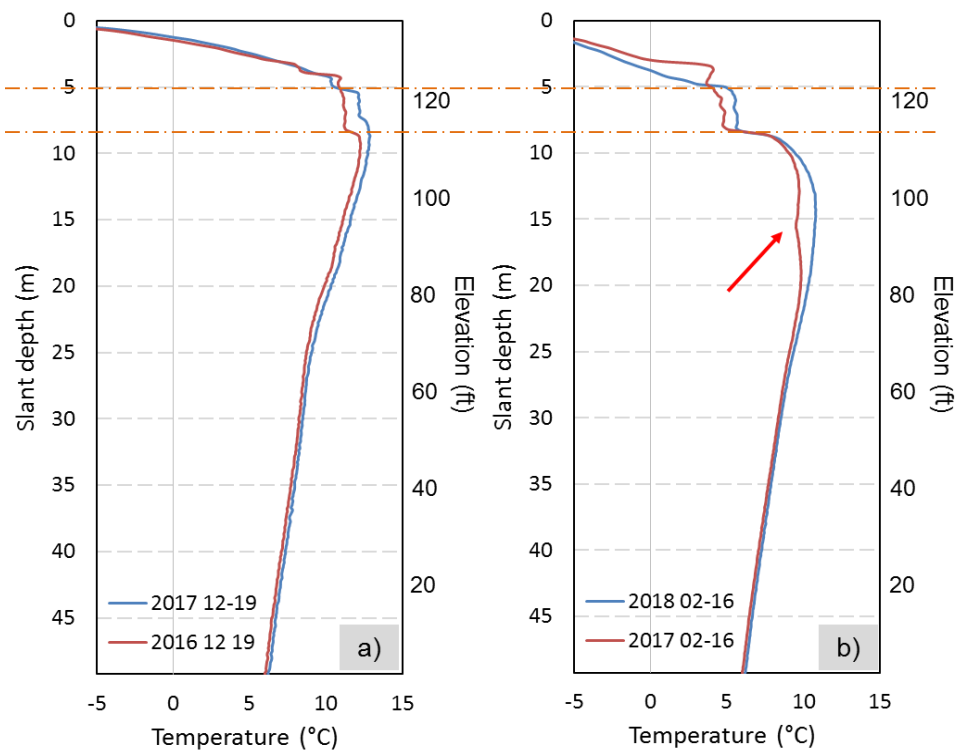


Figure 5-21: Comparisons of daily average DTS temperature profiles on a) December 19, 2016/2017, and b) on February 16, 2017/2018.



Figure 5-22: Photos of the back of the SEP concrete wall showing that an icefall emanating from a crack in the concrete at elevation 95' in April 2017 had disappeared in April 2018.

### 5.5.2 Influence of freeze and thaw cycle

The influence of freezing and thawing of pore water within the embankment and concrete on heat transport was investigated using piFreeze, a recently developed FEFLOW plug-in module (Clausnitzer & Mirnyy, 2016). In addition to the air, liquid and solid phases considered for partially-saturated flow, an ice phase and latent heat are included in the piFreeze module.

Scenarios B9 (bulk seepage, Section 4.4) and A9 (anomalous seepage zone simulated along interface at shallow depth, Section 5.3.2) were simulated in FEFLOW with the piFreeze plug-in. The simulated temperatures for scenario B9 obtained with piFreeze only show an average of 0.02 °C temperature difference along the borehole for

an entire year when compared to the results of the original scenario B9, which did not consider freeze-thaw. The simulated temperatures for scenario A9 obtained with piFreeze show a slight reduction in temperatures between 3 m to 6 m slant depth from January to March, with an average of approximately 1°C temperature difference when compared to the original results for scenario A9.

Overall, the influence of the freeze and thaw process on the simulated temperatures along the borehole is not very significant, and it has a minor effect on the observed shallow temperature anomaly. However, this topic might warrant further investigations as it has generally not been considered in simulating heat transport in embankment dams.

### *5.5.3 Recommendations for improvement of anomalous seepage simulations*

The average RMS deviation of the simulated temperature from the measured DTS data for all scenarios varied from 0.95 °C (scenario A3) to 1.95 °C (scenario A10). The largest temperature misfits occur above a slant depth of 20 m (elevation 82.6') due to poor reproduction of the shallow observed temperature anomaly.

#### *5.5.3.1 Consider of heterogeneity in the clay till core*

Due to the lack of construction records indicating the exact thickness and placement of the core and because the core was constructed in lifts, its properties could vary with height (as observed in the dam seepage study of Smith and Konrad (2008)).

Thus, heterogeneity of the core was investigated to try to improve the fit to the DTS data. Two bulk seepage simulations were performed based on scenario B9. The hydraulic conductivity of the core above elevation 95' (slant depth of 15.5 m) in scenarios B11 and B12 was increased and decreased by a factor of four compared to the value used in scenario B9 ( $2.5 \times 10^{-7}$  m/s), respectively. The weekly average temperature profiles of scenarios B11 and B12 were then compared with the results of scenario B9 and the DTS data (Appendix J). Increasing the hydraulic conductivity of the upper core produced larger temperature variations above 15.5 m, with temperature increase in summer and temperature reduction in winter. Reducing the hydraulic conductivity of the upper core had only a slight effect on the temperature distributions when compared to the results of scenario B9, indicating that, at such low hydraulic conductivity, thermal conduction dominated the heat transport within the dam. Neither scenario could improve the fit to the DTS data through raising the temperature at the top of the shallow anomalous zone, suggesting that the heterogeneity of the core has a minor effect on the shallow temperature anomaly.

#### 5.5.3.2 Consideration of an alternative geometry for seepage paths in the concrete

It has been assumed in this study that the geometry of seepage paths in the concrete would be relatively thin horizontal layers, meant to represent seepage along boundaries between concrete pour lifts. However, recent (July, 2018) visual inspection of the concrete drill core from boreholes SEPI-1, SEPI-2 and SEPI-3, all drilled close to the interface and within a few metres of each other (Figure K.1 in Appendix K), has revealed that this assumption may be too limiting.

Comparisons between the core for the upper 30 m of the three boreholes show that the concrete between 20' and 30' (6.1 m and 9.1 m) slant depth, corresponding to the zone of the shallow temperature anomaly, was much more fractured in borehole SEPI-3 than in the other two boreholes (Figure K.2 to Figure K.4). The tan-colored water staining observed on the surfaces of the core breaks suggest that the fractures were not simply a consequence of damage generated during the drilling process. The height of this heavily fractured zone in borehole SEPI-3, and the fact that it is not evident in the other two boreholes, indicates that the seepage zone in the concrete may not be well-represented by a thin horizontal seepage zone.

In addition, both shallowly dipping water-stained fractures (as would be expected along pour lift boundaries) and steeply dipping water-stained fractures were observed in the core from the three boreholes. Examples of both types of fractures, distinguished by the angle between fracture surface and the core axis, are shown in Figure K.5 and Figure K.6. Although the steeply dipping fractures seemed to be less common, their existence suggests that the height of the shallow seepage zone may be more adequately represented by a taller concrete fractured zone without seepage zone along the dam/concrete interface.

#### 5.5.3.3 Consider seepage in the concrete isolated from the embankment

The misfits between observed and simulated temperatures in the deeper anomalous seepage zone at elevation 95' were mainly due to opposing seasonal temperature changes. For example, the simulated temperature at elevation 95' in September was anomalously low, while the observed DTS temperature was anomalously

high (Figure 5-18). The fit of the simulated temperature anomaly to the DTS data may be improved by a fractured concrete model similar to scenario A11 (Table 5-7), but with the horizontal extent of the thin seepage zone reduced so that it does not reach the embankment/concrete interface. In this case, seepage from the embankment, which is colder than the headpond temperature in September (Figure 5-23) due to the time lag between the temperature in the headpond and within the dam, would be impeded from entering the concrete seepage zone and influencing the borehole temperature directly. As illustrated in Figure 5-24, the borehole temperature within the seepage zone in September would instead be mainly influenced by the warm headpond water moving relatively rapidly through the hydraulically conductive concrete seepage zone, thus producing an anomalous temperature increase at elevation 95' as observed in the DTS data.

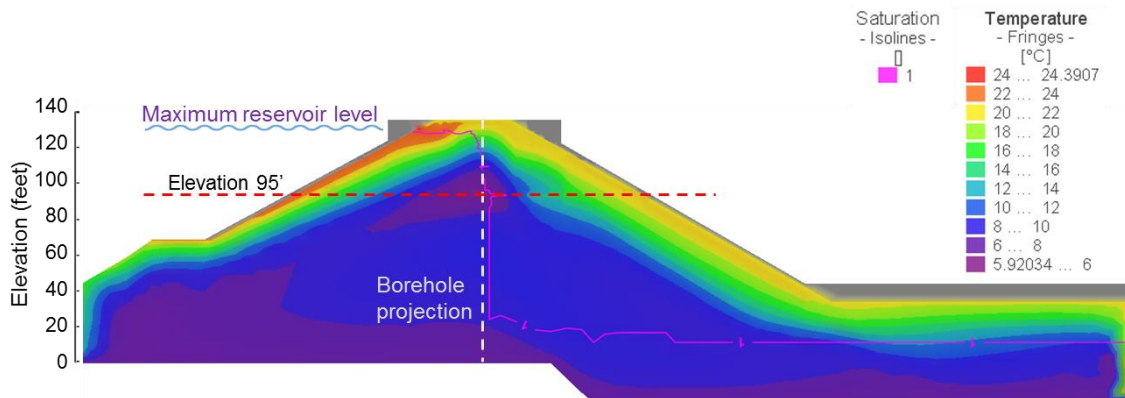


Figure 5-23: Temperature distribution within the embankment along the interface on September 1, indicating that the headpond water temperature is higher than the temperature at the clay till core at elevation 95' in September.

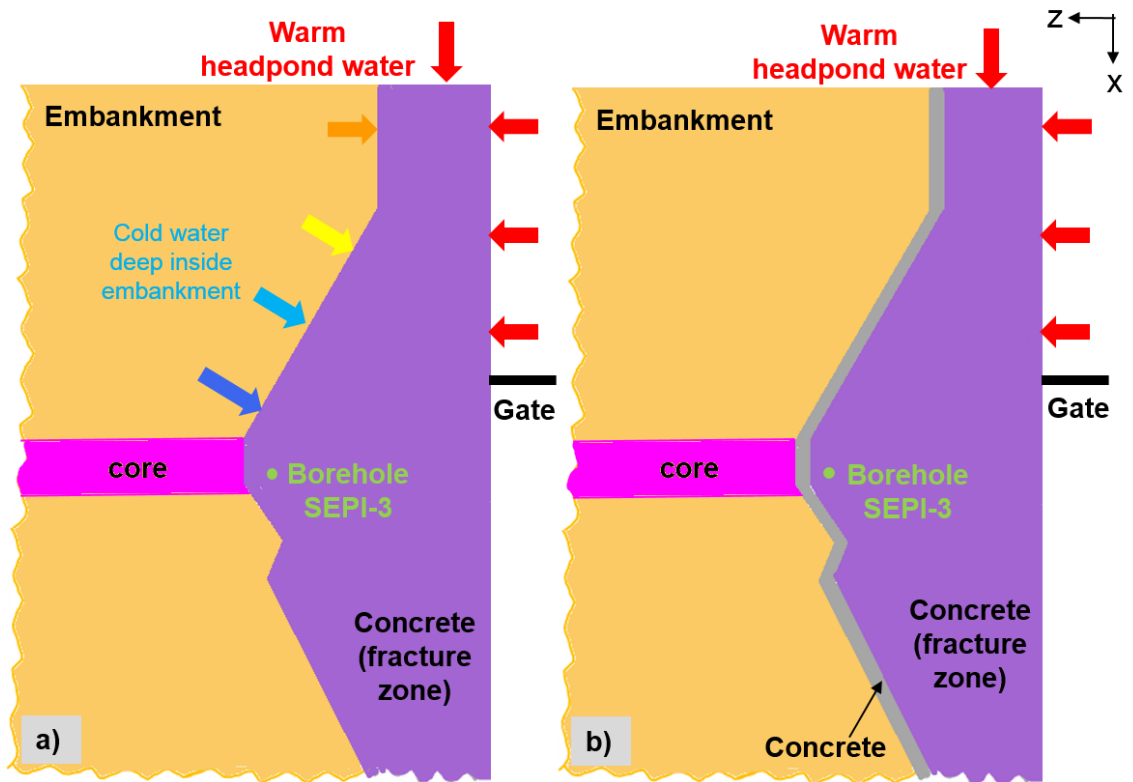


Figure 5-24: Schematic horizontal slice through the dam-concrete structure at elevation 95' illustrating how the water flow into a fracture zone in the concrete from the embankment and headpond would influence the borehole temperature in September depending on the horizontal extent of the fracture: a) extent from the interface to the outer concrete wall; b) reduced extent, not reaching the interface.

This idea was explored further by conducting an anomalous seepage simulation (scenario A15) with a 0.15 m height seepage zone, effectively disconnected from the embankment, simulated in the concrete at elevation 95'; the seepage zone was assumed active for an entire year. The hydraulic conductivity of the seepage zone was set as  $4.6 \times 10^{-4}$  m/s. The simulated seepage zone intersected the headpond on the outer SEP wall, but was terminated 0.3 m short of the embankment/concrete interface. The temperature profile comparisons between the simulated temperatures and DTS data are shown in Figure 5-25 for scenarios A11 and A15 in September and October. As

hypothesized, the anomalously warm zone observed in the DTS data at elevation 95' (slant depth 15 m) was much more successfully reproduced in scenario A15. The annual and spatial average RMS deviation of the simulated temperatures in scenario A15 from the DTS data was reduced to 1.29 °C when compared to that of the bulk seepage simulation (1.34 °C). Adding a shallow seepage zone like those simulated in Section 5.3, or a shallow one in the concrete that is similarly disconnected from the embankment may help to further improve the fit to the DTS data.

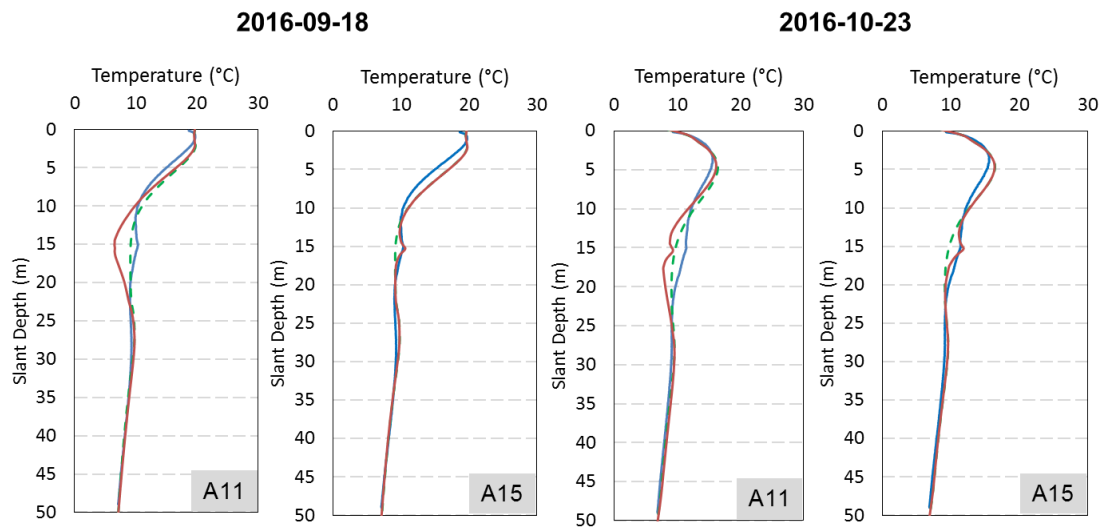


Figure 5-25: Comparisons of weekly average DTS temperature profiles (in blue) to the simulated anomalous temperature profile (in red) and bulk seepage profile (in dashed green) for scenarios A11 and A15 in September and October in 2017. Note that the simulated profiles in red match the observed profiles in blue much more closely for scenario A15, in which the deep concrete seepage zone is effectively disconnected from the embankment.

## **Chapter 6 : Conclusions**

In this research, spatial and temporal variations of temperature have been monitored and numerically modelled near the interface between the compacted clay till core of an embankment dam and an adjoining concrete diversion sluiceway structure at the Mactaquac Generating Station near Fredericton, NB, Canada. The field temperature data obtained by a DTS system in the SEPI-3 borehole were first critically examined and adjusted by comparisons to thermistor temperature measurements. They were subsequently investigated, using numerical simulations, to find possible explanations for temperature anomalies observed during the passive temperature monitoring. A parameter sensitivity analysis was performed for bulk (i.e. distributed) water seepage to investigate the influence of various thermal-hydraulic properties on the simulated temperature distributions and seepage rate. Additional anomalous seepage simulations were conducted to investigate the temperature anomalies observed in the DTS data at elevation 113' to 120-129', and at elevation 95' (Figure 2-5).

The parameter sensitivity analysis revealed that variations in porosity, longitudinal and transverse dispersivity, modified van Genuchten fitting parameters, and residual saturation within the ranges mainly recommended by Velásquez (2007) did not significantly affect the simulated temperature distributions and seepage rates within the dam. Of the parameters examined, the hydraulic conductivity and thickness of the core had the dominant influence on bulk seepage and the temperature distributions. Changing the hydraulic conductivity of the concrete did not make a significant difference as long as it remained much lower than that of the embankment dam core. The thermal properties of the concrete (including thermal conductivity and volumetric heat capacity)

were found to be more sensitive than those of the embankment in terms of their influence on temperature variations along the SEPI-3 borehole. For example, varying the thermal conductivity of the core (embankment) did not have a significant effect on the simulated temperatures, while increasing of the thermal conductivity of the concrete induced deeper penetration of the seasonal temperature variations provided the hydraulic conductivity of the core was sufficiently high.

The seasonal temperature variations that were observed in the DTS data near the surface, and a relatively steady temperature distribution at greater depths, were successfully reproduced in the bulk seepage simulation. Simplified heat transport modelling, that was effectively 2D, demonstrated that concentrated seepage near the dam/concrete interface must be present within 0.3 m of the borehole, to account for the strong temperature gradients associated with the shallow temperature anomaly. Subsequent 3D modelling of coupled seepage and heat transport therefore considered seepage paths both in the concrete and along the embankment/concrete interface.

Simulations of anomalous seepage zones in the concrete, embankment and in both locations simultaneously produced temperature drops during winter at shallower depths. Varying the hydraulic conductivity of a seepage zone along the interface was indistinguishable from changing its horizontal extent in terms of the effect on temperature. Increasing the hydraulic conductivity and the cross-sectional area (height x thickness) of the simulated seepage zone resulted in both a higher simulated seepage rate and a larger magnitude for the temperature anomaly.

The strong temperature gradients observed in the DTS data at the upper boundary of the shallow seepage zone could not be reproduced through any of the anomalous seepage modelling scenarios that were considered. The inconsistency is that simulated temperatures associated with bulk seepage in the upper part of the shallow temperature anomaly in early winter are already lower than the measured DTS temperatures, and adding a concentrated seepage path in winter only produces further cooling.

A 0.09 m high seepage zone simulated within the concrete only (scenario A3) was able to reproduce the strong temperature gradient at the lower boundary of the shallow seepage zone. However, seepage along such a thin layer could not reproduce the vertical extent of the near-constant temperature zone within the shallow temperature anomaly. A 2.9 m high seepage zone simulated along the dam/concrete interface (scenario A8 and A9) successfully reproduced the vertical extent of the shallow anomaly but not the strong temperature gradients. A seepage zone with a larger height in the concrete near the SEPI-3 borehole, as suggested by recent inspection of drill core, may reproduce both the strong temperature gradients at the boundaries of the shallow seepage zone as well as its vertical extent, although it is unlikely to resolve the problem of simulated temperatures in the upper part of the shallow seepage zone being too cold during winter. In conclusion then, the shallow temperature anomaly would appear to be at least partially a consequence of seepage in the concrete, but it is not fully explained by any of the models considered, and we cannot say for certain whether it involves a component of seepage along the embankment/concrete interface

A 0.15 m high seepage zone simulated in the concrete at elevation 95' (scenario A11 and A13) induced a narrow temperature anomaly similar to that measured, except that it is cold (rather than warm) in summer and warm (rather than cold) in winter. Analysis of this problem suggested that it could be a consequence of the simulation allowing water in the interior of the embankment, having a seasonal temperature variation significantly lagging that in the headpond, to be drawn into the concrete seepage zone. A similar simulation, except with the concrete seepage zone effectively isolated from the embankment, produced an improved fit to the DTS data, confirming the hypothesis and indicating that this minor temperature anomaly was likely to be related to seepage within the concrete only – a conclusion supported by the results of recent concrete grouting operations.

Due to the imperfect reproduction of the two observed temperature anomalies, the annual average seepage rate, which represents the total outflow from the modelling domain determined along the downstream slope of the dam, is uncertain. Obvious increases in seepage rate can be observed when zones with enhanced hydraulic conductivity are introduced into the model.

The results of this study demonstrate that passive DTS monitoring is a feasible approach to identify potential seepage zones near an embankment dam/concrete structure interface. Anomalous temperature zones, and associated gradients, can be clearly identified and finite element numerical modelling can, in some cases, indicate whether such anomalies are related to seepage in the concrete or in the embankment. However, other details such as the water flow path geometries and seepage rate are not as well constrained. In particular, varying the hydraulic conductivity and horizontal

extent of a simulated seepage zone can produce very similar effects on the simulated seepage rate and temperature variations along the monitoring borehole.

## REFERENCES

- Al-Ansari, N., Adamo, N. Sissakian, V., Knutsson, S., & Laue, J. (2017). Is Mosul dam the most dangerous dam in the world? Review of previous work and possible solutions. *Engineering*, 9, 801-823.
- Alejandro, V. B. (2014). *Modelling internal erosion within an embankment dam prior to breaching* (Master's thesis). Royal Institute of Technology, Stockholm, Sweden.
- Artières, O., Beck, Y. L., Khan, A. A., Cunat, P., Fry, J. J., Courivaud, J. R., Guidoux, C., & Pinettes, P. (2010). Assessment of dams and dikes behaviour with a fibre optics based monitoring solution. R.R. Garcia, M.A. Mir, F.H. Britian, R.L. Dios, M.R.C. Caballero (Eds.). *Dam Maintenance and Rehabilitation II. Proceedings of the 2nd International Congress on Dam Maintenance and Rehabilitation*, 79-86.
- Artières, O., Bonelli, S., Fabre, J.P., Guidoux, C., Radzicki, K., Royet, P., & Vedrenne, C. (2007). Assessment of the risk of internal erosion of water retaining structures: dams, dykes and levees. M. Aufleger, J. Fry, M. Goltz, & S. Perzmaier (Eds.). *Active and passive defences against internal erosion of dikes*. Symposium conducted at the International Congress on Large Dams, Freising, Germany.
- Aufleger, M., Conrad, M., Goltz, M., Perzmaier, S., & Porras, P. (2007). Innovative Dam Monitoring Tools Based on Distributed Temperature Measurement. *Jordan Journal of Civil Engineering*, 1(1), 29-37.

Aufleger, M., Goltz, M., Dornstädter, J., & Mangarovski, O. (2011). Distributed fibre optic temperature measurements in embankment dams with central core—new benchmark for seepage monitoring. In A. J. Schleiss & R. M. Boes (Eds.), *Dams and reservoirs under changing challenges* (pp.107- 114). London, England: Taylor & Francis.

Aufleger, M., Goltz, M., Perzmaier, S., & Dornstädter, J. (2008). Integral seepage monitoring on embankment dams by the DFOT Heat Pulse Method. *Proceedings of the 1st International Conference on Long Time Effects and Seepage Behaviour of Dams*.

Baker, M. (2011). The Fontenelle Dam Incident: The Investigation, Likely Causes, and Lessons (Eventually) Learned. *ASDSO Annual Conference*. Washington, D.C.: Association of State Dam Safety Officials.

Beck, Y. L., Khan, A. A., Cunat, P., Guidoux, C., Artières, O., Mars, J., & Fry, J. J. (2010). *Thermal monitoring of embankment dams by fibre optics*. Symposium conducted at the 8th International Congress on Large Dams, Innsbruck, Austria.

Blecher, J. J., Palmer, T. A., & DebRoy, T. (2012). Laser-silicon interaction for selective emitter formation in photovoltaics. I. Numerical model and validation. *Journal of Applied Physics*, 112(11), 114906.

Bofang, Z. (2013). *Thermal stresses and temperature control of mass concrete*. Waltham, MA: Butterworth-Heinemann.

- Butler, K.E. (2013). *Earth dam – concrete interface delineation at Mactaquac Generating Station by borehole seismic reflection surveying*. Report prepared for New Brunswick Power Generation Corporation.
- Butler, K.E., McLean, D.B., Cosma, C., & Enescu, N. (2018). *A borehole seismic reflection survey in support of seepage surveillance at the abutment of a large embankment dam*. Manuscript submitted for publication.
- Clausnitzer V., & Mirnyy V. (2016). Modeling groundwater and heat flow subject to freezing and thawing. Drebenstedt, Carsten, Paul, Michael (Eds.). *Proceeding of IMWA 2016, Freiberg, Germany*, 1150-1153.
- Conlon, R., & Ganong, G. (1966). The foundation of the Mactaquac rockfill dam, *Engineering Journal*, April, 33-38.
- Cuong, B. Q., Thai N.C., Yihong, Z., & Chunju, Z. (2017a). Estimating seepage in embankment dams based on temperature measurement: a review paper. *International Journal of Engineering Research & Technology*, 6(1), 106-112.
- Cuong, B. Q., Yihong, Z., & Chunju, Z. (2016). Seepage evaluation in embankment dam based on short-term temperature observation and heat injection. *Electronic Journal of Geotechnical Engineering*, 21(26), 10493-10506.
- Cuong, B. Q., Yihong, Z., & Chunju, Z. (2017b). The capacity of active heat method in evaluation of seepage. *Heat Transfer-Asian Research*. 47(1), 150-164
- Curtis, D.D., Feng, L., Sooch, G.S., Zheng, J., & Fletcher, J. (2016). *Practical analysis and assessment of AAR affected dams and hydroelectric plants*. Paper presented at 36th Annual United Society on Dams (USSD) Conference, Denver, Colorado.

- Diersch, H. J. G. (2009a). *FEFLOW® finite element subsurface flow and transport simulation system*. Reference Manual. DHI-WASY GmbH Berlin.
- Diersch, H. J. G. (2009b). Treatment of free surfaces in 2D and 3D groundwater modeling. *Finite Element Subsurface Flow & Transport Simulation System, White Papers*, 1: 67-100.
- Diersch, H. J. G., & Perrochet, P. (2009). On the primary variable switching technique for simulating unsaturated-saturated flows. *Finite Element Subsurface Flow & Transport Simulation System, White Papers*, 1: 9-66.
- Diersch, H. J. G. (2013). *FEFLOW: finite element modeling of flow, mass and heat transport in porous and fractured media*. New York, NY: Springer Science & Business Media.
- Diersch, H. J. G. (2016). *FEFLOW 7.0 user guide*. DHI-WASY GmbH Berlin.
- Dornstädter, J. (2013). Leakage Detection in Dams - State of the Art. In *the 20th Anniversary of SLOCOLD, Ljubljana*, 77-86111.
- Fell, R., & Fry, J. J. (2007). The state of the art of assessing the likelihood of internal erosion of embankment dams, water retaining structures and their foundations. In R. Fell & J.J. Fry (Eds.), *Internal erosion of dams and their foundations*, London, England: Taylor & Francis.
- Fell, R., MacGregor, P., & Stapledon, D. (1992). *Geotechnical engineering of embankment dams*. Dutch: A. A. Balkema. ISBN: 9789054101284.

- Fell, R., & Wan, C. F. (2005). *Methods for estimating the probability of failure of embankment dams by internal erosion and piping in the foundation and from embankment to foundation* (Report No. 436). Sydney, Australia: University of New South Wales. ISBN: 85841-403-1.
- Fell, R., Wan, C. F., Cyganiewicz, J., & Foster, M. (2003). Time for development of internal erosion and piping in embankment dams. *Journal of Geotechnical and Geoenvironmental Engineering*, 129(4), 307–314.
- Fetter, C. W. (2000). *Applied hydrogeology* (4th edition). New Jersey, United states: Prentice hall.
- Flores, B. R., Ramirez, R. M., & Macari, E. J. (2011). Internal erosion and rehabilitation of an earth-rock dam. *Journal of Geotechnical and Geoenvironmental Engineering*, 137(2), 150–160.
- Foster, M., Fell, R., & Spannagle, M. (2000a). A method for assessing the relative likelihood of failure of embankment dams by piping. *Canadian Geotechnical Journal*, 37(5), 1025-1061.
- Foster, M., Fell, R., & Spannagle, M. (2000b). The statistics of embankment dam failures and accidents. *Canadian Geotechnical Journal*, 37(5), 1000-1024.
- Gilks, P., May, T., & Curtis, D. (2001). A review and management of AAR at Mactaquac Generating Station. *Proceedings of the Canadian Dam Association 2001 Annual Conference*, 167-177.
- Hanke, K. (2014). *Development of relationships between seismic wave velocities and porosity for concrete at Mactaquac dam*. Paper prepared to fulfil the CE5913 Special studies at the University of New Brunswick.

- Hausner, M. B., Suárez, F., Glander, K. E., Giesen, N. V. D., Selker, J. S., & Tyler, S. W. (2011). Calibrating single-ended fibre-optic Raman spectra distributed temperature sensing data. *Sensors*, *11*(11), 10859-10879.
- Hickey, C., Ekimov, A., Hanson, G. & Sabatier, J. (2009). Time-lapse seismic measurements on a small earthen embankment during an internal erosion experiment. In *22nd EEGS Symposium on the Application of Geophysics to Engineering and Environmental Problems*, Fort Worth TX, USA, 144-156.
- Hoffmann, L., Muller, M., Kramer, S., Giebel, M., Schwotzer, G., & Wieduwilt, T. (2007). Applications of fibre optic temperature measurement. *Proceedings of the Estonian Academy of Sciences*, *13*(4), 363-378.
- Huen, K., Tighe, S., Mills, B., & Perchanok, M. (2006). *Development of tools for improved spring load restriction policies in Ontario*. Paper presented at 2006 Annual Conference of the Transportation Association of Canada, Charlottetown, Prince Edward Island.
- Johansson, S. (1997). *Seepage monitoring in embankment dams*. (Doctoral dissertation), Royal Institute of Technology, Stockholm, Sweden.
- Johansson, S. (2009). *A guide for seepage monitoring of embankment dams using temperature measurements*. (Report No. T062700-0214). Montreal, Canada: CEATI International Inc.
- Kamanbedast, A., & Shahosseini, M. (2011). Determination of seepage and analysis of earth dams (Case study: Karkheh Dam). *Iranica Journal of Energy and Environment*, *2*(3), 201-207.

- Keenan, G. (1969). *A study of overconsolidated clayey soils* (Master's thesis). University of New Brunswick, Fredericton, Canada.
- Khaleel, R., Relyea, J. F., & Conca, J. L. (1995). Evaluation of van Genuchten–Mualem relationships to estimate unsaturated hydraulic conductivity at low water contents. *Water Resources Research*, *31*(11), 2659-2668.
- Khan, A. A., Cunat, P., Beck, Y. L., Mars, J. I., Vrabie, V., & Fabre, J. P. (2010a). Distributed fibre optic temperature sensors for leakage detection in hydraulic structures. In *the 5th World Conference on Structural Control and Monitoring*, Tokyo, Japan.
- Khan, A.A., Vrabie, V., Mars, J., Girard, A., & D'Urso, G. (2010b). Automatic monitoring system for singularity detection in dikes by DTS data measurement. *IEEE Transaction on Instrumentation and Measurement*, *59*(8), 2167-2175. doi:10.1109.
- Kolala, M., Lungu, C., & Kambole C. (2015). The cause of dam failures a study of earthen embankment dams on the copperbelt province of Zambia. *International Journal of Engineering Research & Technology*, *4*(2), 301-309.
- Kumar, R., & Bhattacharjee, B. (2003). Porosity, pore size distribution and in situ strength of concrete. *Cement and Concrete Research*, *33*(1), 155-164.
- Lagerlund, J. (2009). *Remedial injection grouting of embankment dams with non-hardening grouts* (Licentiate thesis). Royal Institute of Technology, Stockholm, Sweden.

- Leger, P., Venturelli, J., & Bhattacharjee, S. S. (1993). Seasonal temperature and stress distributions in concrete gravity dams. Part 1: modelling. *Canadian Journal of Civil Engineering*, 20(6), 999-1017.
- Mairaing W., & Lapkengkrai S. (1993). Ratio of vertical to horizontal permeabilities of compacted soils. *Kasetsart Engineering Journal (Thailand)*, 7(19), 41-54.
- Markle, J. M., & Schincariol, R. A. (2007). Thermal plume transport from sand and gravel pits—Potential thermal impacts on cool water streams. *Journal of Hydrology*, 338(3), 174-195.
- Mattsson, H., Hellström, J. G. I., & Lundström, S. (2008). *On internal erosion in embankment dams: a literature survey of the phenomenon and the prospect to model it numerically*. Luleå, Sweden: Lulea University of Technology. ISSN: 1402-1528.
- Mehta, P.K. & Monteiro, P.J.M. (2006). *Concrete: structure, properties, and materials*. 3<sup>rd</sup> edition. New York, NY: McGraw-Hill.
- Mesri, G., & Ali, S. (1988). Hydraulic fracturing in embankment dams. *Journal of Geotechnical Engineering*, 114(6), 742-746. doi: 10.1061/(ASCE)0733-9410(1988)114:6(742)
- Miedema, D. (2004). *Selected case histories of dam failures and accidents caused by internal erosion* (Report No. DSO-04-03). Washington, D.C.: Bureau of Reclamation.
- Milanović, P. (2018). *Engineering karstology of dams and reservoirs*. Boca Raton, FL: Taylor & Francis.

- Narita, K. (2000). *Design and construction of embankment dams*. Aichi Institute of Technology. Retrieved from <http://aitech.ac.jp/tonarita/tembankmentdam1.pdf>.
- Opaliński, P., Radzicki, K., & Bonelli, S. (2016). Numerical modelling of coupled heat and water transport on embankment dam in Kozłowa Góra. *Technical Transactions*, 113(1-Ś) 117-126. doi: 10.4467/2353737XCT.16.200.5949.
- Radzicki, K. (2014). *The thermal monitoring method-A quality change in the monitoring of seepage and erosion process in dikes and earth dams*. Paper presented at the seminar of Modern Monitoring Solutions of Dams and Dikes, Hanoi.
- Radzicki, K., & Bonelli, S. (2011). Impulse Response Function Analysis model application to the thermal seepage monitoring in the earth dams. In *20ème Congrès Français de Mécanique*, Besançon, France.
- Richards, L. A. (1931). Capillary conduction of liquids through porous mediums. *Physics*, 1(5), 318-333.
- Ridley A., Brady K.C., & Vaughan P. R. (2003). *Field measurement of pore water pressures*. Report prepared for Quality Services, Civil Engineering Division, Highways Agency. TRL Report: TRL 555.
- Ringeri, A., Butler, K.E., & McLean, D.B. (2016). *Long term monitoring and numerical modelling of self-potential for seepage surveillance at Mactaquac dam, New Brunswick, Canada*. Proceedings of 69<sup>th</sup> Canadian Geotechnical Conference (GeoVancouver 2016), Oct. 2<sup>nd</sup> - 5<sup>th</sup>, Vancouver, Canada.

- Sharma, R. P., & Kumar, A. (2013). *Case histories of earthen dam failures*. Symposium conducted at the 7th International Conference on Case Histories in Geotechnical Engineering, Chicago, IL.
- Seed, H. B., & Duncan, J. M. (1981). The Teton dam failure: A retrospective review. *Proceedings of the 10th International Conference on Soil Mechanics and Foundation Engineering*, 4, 219-238.
- Sensornet Ltd. (n.d.). *Sentinel DTS user manual*. London, UK.
- Shija, N. P., & MacQuarrie, K. T. B. (2015). Numerical simulation of active heat injection and anomalous seepage near an earth dam–concrete Interface. *ASCE International Journal of Geomechanics*, 15(5), 04014084.
- Sjödahl, P., & Johansson, S. (2012). Experiences from internal erosion detection and seepage monitoring based on temperature measurements on Swedish embankment dams. In *the 6th International Conference on Scour and Erosion*, Paris, France.
- Smith, M., & Konrad, J. M. (2008). Analysis of the annual thermal response of an earth dam for the assessment of the hydraulic conductivity of its compacted till core. *Canadian Geotechnical Journal*, 45(2), 185-195.
- Soliman, H., Kass, S., & Fleury, N. (2008). *A simplified model to predict frost penetration for Manitoba soils*. Poster session presented at the 2008 Annual Conference of the Transportation Association of Canada, Toronto, Ontario.

- Song, C. R., & Yosef, T. Y. (2017). Seepage monitoring of an embankment dam based on hydro-thermal coupled analysis. *Journal of Engineering Materials and Technology*, 139(2), 021024.
- Sooch G. (2016). *New Brunswick power generation Mactaquac water retaining structure: coupled thermal-structural analysis of south end pier*. Project memo prepared for HATCH.
- Tanchev, L. (2014). *Dams and Appurtenant Hydraulic Structures* (2nd ed., pp. 499). London: Balkema.
- U.S. Army Corps of Engineers. (2004). *General design and construction considerations for earth and rock-fill dams: Engineer Manual* (Manual No. 1110-2-2300). Washington, D.C.: U.S. Army Corps of Engineers.
- Van De Giesen, N., Steele-Dunne, S. C., Jansen, J., Hoes, O., Hausner, M. B., Tyler, S., & Selker, J. (2012). Double-ended calibration of fibre-optic Raman spectra distributed temperature sensing data. *Sensors*, 12(5), 5471-5485.
- Velásquez, J.P.P. (2007). *Fibre optic temperature measurements: further development of the gradient method for leakage detection and localization in earthen structures*. München: Technische Universität München.
- Venturelli, J. (1992). *Seasonal temperature and stress distributions in concrete gravity dams* (Master's thesis). McGill University, Montreal, Canada.
- Vuola, P., Konrad, J., & Bartsch, M. (2007). Assessment of the risk of internal erosion of water retaining structures: dams, dykes and levees. M. Aufleger, J. Fry, M.

Goltz, & S. Perzlmaier (Eds.). *Effects of frost and thaw on dams*. Symposium conducted at the International Congress on Large Dams, Freising, Germany.

Wong, W. S., Rees, D. A. S., & Pop, I. (2004). Forced convection past a heated cylinder in a porous medium using a thermal nonequilibrium model: finite Peclet number effects. *International Journal of Thermal Sciences*, 43(3), 213-220.

Yousefi, S., Ghiassi, R., Noorzad, A., Ghaemian, M., & Kharaghani, S. (2013). Application of temperature simulation for seepage inspection in earth-fill dams. *Grđevinar*, 65(09.), 825-832.

Zhu, P.Y., Zhou, Y., Thévenav, L., & Jiang, G. L. (2008). Seepage and settlement monitoring for earth embankment dams using fully distributed sensing along optical fibres. *Proceedings of the 2008 International Conference on Optical Instruments and Technology*, 716013. doi: 10.1117/12.81196.

## Appendix A. Instrumentation specification sheets

### A.1 Halo-DTS

The Halo-DTS is Sensornet's revolutionary DTS system that sets new standards in value and performance.

For industrial monitoring applications where reliability, safety and seamless system integration are essential, the compact, low-power, user friendly Halo-DTS is the ideal solution to close your monitoring gap. The system features an inbuilt multiplexing module (with either 2 or 4 channels) enabling up to 4 single ended measurements or 2 double-ended measurements. User configurable zones and alarms functionality are also available for a wide variety of applications. The system is packaged in a standalone unit which contains both the sensing optoelectronics and an onboard PC. The system operates with an intuitive software interface (based on Windows OS), making it a simple-to-use system. The system has been designed with safety in mind and has been tested to some of the industry's most rigorous standards.



#### Summary of sensing capabilities

RANGE	CHANNELS	TEMPERATURE RESOLUTION	SAMPLING RESOLUTION
0-4km	2 or 4	See reverse	2m

#### Operating environment

OPERATING TEMPERATURE	STORAGE TEMPERATURE	HUMIDITY
0°C to +40°C	-15°C to +65°C	5% to 95% relative humidity, non-condensing

#### Power requirements

AC POWER	DC POWER	POWER CONSUMPTION
100V - 240V, 50Hz - 60Hz	24V or 48V supply option available	40W - 50W maximum

#### Certification & compliance

SAFETY	EMC	CE MARK
The Halo DTS has been independently classified to EN 60825-1 (2001-03) as a Class 1M laser product. The DTS (1mW mean power output) is suitable to monitor Zone 0 Hazardous areas according to the European Commission report no. EUR 16011 EN (1994).	EN61326:1997/A1:1998; Conducted Emissions: Class B; Radiated Emissions: Class A**; EN 61000-4-3:1996; EN 61000-4-6:1996; EN 61000-4-4:1995; EN 61000-4-2:1995/A1:1998/A2:2001; EN 61000-4-11:1994; EN 61000-4-5:1995; EN 61000-3-2:1995; EN 61000-3-2:2000; EN 61000-3-3:1995	Accordance with 89/336 EEC. EMC Directive Accordance with LVD 72/23 EEC Directive: EN 41003; EN 50178; EN 60065; EN 60825-1; EN 60950; EN 61010-1

#### Physical dimensions\*

HEIGHT	WIDTH	DEPTH	WEIGHT
87mm (3.4 inches)	435mm (17.1 inches)	445mm (17.3 inches)	9kg (22lb)

\*Fits in standard 19 inch rack mounting.

All details are subject to change.



T: +44 (0)20 8236 2550  
E: enquiries@sensornet.co.uk  
W: www.sensornet.co.uk

## A.2 BRUsens fibre optic DTS cable

### BRUsens Temperature

3.50.1.006

High resolution temperature sensing cable with fiber to cable ratio of approx. 10 : 1  
dielectrical flexible mini fibre optic sensing cable

2 special bend optimised multimode sensing optical fiber, protected with additional strain relief and an additional dielectrical sheath

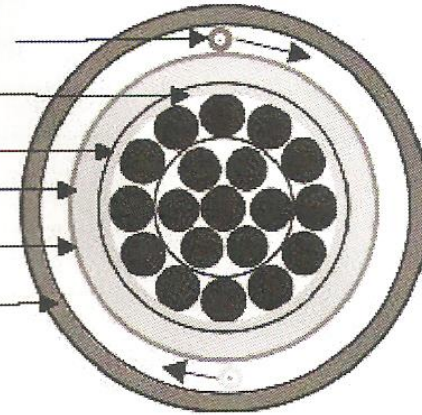
Special lightweight and flexible stranded (1/6/12) non-metallic core

Special strain relief, optimized for rough handling during installation

PE layer (yellow)

Soft dielectrical bedding layer (red)

PUR protective outer sheath optimized tensile load transfer into core. Easy temperature transfer to the fiber (blue)



#### Features:

- High resolution temperature sensing cable with approx. 10 m fiber in 1 m cable
- 2 fibers for single ended measurement with redundancy or one double ended measurement
- Flexible sensing cable for easy handling in rough environment
- Possibility for aerial installation
- Meter marking on outer sheath

#### Temperature range:

Operating temperature approx: -40° ... +85°C  
Storage temperature approx: -40° ... +85°C  
Installation temperature approx: 5° ... +50°C

#### Technical data

Type	Max. no. of fibres units	Cable Ø mm	Weight kg/km	Max. tensile strength	
				short term N	long term N
2F	2	approx. 26,60	approx. 530	to be defined	to be defined

Type	Min. bending radius		Max. crush resistance N/cm
	With tensile mm	Without tensile mm	
2F	to be defined	to be defined	to be defined

### A.3 PW series vibrating wire piezometer

The model used in this study is **PWS**.



### PW Series - Vibrating Wire Piezometer

Piezometer



HIGH ACCURACY  
LONG-TERM RELIABILITY  
WIDE MEASURING RANGE

The PW series of vibrating wire piezometers is designed to measure pore-water or other fluid pressure.

#### Description

The **PW** piezometer consists of a vibrating wire sensing element enclosed in a protective steel housing. The sensing element is essentially formed of a steel wire clamped to both ends of a hollow cylindrical body. An electromagnetic coil is used to excite the wire and to measure its vibration period. The period is sensitive to the pressure applied onto the sensing element.

The excellent long-term reliability of the **PW** results from the use of the latest developments in vibrating wire technology. For instance, the wire is clamped by a proven hydraulic swaging technique that ensures high stability. The sensing element is hermetically sealed in order to protect the steel wire against corrosion. All parts of the sensing element other than the wire are machined from a high-grade stainless steel. The **PW** is fitted with a surge protector and resists electrical and radio frequency interferences, as determined by tests compliant to IEEE and CEI specifications.

Five models of **PW** piezometers are available: The **PWS** is designed to be embedded in earth fills, at concrete/earth interfaces or inserted into boreholes and small-diameter pipes. The end of the **PWS** is fitted with a high or low air entry filter, which protects the sensing element from solid particles, allowing this model to sense only the fluid pressure to be measured. The filter is easily removable in case of saturation. The **PWF** is a thick-walled version of the **PWS** for use in direct burial applications. The **PWC** is provided with a pipe thread adapter, thus enabling the piezometer to be used as a pressure transducer. The **PWP** is designed to be driven into unconsolidated fine grain materials such as sand, silt or clay. The external housing is a thick-wall cylinder fitted with a conical shoe at one end and an EW drill rod or standpipe thread adapter at the cable entry end. The **PWL** is a low-pressure piezometer (35,70 kPa).

#### Key Features

- Rugged stainless steel construction
- High accuracy and resolution
- Triple stage water blocking
- Wide measuring range
- Temperature reading
- Long-term reliability
- Surge protection

#### Applications

- Hydraulic structures
- Retaining walls
- Embankments
- Dams

## Specifications

### PERFORMANCE

Range <sup>1</sup>	0.035 <sup>2</sup> , 0.070 <sup>2</sup> , 0.2, 0.35, 0.5, 0.75, 1, 1.5, 2, 3, 5, 7 MPa
Accuracy <sup>3</sup>	± 0.1%
Linearity <sup>3</sup>	< ± 0.5% F.S
Resolution with MB-3TL	0.025% F.S. (min.)
Thermal drift <sup>3</sup>	± 0.1% F.S. / °C
Thermistance	3 kΩ (see model TH-T)
Cable <sup>4</sup>	IRC-41A, IRC-390, IRC-41AV

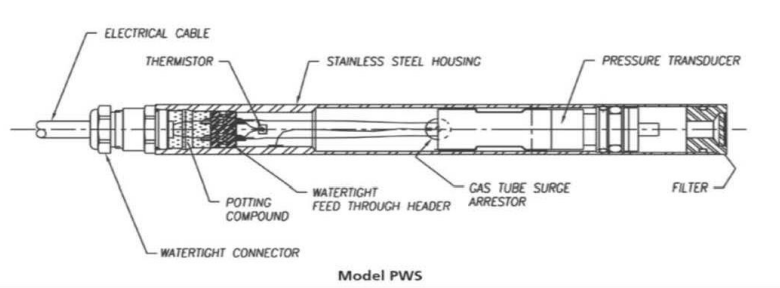
MODEL	PWS	PWF	PWC	PWP	PWL
Housing	Slim	Thick-walled	Threaded (STD ¼ in -18 NPT male)	Push-in-point	–
Outside diameter	19 mm	28.6 mm	19 mm	33.4 mm	38 mm
Length	200 mm	200 mm	213 mm	260 mm	200 mm
Material	Stainless steel				
Filter	Stainless steel, ~ 50 µm, ~ 10 kPa, low air entry Ceramic, ~ 1 µm, ~ 450 kPa, high air entry				

<sup>1</sup> Other ranges available on request. 1 MPa = 145 psi

<sup>2</sup> Available only with Model PWL

<sup>3</sup> Specifications achieved in laboratory conditions

<sup>4</sup> PWL must be used with vented cable type IRC-41AV



## Ordering Information

Please specify:

- Model and range
- Cable length

## Optional Accessories

- Type of thermistor, filter and cable
- Calibration to -100 kPa
- Readout instrument: MB-3TL, SENSLOG

Roctest Ltd,  
680 Birch Street  
St-Lambert, Quebec  
Canada J4P 2N3  
E5001D-160208

Phone +1 450 465 1113  
Fax. +1 450 465 1938

Email info@roctest.com  
Web www.roctest.com

Roctest reserves the right to make any changes in the specifications without prior notice

**NX** NOVA  
METRIX

## A.4 TH series – Temperature sensor

This study used model **TH-T** thermistors, integrated within PWS vibrating wire piezometers.



RELIABLE & SENSITIVE  
ROBUST CONSTRUCTION  
VARIOUS CONFIGURATIONS AVAILABLE

Temperature sensor series TH provides reliable means to monitor temperature in rock, concrete, soil, or ground fill

### Description

---

Temperature sensors are available in three different models: **TH-T**, **TH-PT100**, and **TH-TC**.

Model **TH-T** uses a 3 k $\Omega$  chip thermistor. The thermistor is encapsulated and sealed into a stainless steel or PVC cylindrical housing. Two lead wires are connected to the thermistor for readout. The **TH-T** incorporates the standard thermistor used in most vibrating wire instruments.

Model **TH-PT100** consists of a platinum resistor highly sensible to temperature. Platinum is well suited because of its stability at high temperature. A four- or three-wire bridge mounting gives a good measurement resolution with a portable bridge measurement device or a data acquisition system. The sensor is enclosed inside a stainless steel housing, which allows grouting while offering resistance to strain.

Model **TH-TC** is a thermocouple consisting of a twin solid thermocouple wire AWG 24, covered by a 0.38-mm thick PVC jacket and encapsulated in a PVC protective housing. It is usually connected with an extension wire, which will be connected to a readout unit. The thermocouple and extension wires are copper-constantan alloy (type T).

### Key Features

---

- Available in various configurations
- Reliable & sensitive
- Rugged

### Applications

---

- Dams and bridges
- Buildings and tunnel linings
- Influence of instrument temperature

## Specifications

MODEL	TH-T	TH-PT100 (Class A)	TH-TC TYPE T
Range*	-50 to +150°C	-200 to 600°C	-60 to +400°C
Accuracy	±0.5% F.S.	±0.15°C at 0°C	±0.1% F.S.
Resolution	0.1°C	Depends on readout	0.1°C
Sensor	3 kΩ thermistor	100 Ω resistor	Thermocouple
Housing	PVC or stainless steel	Stainless steel	PVC
	16 mm OD	16 mm OD	16 mm OD
	51 mm long	51 mm long	51 mm long
Cable	IRC-41A or IRC-295	IRC-41A	Duplex AWG 20 extension wire,
Sensibility	—	<0.1% F.S.	—

\* Temperature range of cable must be considered (e.g. -20 to +60°C for the IRC)

## Appendix B. Headpond temperature vs. depth profile from Mactaquac Aquatic Ecosystem (MAES) project

Figure B.1 shows the headpond water temperature versus time at various depths, measured from a thermograph string in the headpond from late July to late November, 2014, which is part of the Mactaquac Aquatic Ecosystem (MAES) project. Ten temperature sensors were deployed 2 to 34 m below surface at a spacing of 2 m at shallower depths and 5 m below 10 m depth. The location of the thermistor string is at site 24 (Figure B.2), which is less than 1 km upstream of the dam.

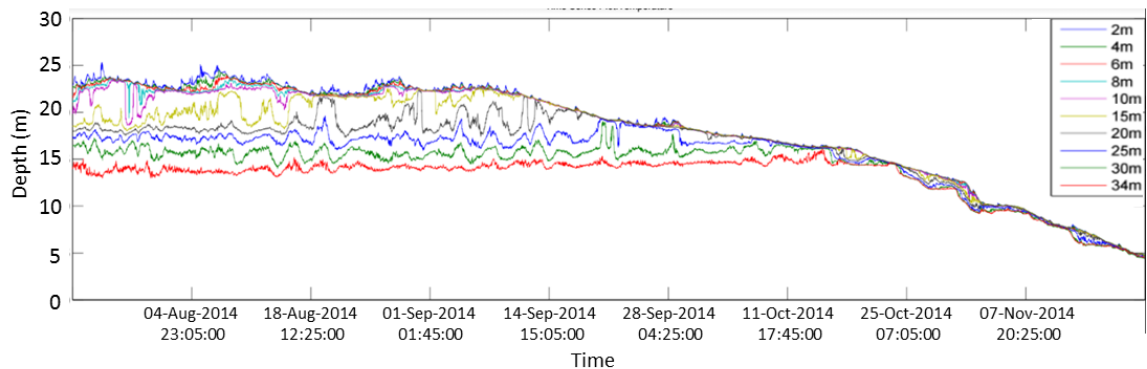


Figure B.1: Headpond temperature vs. depth time series (MAES project).

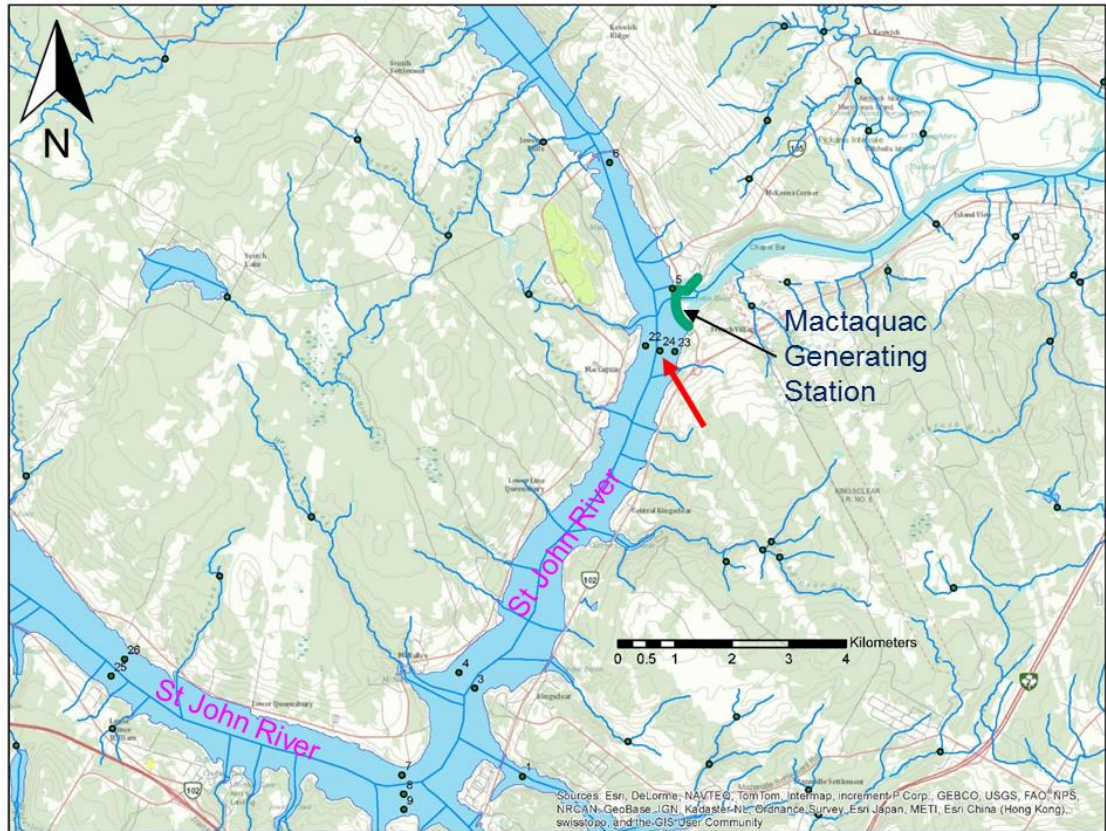


Figure B.2: MAES project map showing the location of thermograph strings in the headpond. The site 24 is indicated by a red arrow.

### Appendix C. Jib boom temperature data

Three independent headpond water temperature versus depth measurements were performed on December 5, 2016, June 1, 2017 and August 30, 2017 by deploying a Solinst Model 107 TLC (temperature-level-conductivity) meter from a jib boom on the SEP concrete structure. The photo in Figure C.1 shows the location and dimensions of the jib boom. It extends more than 3 meters above the water from the edge of the SEP. This ensured that the probe of the TLC meter did not touch submerged portions of the SEP structure and construction debris as it was lowered. Temperature data were logged manually at a 2 m interval in deep water and at a 1 meter interval closer to surface. The measured headpond temperatures are listed in Table C.1.

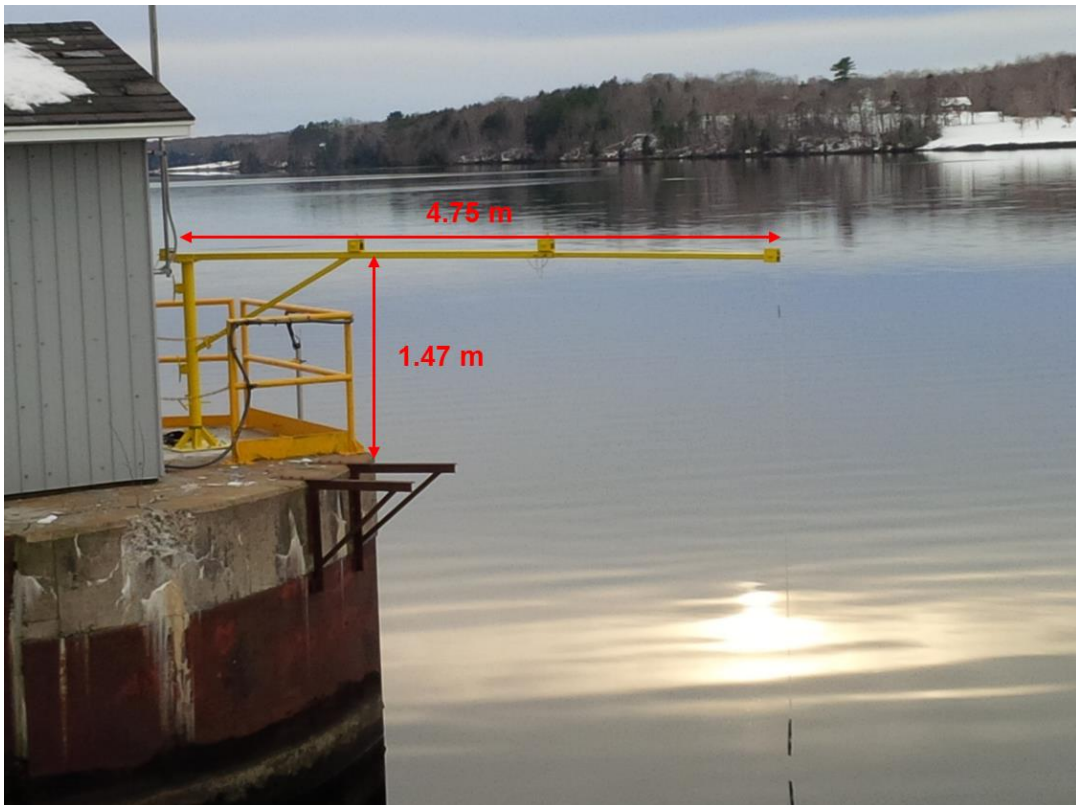


Figure C.1: Jib boom structure installed on the SEP concrete structure to facilitate measurements of water temperature versus depth.

Table C.1: Headpond water temperature data measured by TLC meter on the SEP concrete structure.

Date and Time								
2016-12-05 14:30			2017-06-01 11:30			2017-08-30 11:30		
Headpond level (feet)								
131.97			132			132		
Depth (m)	Elev. (feet)	Temp (°C)	Depth (m)	Elev. (feet)	Temp (°C)	Depth (m)	Elev. (feet)	Temp (°C)
37.21	9.92	-	37.32	9.92	10.70	37.32	9.92	11.10
37.11	10.25	4.55	37.24	10.18	10.75	37.02	11.16	11.10
36.81	11.23	4.50	36.94	11.16	10.80	35.02	17.71	11.60
34.81	17.79	4.50	34.94	17.71	10.80	33.02	24.25	11.90
32.81	24.35	4.50	32.94	24.25	10.80	31.02	30.79	12.10
30.81	30.91	4.50	30.94	30.79	10.90	29.02	37.33	12.70
28.81	37.47	4.50	28.94	37.33	10.90	27.02	43.87	13.50
26.81	44.03	4.50	26.94	43.87	10.90	25.02	50.42	13.60
24.81	50.59	4.50	24.94	50.42	10.90	23.02	56.96	14.50
22.81	57.15	4.50	22.94	56.96	11.20	21.02	63.50	14.90
20.81	63.71	4.50	20.94	63.50	12.20	19.02	70.04	16.00
18.81	70.27	4.50	18.94	70.04	12.40	17.02	76.59	18.60
16.81	76.83	4.50	16.94	76.59	12.50	15.02	83.13	21.20
14.81	83.39	4.50	14.94	83.13	12.60	13.02	89.67	21.50
12.81	89.95	4.50	12.94	89.67	12.60	11.02	96.21	21.60
10.81	96.51	4.50	10.94	96.21	12.70	9.02	102.76	21.60
8.81	103.07	4.50	8.94	102.76	12.70	7.02	109.30	21.70
6.81	109.63	4.50	6.94	109.30	12.80	6.02	112.57	21.70
5.81	112.91	4.50	5.94	112.57	12.80	5.02	115.84	21.70
4.81	116.19	4.50	4.94	115.84	12.90	4.02	119.11	21.70
3.81	119.47	4.50	3.94	119.11	13.00	3.02	122.38	21.80
2.81	122.75	4.50	2.94	122.38	13.00	2.02	125.65	21.80
1.81	126.03	4.60	1.94	125.65	13.20	1.02	128.93	21.80
0.81	129.31	4.50	0.94	128.93	13.50	0.52	130.56	21.90
0.31	130.95	4.50	0.44	130.56	13.50	0.12	131.87	21.90
0.00	131.97	4.50	0.00	132.00	-	0.00	132.26	-

## Appendix D. Frost depth estimation at the Mactaquac dam

The freezing and thawing cycles at dams may affect the heat transport within the dam. The main factor that controls the depth of frost penetration is the variation of air temperature during a freezing season, which can be presented by the freezing index (Soliman et al., 2008). The maximum frost depth can be calculated by a power function with a power of 0.5 as the equation below (Soliman et al., 2008):

$$Z = f \cdot \sqrt{F} \quad (\text{D.1})$$

$$F = \sum 0.5 \times (T_i^1 + T_i^2) \quad (\text{D.2})$$

where  $Z$  is the maximum frost depth [m] for a homogeneous ground.  $F$  is the freezing index given by the summation of the daily mean air temperature ( $^{\circ}\text{C}$ ) for a freezing season.  $T_i^1$  and  $T_i^2$  represent the maximum and minimum daily air temperature ( $^{\circ}\text{C}$ ) on day  $i$ , respectively.  $f$  is a constant coefficient.

The freezing index determined in this study, according to the air temperature recorded at the Mactaquac site during the freezing season from December 1, 2016 to April 1, 2017, is  $568.6^{\circ}\text{C}$ . The coefficient  $f$  varies at different locations, but is on the order of magnitude 0.01 for all soils (Vuola et al., 2007). Huen et al. (2006) used a coefficient value of 0.05537 to determine the frost depth for pavement materials in northern Ontario, Canada. The value used by Soliman et al. (2008) in Manitoba, Canada for pavement materials is equal to 0.048. A value of 0.01 was applied at Kyrkösjärvi earth dam in Finland to determine the maximum frost depth (Vuola et al., 2007). As the latitude of the Mactaquac site is higher than all of these three locations listed above, in

which case the air temperatures during winter are usually expected to be lower, thus the maximum frost depth at the Mactaquac site should not be larger than 1.3 m if using the largest coefficient of 0.05537 (Huen et al., 2006) for equation D.1.

## Appendix E. Construction of the Mactaquac embankment dam

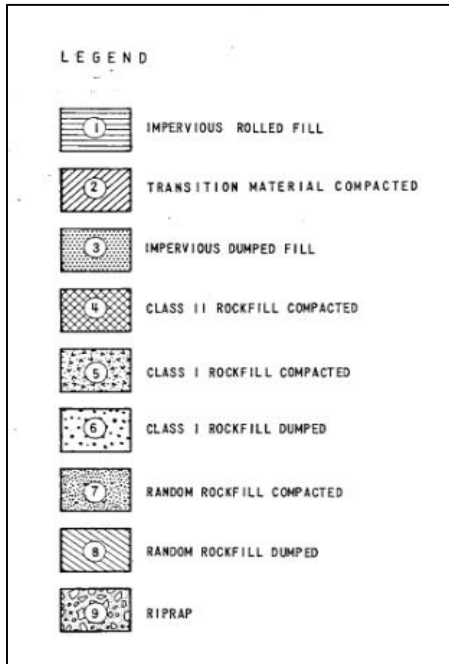
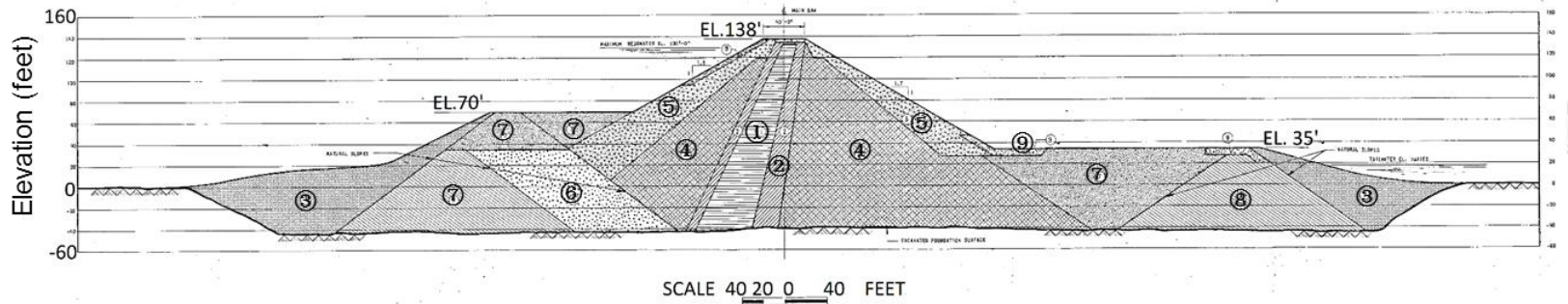


Figure E.1: Design drawing for a cross section through the middle of the Mactaquac embankment dam, approximately 300 m away from the dam/concrete interface, showing zonation of the construction materials, and upstream inclination of the core. Scale bar at base of drawing spans 80' and divisions on vertical scale are 20' apart. Upstream and downstream slopes of the main dam are 1.8:1 and 1.7:1, respectively. (Drawing provided by NB Power, based on an original drawing by H.G. Acres in 1968, Drawing No. 1140-C-2936)



Figure E.2: Photo of the clay till core materials distribution looking from the SEP to the south at the time of dam construction in 1967 indicating that the core was made wider at its southern abutment (NB Power).

## Appendix F. Simulated temperatures within the dam/concrete structure

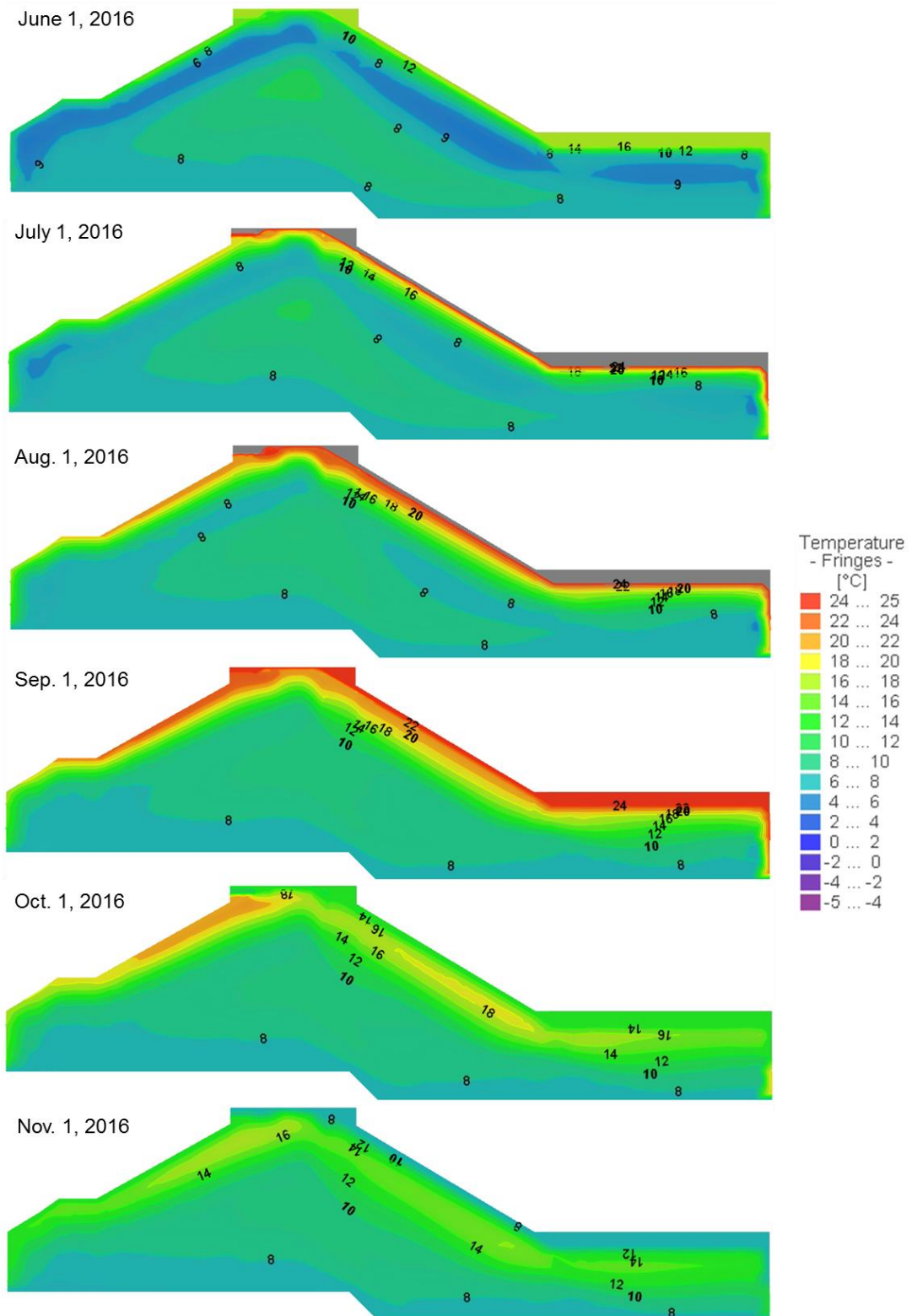


Figure F.1: Simulated temperature distribution along the dam/concrete interface (slice 6 in Figure 4-3) for bulk seepage scenario B9 from June 1, 2016 to Nov. 1, 2016.

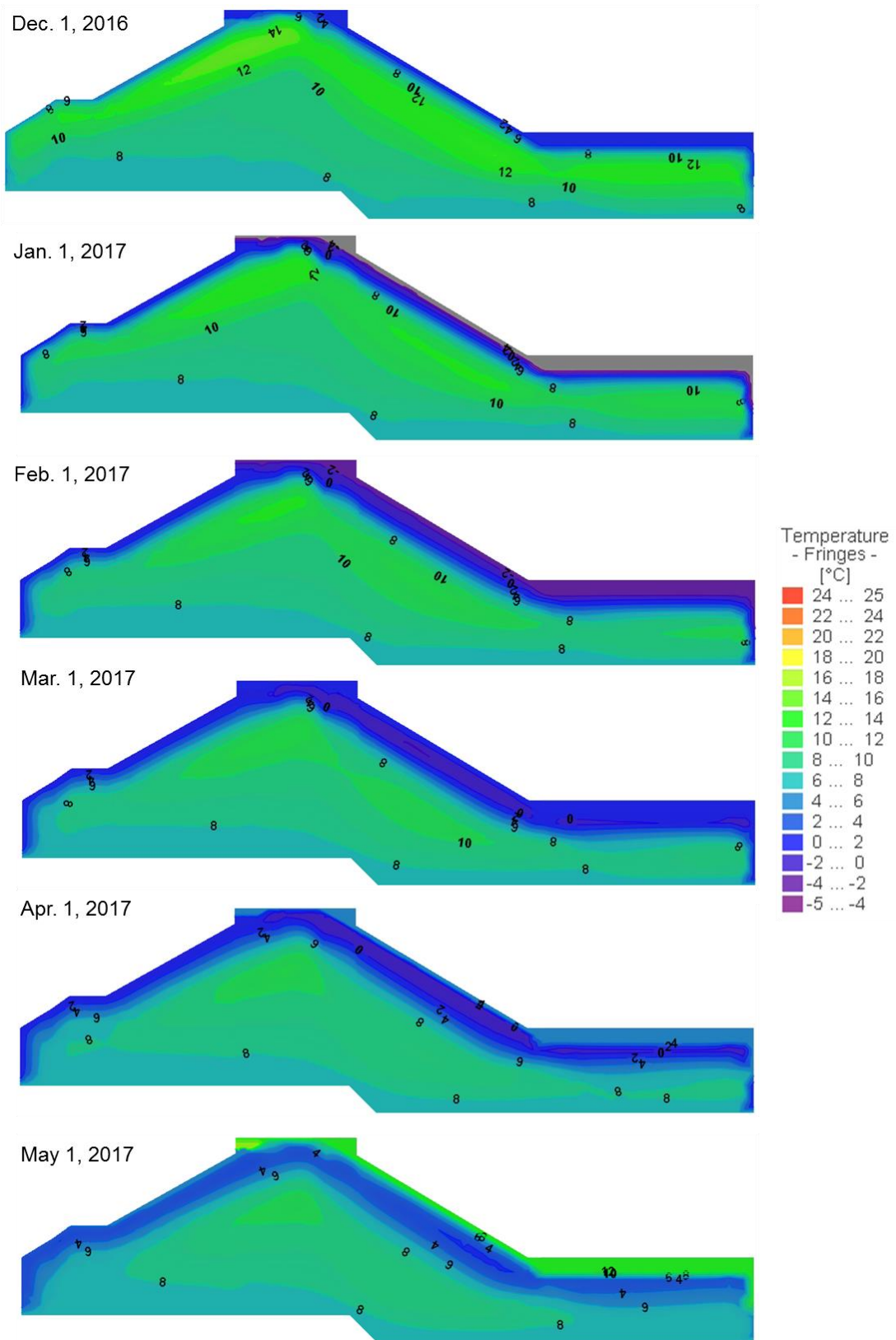


Figure F.2: Simulated temperature distribution along the dam/concrete interface (slice 6 in Figure 4-3) for bulk seepage scenario B9 from Dec. 1, 2016 to May 1, 2017.

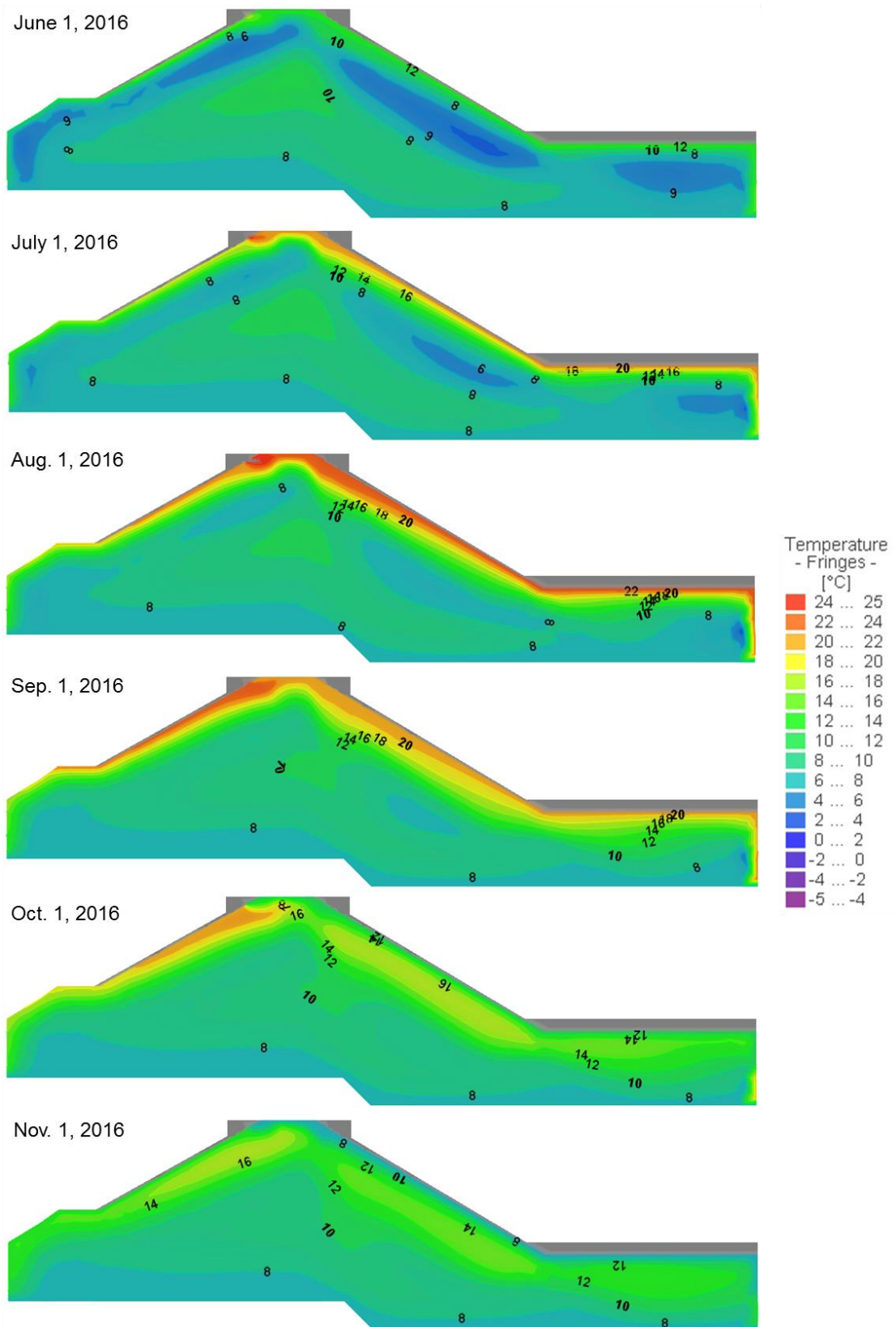


Figure F.3: Simulated temperatures on slice 1 within the embankment, 30.6 m from top of the SEP interface, for bulk seepage scenario B9; June 1, 2016 to Nov. 1, 2016.

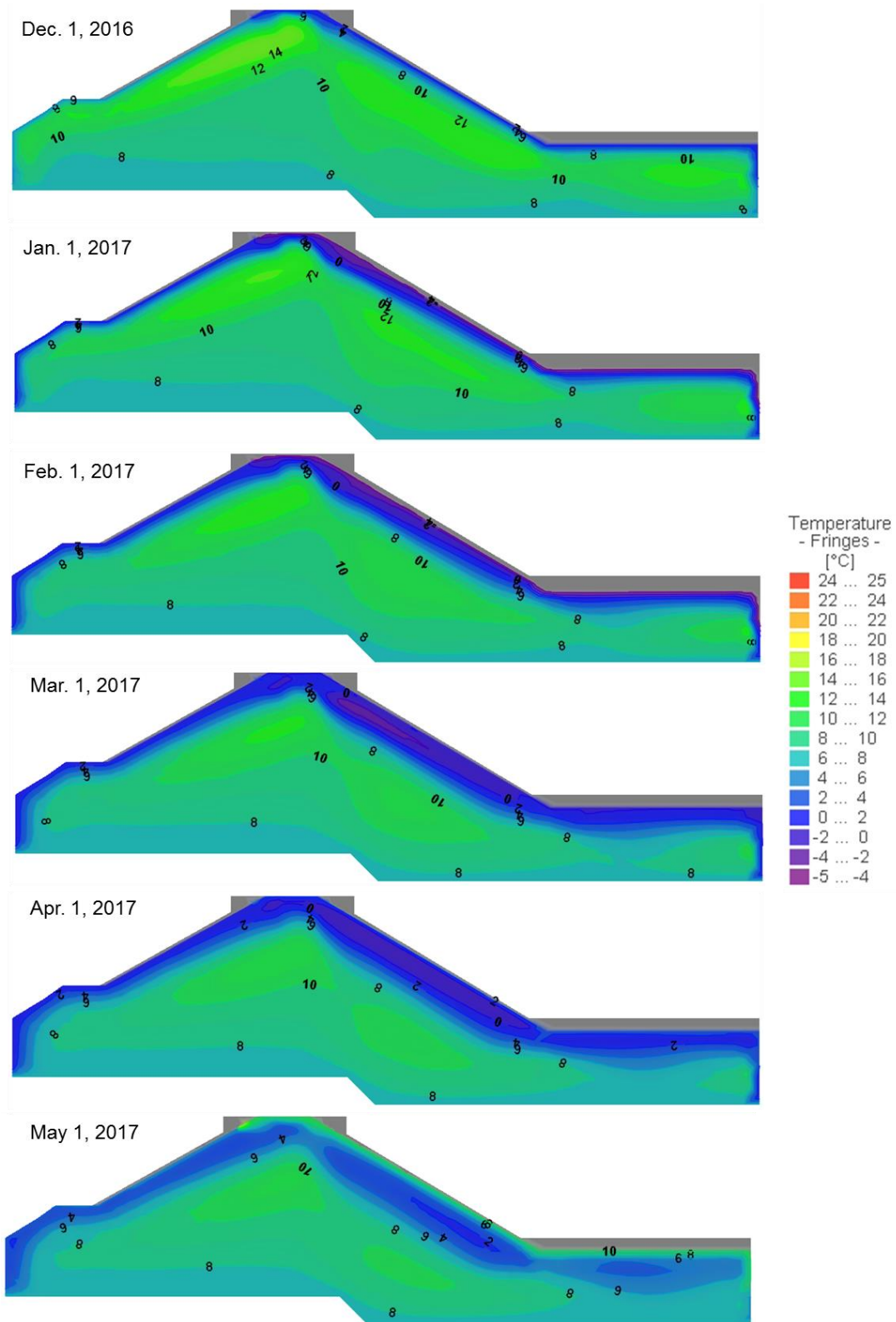


Figure F.4: Simulated temperatures on slice 1 within the embankment, 30.6 m from top of the SEP interface, for bulk seepage scenario B9; Dec 1, 2016 to May 1, 2017.

**Appendix G. Interpreted position of the clay till core-concrete interface through a borehole seismic reflection survey**

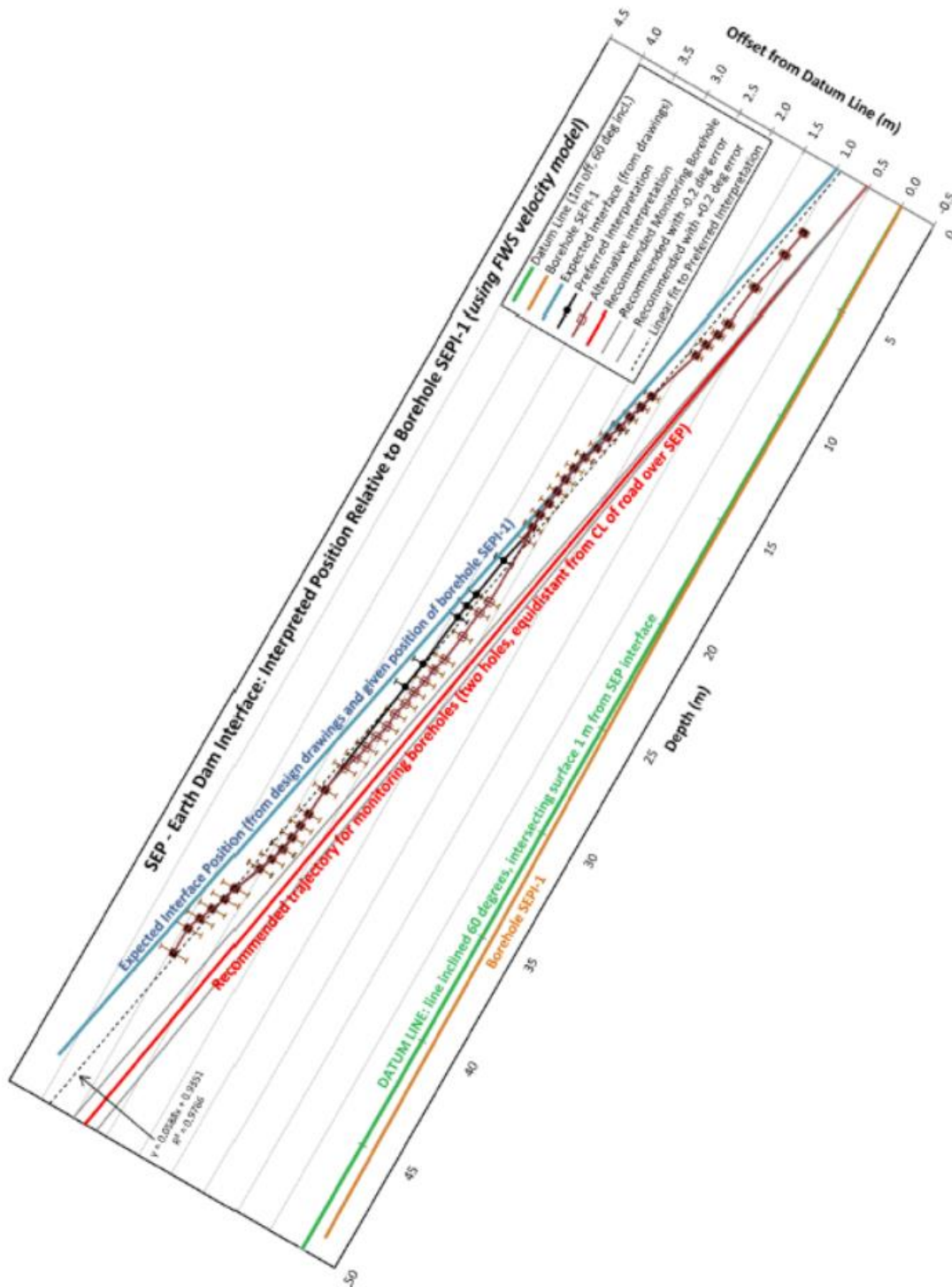


Figure G.1: Interpreted clay till core-concrete interface. Preferred interpretation shown in black. Red line shows recommended trajectory for seepage monitoring boreholes (Butler et al., 2018)

**Appendix H. An example of simulated temperature profile with seepage simulated for an entire year.**

Figure H.1 shows an example of simulated temperature profile with shallower seepage simulated in both the concrete and the embankment for a whole year. Three seepage zones extending from upstream to downstream were simulated in this numerical simulation. A seepage zone with hydraulic conductivity of  $4.6 \times 10^{-4}$  m/s was simulated in the concrete between the elevation of 115.5' and 116'. The thickness of the seepage zone is about 1 m. A seepage zone with hydraulic conductivity of  $5.0 \times 10^{-5}$  was simulated in the embankment between elevation 115.5' and 127' and the thickness of it is 0.2 m. The last seepage zone was simulated in the embankment between elevation 95' to 96' with hydraulic conductivity of  $4.6 \times 10^{-4}$  m/s and thickness of 0.3 m.

It can be found that with seepage zones simulated for a whole year, the temperature anomaly at the shallower depth appear during both summer and winter.

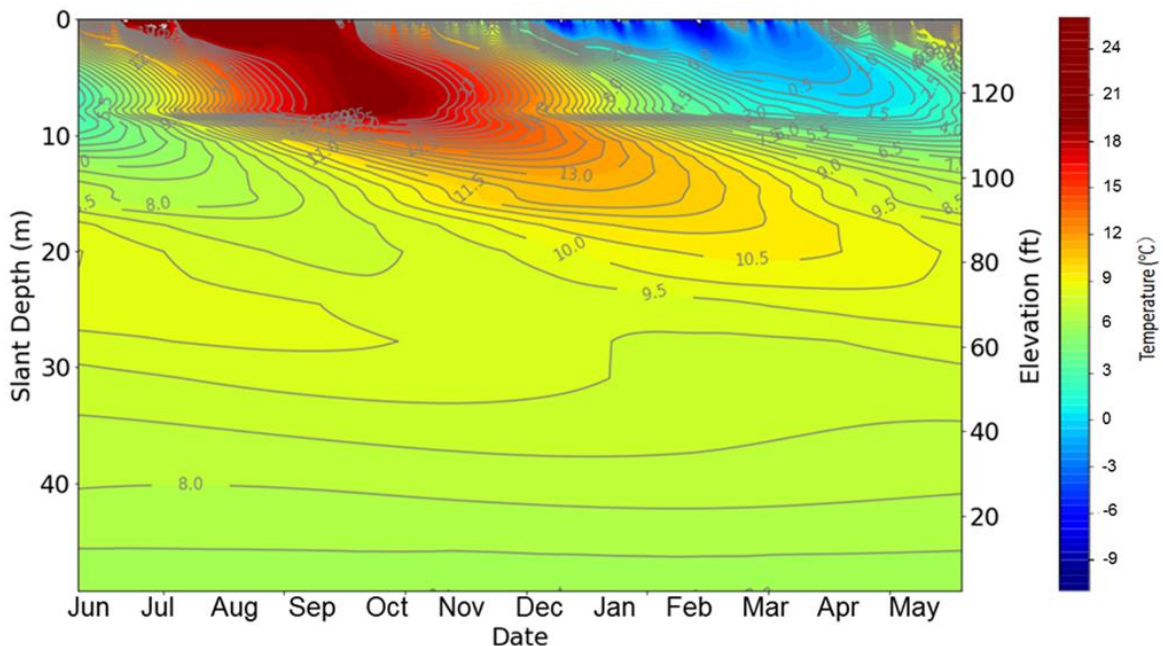
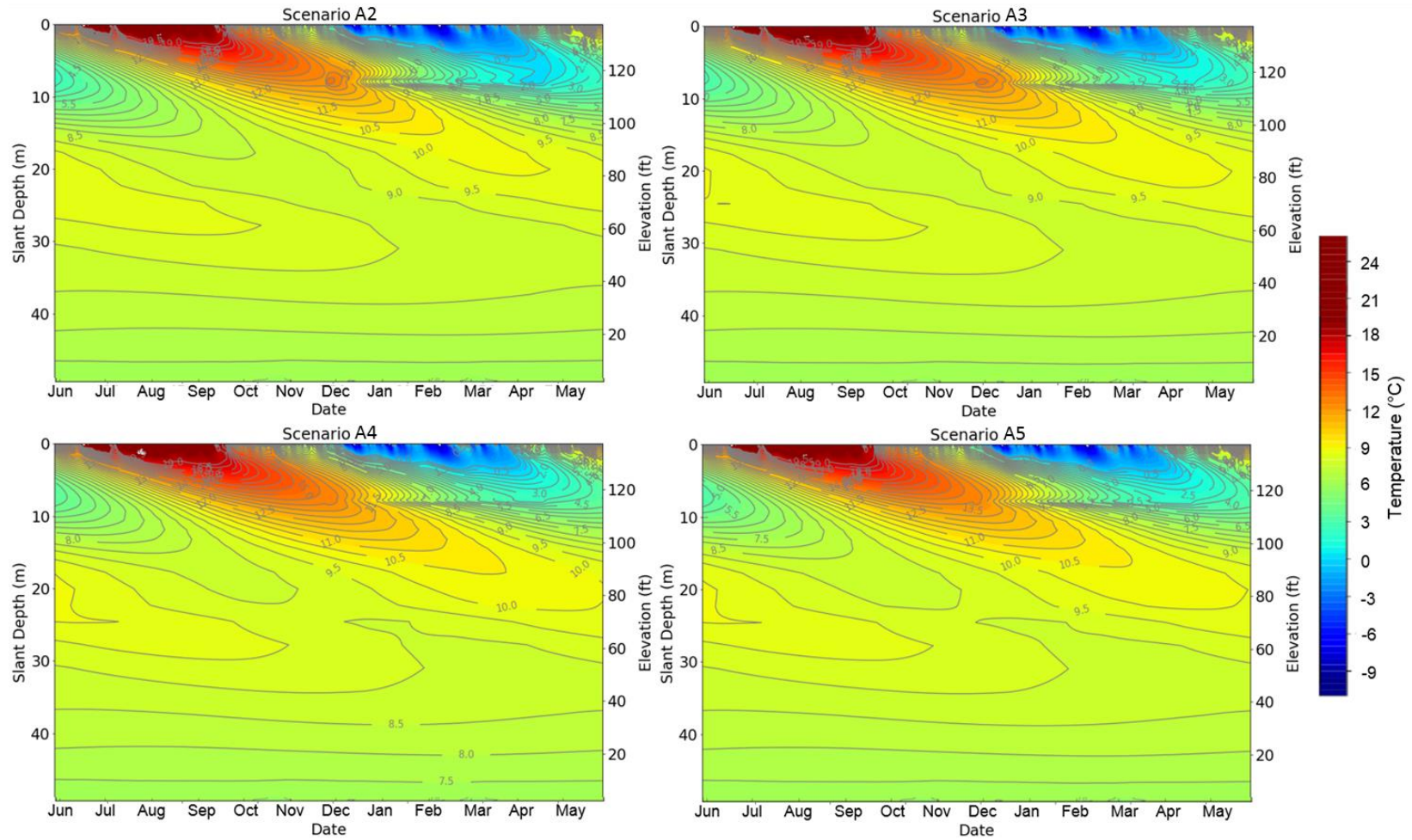


Figure H.1: An example of the simulated temperature versus depth plot from June 1, 2016 to June 1, 2017 for the case of a seepage zone simulated in the concrete and along the interface for an entire year.

**Appendix I. Simulated temperature variations versus time for scenarios A2 to A5**



160

Figure I.1: Simulated temperature variations versus time for scenarios A2 to A5.

## Appendix J. Weekly average temperature profiles for scenarios B11 and B12

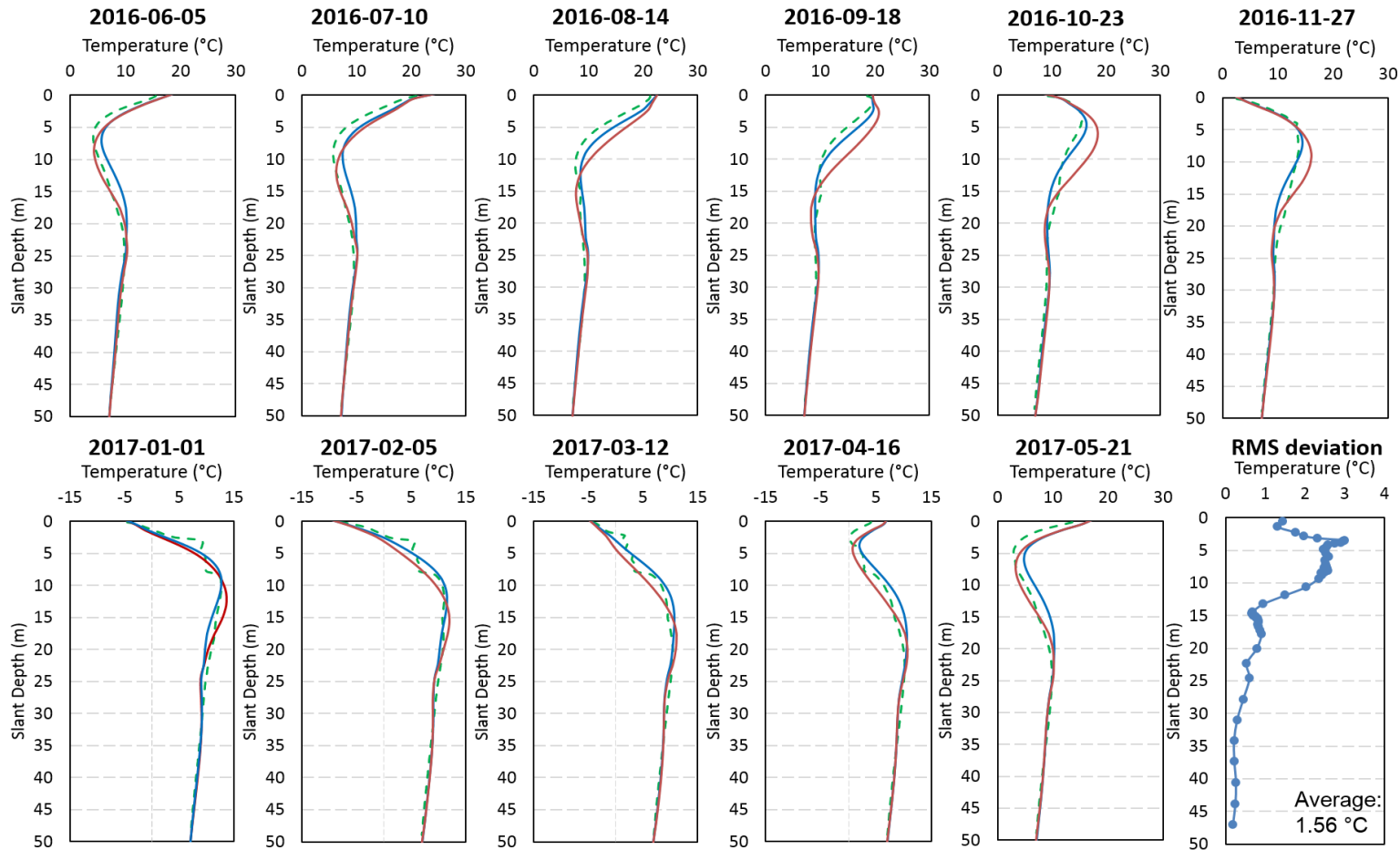


Figure J.1: Comparisons of weekly average DTS temperature profiles (in dashed green) to the simulated bulk seepage temperature profiles for scenarios B9 (in blue) and B11 (in red) at intervals of 35 days, along with annual average RMS deviation as a function of depth for scenario B11.

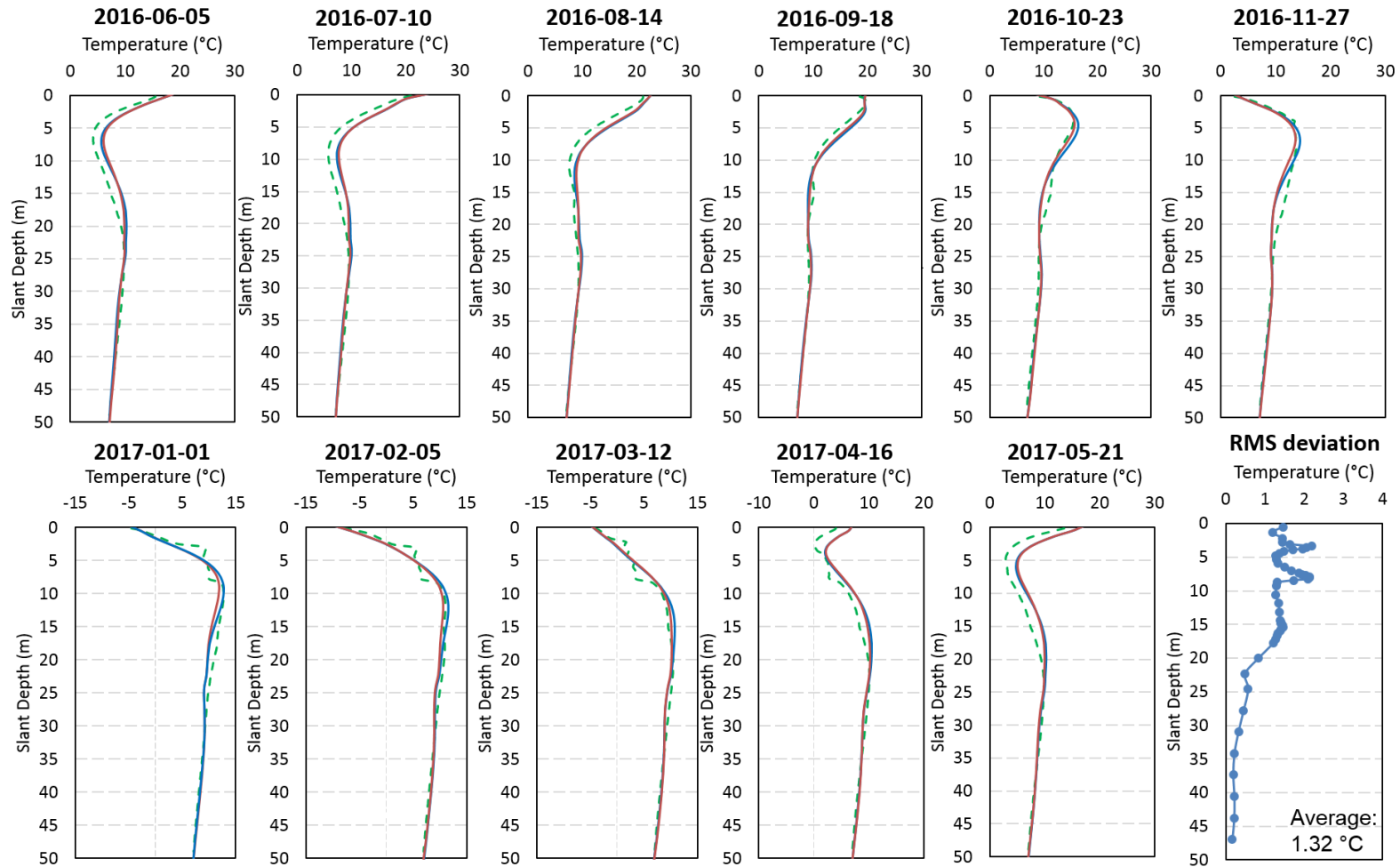


Figure J.2: Comparisons of weekly average DTS temperature profiles (in dashed green) to the simulated bulk seepage temperature profiles for scenarios B9 (in blue) and B12 (in red) at intervals of 35 days, along with annual average RMS deviation as a function of depth for scenario B1.

**Appendix K. Photographs of concrete drill core from boreholes SEPI-1, 2 and 3**

163

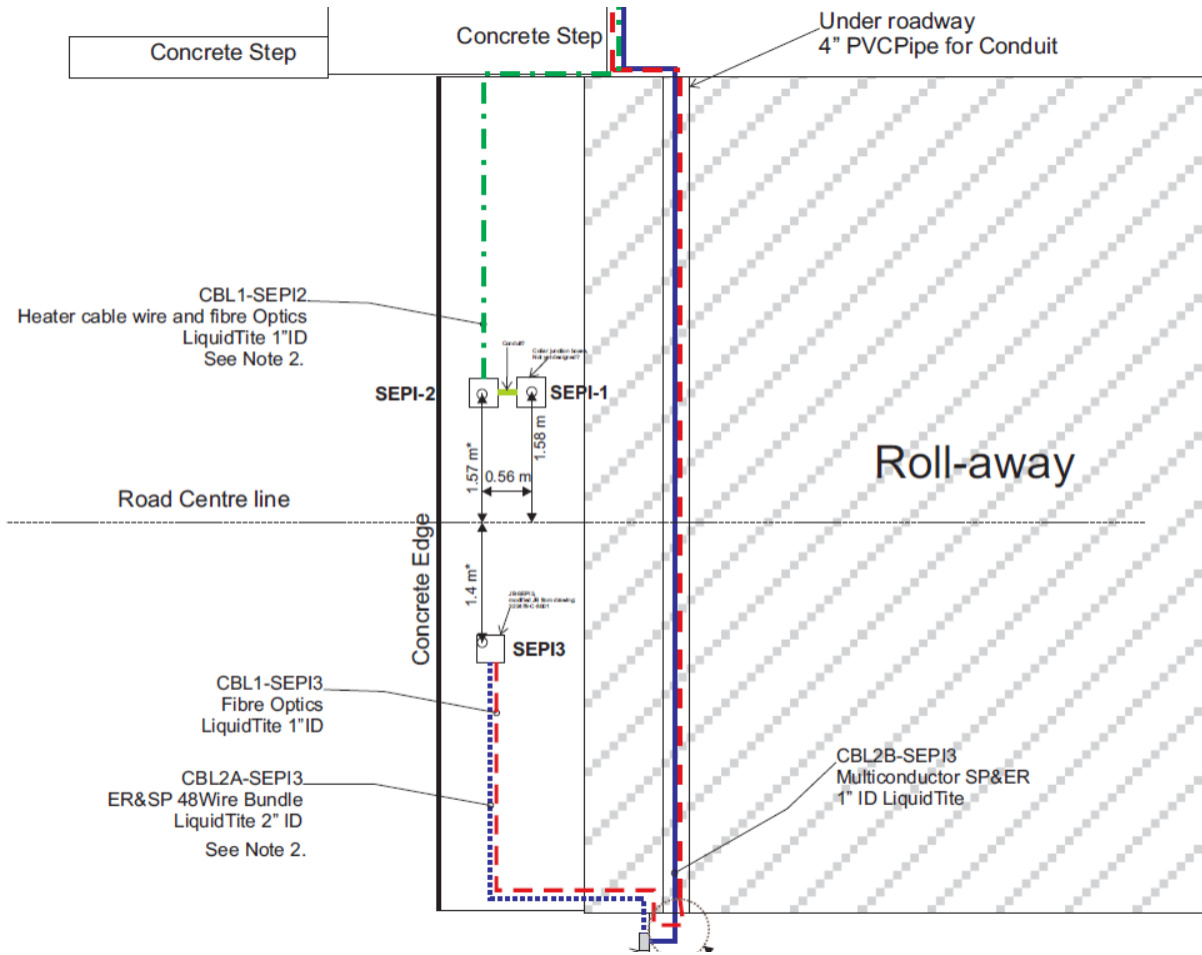


Figure K.1: Plan view of the top of the SEP showing locations of the collars of boreholes SEPI 1, 2 and 3 below the road. (Drawing by A. Ringeri).



Figure K.2: Photo of the concrete core drilled from borehole SEPI 1 between slant depth 0' to 27' (slant depth 0 to 8.2 m).

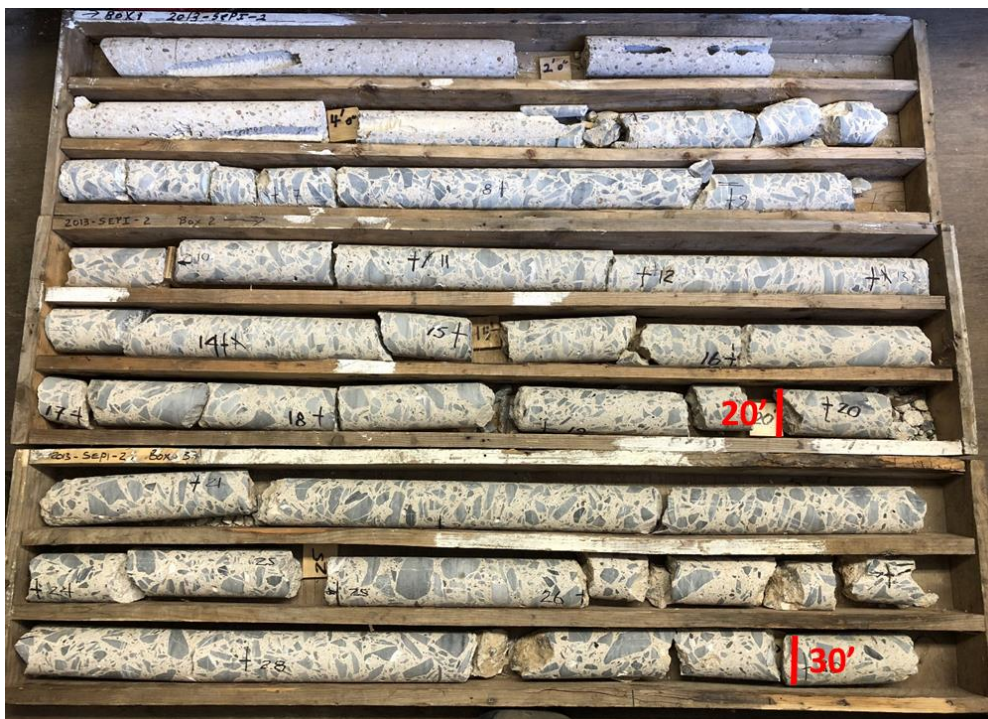


Figure K.3: Photo of the concrete core drilled from borehole SEPI 2 between slant depth 0' to 30' (slant depth 0 to 9.1 m).

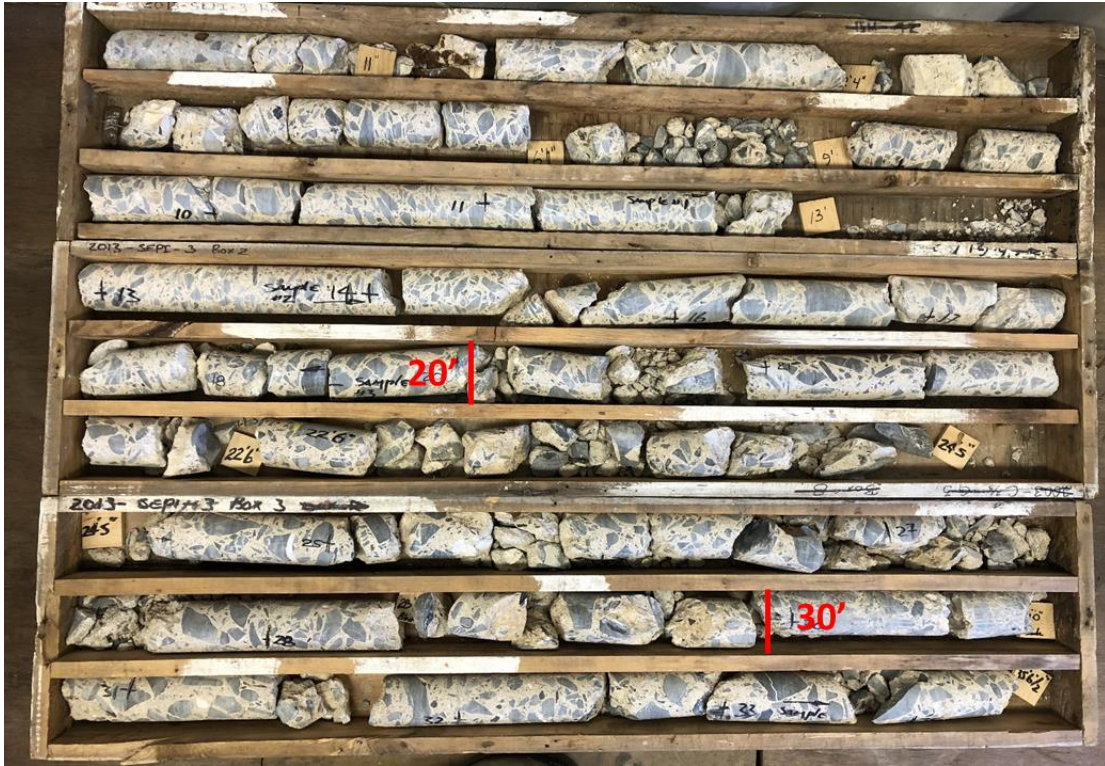


Figure K.4: Photo of the concrete core drilled from borehole SEPI 3 between slant depth 0' to 35' (slant depth 0 to 10.7 m).



Figure K.5: Photo of the concrete core drilled from borehole SEPI 2 showing the steeply (red arrow) and gently (blue arrows) dipping fractures at a slant depth of approximately 50' (15.24 m). The dashed yellow lines are approximately parallel to the core axis.



Figure K.6: Photo of the concrete core drilled from borehole SEPI 3 showing the steeply dipping fracture at slant depth a) 27' (8.2 m); b) 29' (8.8 m); and c) 67' (20.4 m). The shallow angles of the steeply dipping fractures relative to the core axis and the observed water staining are indicated by red and green arrows, respectively. The dashed yellow lines are approximately parallel to the core axis.

## CURRICULUM VITAE

- Candidate's full name: Tana Yun
- Universities attended: University of Waterloo,  
Bachelor of Science in Geophysics, 2015  
China University of Geosciences,  
Bachelor of Science in resource exploration, 2012
- Conference Presentations: Yun T., Butler, K.E., MacQuarrie K.T., Mclean, B., & Campbell, I. (2018). *Seasonal temperature monitoring and modelling for Seepage Reconnaissance in an Embankment Dam*. Extended abstract accepted for poster presentation at EAGE Near Surface Geoscience Conference and Exhibition, Sep. 9-13, 2018, Porto, Portugal.
- Yun, T., Ringeri, A., Butler K. E., & MacQuarrie, K. T. B. (2016). *Seepage reconnaissance in an embankment dam using distributed temperature sensing (DTS): monitoring and modelling of seasonal effects*. Poster presented at the American Geophysics Union Fall Meeting, San Francisco, US.
- Yun, T., Ringeri, A., Butler K. E., & MacQuarrie, K. T. B. (2016). *Seasonal temperature monitoring for seepage reconnaissance in an embankment dam*. Poster presented at the Annual Scientific Meeting of the Canadian Geophysical Union, Fredericton, NB, Canada.